Advances in Civil Engineering and Transportation IV

Edited by
Xiangdong Zhang and Bin Zhang

TRANS TECH PUBLICATIONS

Advances in Civil Engineering and Transportation IV

Edited by
Xiangdong Zhang
Bin Zhang

Advances in Civil Engineering and Transportation IV

Selected, peer reviewed papers from the
4th International Conference on Civil Engineering and Transportation (ICCET 2014),
December 24-25, 2014, Xiamen, China

Edited by

Xiangdong Zhang and Bin Zhang

Trans Tech Publications Ltd
Churerstrasse 20
CH-8808 Pfaffikon
Switzerland
http://www.ttp.net

Volumes 744-746 of
Applied Mechanics and Materials
ISSN print 1660-9336
ISSN cd 1660-9336
ISSN web 1662-7482

Full text available online at *http://www.scientific.net*

***Distributed** worldwide by*

Trans Tech Publications Ltd
Churerstrasse 20
CH-8808 Pfaffikon
Switzerland

Fax: +41 (44) 922 10 33
e-mail: sales@ttp.net

and in the Americas by

Trans Tech Publications Inc.
PO Box 699, May Street
Enfield, NH 03748
USA

Phone: +1 (603) 632-7377
Fax: +1 (603) 632-5611
e-mail: sales-usa@ttp.net

Preface

The 4th International Conference on Civil Engineering and Transportation took place in Kunming, China, December 24-25, 2014. The impact of construction technology and transport infrastructure development is known to be significant on the economy of any country. Therefore, the International Conference on Civil Engineering and Transportation is aspired to promote construction practices and create awareness among different industry professionals. And the main aim of this conference is to bring together academics and other professionals from all over the world, for the presentation and exchange of their thoughts and experiences on concepts, trends and practices in civil engineering and advanced transportation fields. The conference is intended to offer a stimulating environment to encourage discussion and exchange of ideas leading to the advanced construction technology and transportation.

All the papers in the conference proceedings have been undergone the intensive review process performed by the international technical committee, and only accepted papers are included. This volume comprised the selected papers from the subject areas of Structural Engineering; Geotechnical Engineering and Geological Engineering; Bridge Engineering; Earthquake Engineering; Tunnel, Subway and Underground Facilities; Hydraulic Engineering, Water Supply and Drainage Engineering; Coastal Engineering; Surveying Engineering, Cartography and Geographic Information Systems; Ecological Architecture and Energy Consumption, Energy Saving, Heating, Gas Supply, Ventilation and Air Conditioning Works; Disaster Prevention and Mitigation Engineering; Computational Mechanics and Mathematical Modeling; Construction Project Planning and Monitoring; Roads, Railway Engineering and Landscape Design; Transportation Planning, Construction and Operation Organization; Modern Logistics Systems and Supply Chain; Automotive Engineering and Other Vehicle Tools; Intelligent Transportation Theory and Application; Transportation Control and Information Technology; Transportation and Economic Development, and Low Carbon Transportation; Public Transport Planning and Management; Architectural Design and Theory; Building Technology and Science; Urban Planning and Design, Landscape Design; Environmental Engineering and Environmental Protection; Sustainable City and Regional Development; Building Materials, Processing Technology and Applications.

We would like to acknowledge and give special appreciation to our keynote speakers for their valuable contribution, our delegates for being with us and sharing their experiences, and our invitees for participating in this conference. We would also like to extend my appreciation to the steering Committee and the International Scientific Committee for the devotion of their precious time, advice and hard work to prepare for this Conference.

The editors

Conference Organization

Chairman

Prof. Yishan Pan, Liaoning Technical University, China

International Scientific Committee

Prof. J. H. Bungey, University of Liverpool, Liverpool, UK

Prof. K. J. Bathe, Massachusetts Institute of Technology, USA

Prof. Lawrence C. Bank, University of Wisconsin-Madison, USA

Prof. Longsheng Bao, Shenyang Jianzhu University, China

Prof. Xiangdong Zhang, Liaoning Technical University, China

Prof. Chaohe Chen, South China University of Technology, China

Prof. Xianglin Gu, Tongji University, China

Prof. Xiating Feng, Institute of Rock and Soil Mechanics, CAS

Prof. Hongnan Li, Dalian University of Technology, China

Prof. Zhihua Chen, Tianjin University, China

Prof. Jian-Fei Chen, the University of Edinburgh, UK

Prof. Shucai Li, Shandong University, China

Prof. Lai Wang, Shandong University of Science and Technology

Prof. Xin'gang Zhou, Yantai University, China

Prof. Xuejun Zhou, Shandong Jianzhu University, China

Prof. Feng Fan, Harbin Institute of Technology, China

Prof. Luciano Feo, University of Salerno, Italy

Prof. Han-Bin Ge, Meiju University, Japan

Prof. Haiyan Guo, Ocean University of China

Prof.Zong Woo Geem, iGlobal University, USA

Prof. Linhai Han, Tsinghua University, China

Prof. Yong Huang, Guizhou University, China

Prof. Jiping Hao,Xi'an University of Architecture and Technology,China

Prof. Tamon UEDA, Hokkaido University, Japan

Prof. Guangyue Wang, Shandong University,China

Prof. Lai Wang, Shandong University of Science and Technology, China

Prof. Yan Wang, Qingdao Technological University, China

Prof. Jinfeng Wang, Huaqiao University, China

Prof. Zhi-Shen Wu, Ibaraki University, Japan

Prof. Shi Yan, Shenyang Jianzhu University, China

Dr. Scott T. SMITH, Hong Kong University, Hong Kong

Prof. J-G. Teng, Hong Kong Polytechnic University, Hong Kong

Prof. Xin Zhang, Shandong Jianzhu University, China

Prof. Yigang Zhang, Beijing University of Technology, China

Prof. Xin'gang Zhou, Yantai University, China

Prof. Xuejun Zhou, Shandong Jianzhu University

Prof. Yanpeng Zhu, Lanzhou University of Technology, China

Prof. Chaoying Zou, Harbin Institute of Technology, China

Prof. Jiru Zhang, Wuhan University of Technology, China

Prof. Chuangbin Zhou, Wuhan University, China

Local Organizing Committee

Prof. Xiangdong Zhang, Liaoning Technical University, China

Prof. Bin Zhang, Liaoning Technical University, China

Table of Contents

Chapter 2: Geotechnical Engineering and Geological Engineering

Chapter 3: Bridge Engineering

Chapter 4: Earthquake Engineering

Chapter 5: Tunnel, Subway and Underground Facilities

Chapter 6: Hydraulic and Hydrodynamics Engineering, Water Supply and Drainage Engineering

Chapter 7: Coastal Engineering

Chapter 8: Roads and Railway Engineering

Chapter 9: Building Materials and Technology

Chapter 10: Building Technology and Science

Chapter 11: Computational Mechanics and Mathematical Modeling

Chapter 12: Surveying Engineering, Cartography and Geographic Information Systems

Chapter 13: Disaster Prevention and Mitigation Engineering

Chapter 14: Transportation and Traffic Planning, Operation Organization and Management

Chapter 15: Modern Logistics Systems and Supply Chain

Chapter 16: Intelligent Transportation Theory and Application

Chapter 17: Transportation Control, Analysis, Monitoring, Applied Information Technology

Chapter 18: Public Transport Planning and Management

Chapter 19: Transportation and Economic Development, and Low Carbon Transportation

Chapter 20: Architectural Design and Theory

Chapter 21: Urban Planning and Design, Landscape Design, Sustainable City and Regional Development

Chapter 22: Ecological Architecture and Energy Consumption, Energy Saving, Heating, Ventilation and Air Conditioning Works

Chapter 23: Environmental Engineering, Ecological and Environmental Protection

CHAPTER 1:

Structural Engineering

Applied Mechanics and Materials Vols. 744-746 (2015) pp 3-7

doi:10.4028/www.scientific.net/AMM.744-746.3

Analyzing Fracture Behavior of Beam-Column Joints Using Micromechanical Fracture Models

Chen Zhang[1, a], Yuping Sun[1], Jutao Zhang[2] and Yu Gu[1]

[1] School of Civil Engineering, Lanzhou University of Technology, China

[2]Gansu Institute of Architectural Design and Research, China

[a]chenzi10@163.com

Keywords: fracture, beam-column joints, VGM

Abstract. The micromechanical fracture models were used to study the fracture behavior of the welded connection and welded-bolted connection joints. The Void Growth Model was implemented in commercial finite element software ABAQUS through the user-defined subroutines. The results predicted that cracks initiated at the edge of the welds and extended along the length and thickness of the welds. Comparing the effects of equivalent plastic strain and stress triaxiality for the fracture of the first failure element of both beam-to-column joints, we found that the equivalent plastic strain grew linearly as the loads increased and the weld of the lower flange generated cracks when the stress triaxiality increased at maximum value.

Introduction

Ductile crack initiation is caused by void nucleation, growth and coalescence. Rice and Tracey[1] suggest that void growth is dependent on the evolution of two key quantities—the equivalent plastic strain, and the stress triaxiality. And they found that for any remote strain rate field, the void enlargement rate is amplified over the remote strain rate by a factor rising exponentially with the ratio of mean normal stress to yield stress. Gurson[2] proposed a closed yield surface criterion by the single hole geometry model, and explained the impact of porosity and stress state on plastic yielding and expansion. Then, he established the Gurson Model. Changqing Zheng[3] used low-alloy steel BS4360-50D to study, he found the evolution law of void nucleation, growth and coalescence, and gave a conception of the ratio of void increment. And then he created the VGC criterion about ductile failure by combing microscopic and macroscopic behavior of materials. Kanvinde and Deierlein[4] have been verified to accurately predict ductile fracture in steel connection details under monotonic loading through a series of twelve pull-plate experiments and complementary finite-element analyses of bolted connections and Reduced Beam Section type details. Yuanqing Wang[5] found that the void growth model and the stress modified critical strain model have been validated to predict ductile fracture initiation in steel through a series of tests and analyses of welded beam-to-column joints. However, he found that the results of J-integral are more conservative.

The fracture models based on micromechanics could capture the triaxial stresses and plastic strains which is directly related to ductile fracture initiation. The void growth model was used in this paper by developing UVARM and VUMAT subroutines in ABAQUS software. The crack initiation and crack propagation of welded beam-to-column joints were predicted.

Micromechanics-Based Fracture Models

The void growth model(VGM) is used to predict fracture initiation under monotonic loading, and the fracture is predicted to occur when an integral of stress and strain history is equal to a critical value. This corresponds to the voids growing large enough to exceed a critical void size to trigger necking instabilities between voids leading to coalescence and microcrack formation. The failure criterion of VGM is expressed as:

$$\int_0^{\varepsilon_p^{critical}} \exp\left(1.5\sigma_m/\sigma_c\right)d\varepsilon_p - \eta > 0 \quad (1)$$

where σ_m is mean stress, σ_c is effective stress, σ_m/σ_c is tress triaxiality, ε_p is equivalent plastic strain, $d\varepsilon_p$ is incremental equivalent plastic strain, and η is the material capacity determined by critical void growth ratio.

The base metal used 345MPa grade Chinese structural steel and the weld metal used 500MPa grade Chinese structural steel. Grade 10.9 frictional type high strength bolts were used in the welded-bolted connection joint with flanges and web spliced. According to the method of parameters calibration in research[7], the research[6] calibrated the material parameters by SNT tests. The results are shown in Table1.

Table1. Parameters of VGM

Material	VGM
	η
Base metal	2.55
Weld metal	2.63

The Finite Element Models of Welded Beam-Column Joints

In this paper, the models of welded beam-to-column joints were taken from middle column of Gansu Science and Technology Museum, in which the beams and columns sectional dimensions were welded H800mm × 250mm × 16mm × 32mm and 600mm × 600mm × 28mm × 28mm. Taking advantage of symmetry, half models (shown in Fig.1) were employed in the FEM simulations. The models were hingged at column end and loaded by displacement control at beam end. Elements by the 8-node hexahedron element were divided. The stress and strain properties of base metal and weld metal were explicitly modeled in FEM with isotropic incremental von Mises plasticity and large deformation theory.

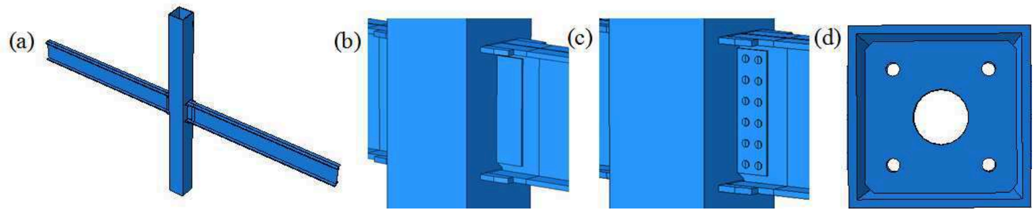

Fig.1. FEM of beam-to-column joint: (a)Whole model of beam-to-column joint, (b)Local region of joint of welded connection joint, (c) Local region of joint of welded-bolted connection joint, (d)Inner diaphragm of joint region.

FEM Simulations of Fracture of Beam-Column Joints

Fracture Prediction of Welded Connection Joints. In order to predict the ductile fracture initiation of the beam-to-column joints, the VGM criteria was used in finite-element simulation in this paper. When material points satisfy the fracture criterion, the cracks will generate in the joints with displacement increasing. Using UVARM subroutine to predict the crack initiation, we found that the cracks of welded connection joint are inclined to appear in the edges of welds. In addition, the crack of welded-bolted connection joint first appeared in the edges of weld, then the cracks generated in the bottom of welds(as seen in Fig. 2). The VUMAT subroutine was developed to predict the path of the crack propagation, the elements were deleted from the finite model one by one which satisfied the fracture criteria. The results showed that the cracks grew along the length and thickness of the welds. Take the welded-bolted connection joint, for example(as seen in Fig. 3).

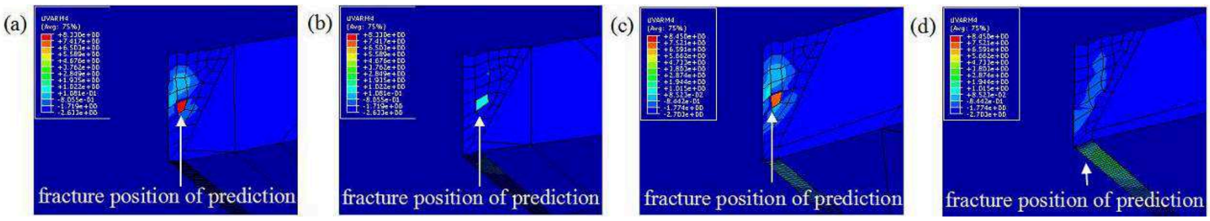

Fig.2. Prediction of fracture position of welded connection joint: (a)Top flange weld of welded connection joint, (b)Lower flange weld of welded connection joint, (c)Top flange weld of welded-bolted connection joint, (d)Lower flange weld of welded-bolted connection joint.

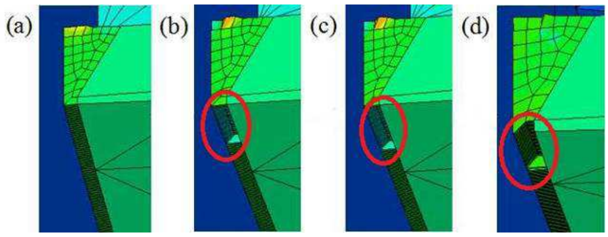

Fig.3. The crack development of lower flange: (a) Displacement=2.69mm, (b) Displacement=4.66mm, (c) Displacement=7.67mm, (d) Displacement=20.32mm.

Equivalent Plastic Strain Analysis of First Failure Element. In Fig.4, the changes of the equivalent plastic strain of bottom weld on the loading history were represented. When the displacement increased to 0.5mm, the status of welds of both joints went from elasticity into plasticity. The equivalent plastic strain grew linearly with increasing displacement. The cracks initiated when the equivalent plastic strain of welded and welded-bolted connection joints increased to 0.23mm and 0.09mm. At this time, the element has failed, so the equivalent plastic strain dropped to zero.

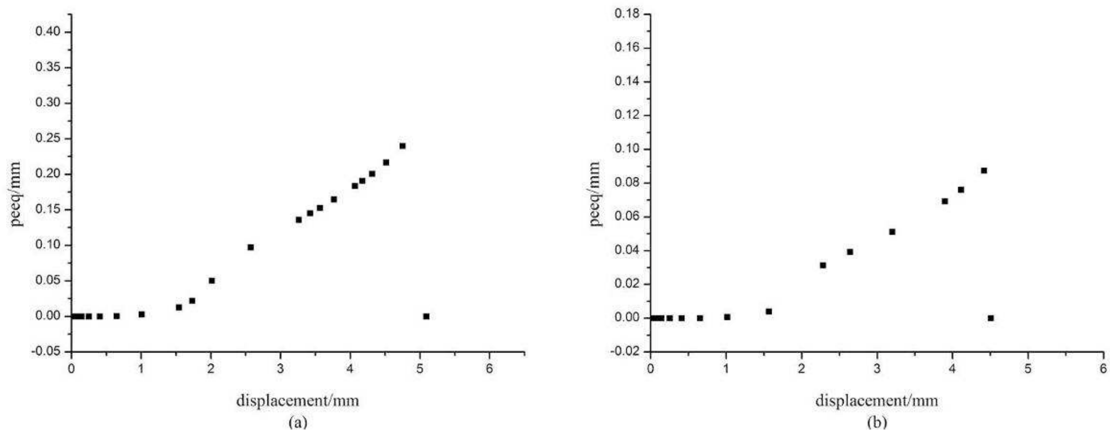

Fig.4. The relationship between equivalent plastic strain and displacement: (a)Welded connection joint, (b)Welded-bolted connection joint.

Stress Triaxiality Analysis. As shown in Fig. 5, the weld of welded connection joint generated cracks when the stress triaxiality rose up to 1.7 but not the maximum. This is because the equivalent plastic strain has not increased to critical value when the stress triaxiality reached the maximum. The stress triaxiality of first failure element of welded-bolted connection joint increased with displacement. When the stress triaxiality got to peak 2.4, the element invalidated, that was crack formed. Then the stress triaxiality dropped to zero.

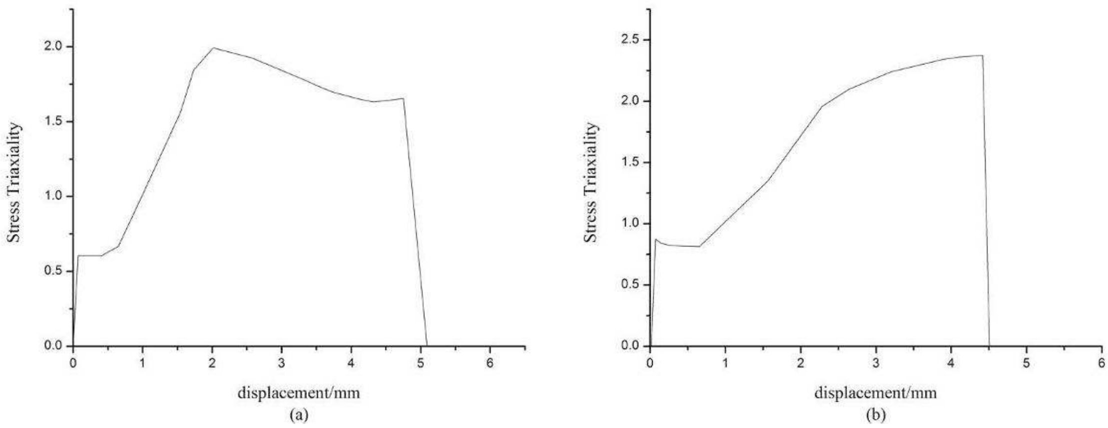

Fig.5. The relationship between stress triaxiality and displacement: (a)Welded connection joint, (b) Welded-bolted connection joint.

Conclusions

1, Based on the micromechanical VGM to predict ductile crack initiation and development, the crack initiation generated in the edge of the weld and grew along the length and the thickness of the weld as displacement increasing.

2, The crack length of welded connection joints was smaller than the welded-bolted connection joints under the same loading condition. It means that the connection stiffness of welded connection joint is better.

3, The VGM fracture models are applicative for the prediction of ductile fracture of steel connection. The VUMAT subroutines can simulate crack initiation and its development, and this simulation technique has reference value for future fracture research.

Acknowledgements

This work was financially supported by the Construction Science & Technology and Building Energy Saving Project Plan of Gansu Province(JK2014-23). The authors would like to thank Professor Sun for her advising.

References

[1] Rice J R, Tracey D. On the ductile enlargement of voids in triaxial stress fields[J]. Journal of the Mechanics and Physics of Solids, 1969, 17: 201-217

[2] Gurson A L. Continuum theory of ductile rupture by void nucleation and growth: part I dash yield criteria and flow rules for porous ductile media. Journal of Engineering Materials and Technology, Transaction of the ASME, 1977, 99(1): 2-15

[3] Changqing Zheng, Keshi Zhang. Analysis of global-cell model using meso-damage mechanics for ductile material. Journal of Inner Mongolia University of Technology, 1999, 31(5): 534-541

[4] Kanvinde A M, Deierlein G G. Void growth model and stress modified critical strain model to predict ductile fracture in structural steels [J]. Journal of Structural Engineering, 2006, 132(12): 1907-1918

[5] Wang Y Q, Zhou H, Shi Y J, Xiong J. Fracture prediction of welded steel connections using traditional fracture mechanics and calibrated micromechanics based models[J]. International Journal of Steel Structures, 2011, 11(3): 351-366

[6] Liao F F, Wang W, Chen Y Y. Parameter calibrations and application of micromechanical fracture models of structural steels [J]. Structural Engineering and Mechanics, 2012, 42(2): 153-174

[7] Kanvinde, A. M., and Deierlein, G. G. (2004). Prediction of Ductile Fracture in Steel Moment Connections During Earthquakes Using Micromechanical Fracture Models. 13th World Conference on Earthquake Engineering, Vancouver, B.C., Canada, Paper No. 297.

Applied Mechanics and Materials Vols. 744-746 (2015) pp 8-12

doi:10.4028/www.scientific.net/AMM.744-746.8

Calculation and Analysis for Limit Bearing Capacity of Steel Tube Reinforced Short Column Piers by Limit Equilibrium Method

LIU Jin Sheng[1, a], QIU Bo[2, b*] and QIAN Yong Jiu[3, a]

[a]School of Civil Engineering, Southwest Jiaotong University, Chengdu, Sichuan 610031, PR china

[b]School of Mechanics and Engineering, Southwest Jiaotong University, Chengdu, Sichuan 610031, PR china

[a]29232446@qq.com, [b]973436645@qq.com, [c] yjqian@home.swjtu.edu.cn

Keywords: Limit Equilibrium Method, Bridge Reinforcement, Steel Tube Reinforcement, Bridge Piers.

Abstract. The existed concrete column reinforced by external steel tube is a common reinforcement technique and widely used in engineering. However, the computational theory on bearing capacity of the reinforced structure is insufficient at present. In the condition that the existed column concrete before completely unloading is reinforced or the initial stress level is low, the mechanics characteristics of reinforced components were analyzed based on the limit equilibrium method, and then the computational equations of the bearing capacity subjected to axial loading after the short column pier reinforced structure had been deduced. Comparing the calculation results with the correspondent experimental data shows that the deduced equation can provide reasonable results for predicting the axial bearing capacity, which provides a support for the computation of the bearing capacity for the reinforcement pier in practice.

Introduction

Currently, the bearing capacity, basic mechanics performance and experimental studies on the concrete reinforced steel tube have already been investigated thoroughly. Based on the large number of experiments of bearing capacity of concrete reinforced steel tube, the constitutive relationship curves of steel tube reinforced concrete were proposed by Han[1]. Zhong [2] proposed the unified theory of the steel tube reinforced concrete. Moreover, the limit bearing capacity of steel tube reinforced concrete was studied by limit equilibrium method, as done by Cai [3, 4] and Gvozdev[5]. All of them provided a good theoretical basis for the analysis of bearing capacity of steel tube reinforced concrete. Unlike the ordinary steel tube reinforced concrete, concrete in the reinforced steel tube is composed of two parts here. Thus, the calculation and theoretical analysis on the bearing capacity of steel tube reinforced concrete short column structure is performed in this work.

Computation and analysis by limit equilibrium theory.

The basic assumptions.

1) The basic assumptions of reinforcement structure are that the core concrete column under axial compression is axisymmetric and the filled concrete and the core concrete are completely bonded without slipping. Meanwhile, the limit yield conditions of steel tube, filled concrete and core concrete are stable. The yield condition of steel tube is employed by Von Mises one. At the same time, the yield of concrete under triaxial compression obeys experiment linear Eqs. (1) and (2) suggested by Cai[3, 4] according to the experimental data, they are listed as follows:

$$\sigma_c = f_c + kp \tag{1}$$

$$\sigma_c = f_c(1 + 1.5\sqrt{\frac{p}{f_c}} + 2\frac{p}{f_c}) \tag{2}$$

2) If the loading is applied in the reinforced structure, the structure stress response of former column after the pressure diffusion is similar to concrete filled steel tube structure subjected to local compression. For reinforced structure, the bearing capacity reduction factor K_{LCO} under local compression can be obtained:

$$K_{LCO} = A \cdot \beta + B \cdot \beta^{0.5} + C \tag{3}$$

The statement of parameters can be found in reference [6].

Derivation of bearing capacity of Reinforcement structure. The static method is used to solve this problem. Force diagrams of steel tube, filled concrete and the core concrete are showed in Figs. 1 and 2.The static equilibrium equation is established by the stress status presented in Fig. 1(a), i.e.,

$$N = K_{LC0}(A_{c1}\sigma_{c1} + A_{c2}\sigma_{c2} + A_s\sigma_1) + A_{s1}\sigma_{s1} \tag{4}$$

where, A_{c1}, A_{c2}, A_s, and A_{s1} are the cross sectional area of core concrete, and longitudinal reinforcement, respectively. σ_{c1}, σ_{c2}, σ_1, and σ_{s1} are longitudinal stress of core concrete, filled concrete, steel tube and longitudinal reinforcement, respectively. f_s is yield limit of steel tube. t_w and t are the thickness of filled concrete and steel tube, respectively. d_c and d_z are diameter of core concrete and reinforced concrete, respectively.

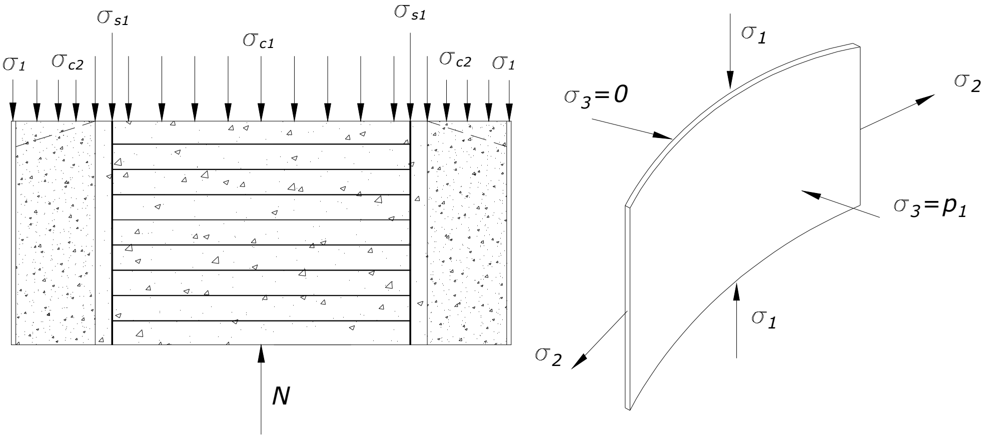

(a) (b)

Fig. 1 Free-body diagram of (a) longitudinal reinforcement column.(b) steel tube infinitesimal body

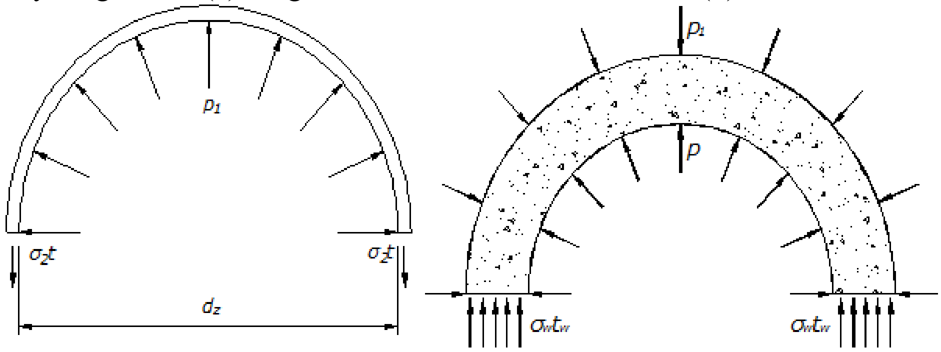

(a) (b)

Fig. 2 (a)Radial force diagram of the steel tube.(b) Force diagram of filled concrete

The pressure acting on the filled concrete can be obtained by static equilibrium conditions described in Fig. 1(b) and Fig. 2(a), i.e.,

$$p = p_1 = \frac{2f_s \cdot t}{d_z} \tag{5}$$

The equilibrium equation followed by Von Mises yield condition for the steel tube in the Fig. 1 can be written as follows:

$$\sigma_1^2 + \sigma_1\sigma_2 + \sigma_2^2 = f_s^2 \tag{6}$$

Combining Eq. (5) and Eq. (6), the longitudinal stress of steel tube σ_1 can be written as follows:

$$\sigma_1=\sqrt{f_s^2-\frac{3}{4}(\frac{d_z p}{2t})^2}-\frac{d_z p}{4t} \tag{7}$$

The concrete in reinforced structure consists of core and filled concretes. θ_1 is confinement index of reinforcement steel tube for column core concrete, and can be written as $\theta_1=\frac{A_s f_s}{A_{c1} f_{c1}}$. Since the relationship between As and Ac1 in thin-wall steel tube can be written as $\frac{A_s}{A_{c1}}=\frac{4d_z\cdot t}{d_c{}^2}$. Expression of θ_1 can be further obtained as $\theta_1=\frac{4d_z t}{d_c{}^2}\cdot\frac{f_s}{f_{c1}}$. And then, the equation can be derived as follows:

$$\frac{p}{f_{c1}}=\frac{f_s}{f_{c1}}\cdot\frac{2t}{d_z}=\frac{1}{2}\theta_1(\frac{d_c}{d_z})^2 \tag{8}$$

The yield condition of core concrete and filled concrete complies with the Eq. (1). Then substituting Eq. (6) into Eq.(4) yields:

$$N=K_{LCO}\left(A_{c1}\left(f_{c1}(1+k\frac{p}{f_{c1}})\right)+A_{c2}\left(f_{c2}(1+k\frac{p}{f_{c2}})\right)+A_s(\sqrt{f_s^2-\frac{3}{4}(\frac{d_z p}{2t})^2}-\frac{d_z p}{4t})\right)+A_{s1}\sigma_{s1} \tag{9}$$

The load N is a function of the lateral pressure p showed in the Eq.(9), the maximum load N_{max} can be obtained by derivative load N on the lateral pressure p and set $dN/dp=0$.

Since the parameter k is set as a value of 4 here, the equation can be derived as follows:

$$\frac{p^*}{f_{c1}}=\frac{1}{2}\theta_1(\frac{d_c}{d_z})^2 \tag{10}$$

Since the steel rebar is led to the yielded state when the reinforcement structure is in limit state, Eq.(10) can be substituted into Eq.(9) yields:

$$N=K_{LCO}A_{c1}f_{c1}\left[1+2(\frac{d_c}{d_z})^2\theta_1\right]+K_{LCO}A_{c2}f_{c2}\left[1+2\frac{d_c^2}{d_z^2}\cdot\frac{f_{c1}}{f_{c2}}\cdot\theta_1\right]+A_{s1}f_{y1} \tag{11}$$

Furthermore, nonlinear Eq. (2) is taken for the concrete yield condition, and the Eq. (4) can be derived as follows:

$$N=K_{LCO}(A_{c1}f_{c1}(1+1.5\sqrt{\frac{p}{f_{c1}}}+2\frac{p}{f_{c1}})+A_{c2}f_{c2}(1+1.5\sqrt{\frac{p}{f_{c2}}}+2\frac{p}{f_{c2}})+A_s(\sqrt{f_s^2-\frac{3}{4}(\frac{d_z p}{2t})^2}-\frac{d_z p}{4t}))+A_{s1}\sigma_{s1} \tag{12}$$

The load N is a function of the lateral pressure, p , the maximum load N_{max} can be obtained by derivative load N on the lateral pressure p and set $dN/dp=0$, the Eq.(12) can be derived as follows:

$$A_{c1}f_{c1}(\frac{1.5}{2\sqrt{f_{c1}p^*}}+\frac{2}{f_{c1}})+A_{c2}f_{c2}(\frac{1.5}{2}\sqrt{\frac{1}{f_{c2}p^*}}+\frac{2}{f_{c2}})+A_s(\frac{-\frac{3d_z^2}{8t^2}p^*}{2\sqrt{f_s^2-\frac{3d_z^2}{16t^2}p^{*2}}}-\frac{d_z}{4t})=0 \tag{13}$$

The limiting value of Eq. (13) can be obtained by considering the condition of the vertical stress of steel tube $\sigma_1^*=0$ and $\sigma_2^*=f_s$ which is limit equilibrium conditions of pure confinement effect coated steel tube, and can be written as:

$$p^*=\frac{f_{c1}d_c^2}{2d_z^2}\theta_1 \tag{14}$$

Therefore, the approximate calculation value of the Eq. (14) which about the ultimate bearing capacity of the reinforcement structure can be written as follows:

$$N = K_{LCO}(A_{c1}f_{c1}(1+1.5\sqrt{\frac{1}{2}\cdot\frac{d_c^2}{d_z^2}\theta_1} + (\frac{d_c}{d_z})^2\theta_1) + A_{c2}f_{c2}(1+1.5\sqrt{\frac{f_{c1}d_c^2}{2f_{c2}d_z^2}\theta_1} + \frac{f_{c1}d_c^2}{f_{c2}d_z^2}\theta_1)) + A_{s1}f_{y1} \quad (15)$$

It is well-known that the yield condition of concrete in three-dimensional pressure condition is different, and the different strength classes between core concrete and filled concrete in normal reinforced structure is few. Here, substituting Eq. (15) into Eq. (11), the boundary value of intersection with two equations can be obtained as $[\theta_1] = 1.125d_z^2/d_c^2$. For safety, when $[\theta_1] \le 1.125d_z^2/d_c^2$, the value of N should be got by Eq. (11), otherwise Eq. (11) should be used.

Due to a same structure form between reinforced structure considering here and the concrete filled steel tube subjected to local compression, refering calculation formula for the concrete filled steel tube subjected to local compression $N_{ul} = f_c A_1(1+\sqrt{\theta}+\theta)\beta$, the bearing capacity of steel tube reinforced the existing concrete structure can be obtained as:

$$N = K_{LCO}(A_{c1}f_{c1}(1+\sqrt{(\frac{d_c}{d_z})^2\theta_1} + (\frac{d_c}{d_z})^2\theta_1) + A_{c2}f_{c2}(1+\sqrt{\frac{f_{c1}d^2{}_c}{f_{c2}d^2{}_z}\theta_1} + \frac{f_{c1}d^2{}_c}{f_{c2}d^2{}_z}\theta_1)) + A_{s1}f_{y1} \quad (16)$$

The experimental verification. In order to validate the computational equation of limit capacity of the reinforced structure, the steel tubereinforced concrete column is used as compressive short column specimen. A test group consists of four specimens. The reinforcement method of the specimen is welded and ferruled by steel tubes after the original concrete column finishs pouring. Before the reinforcement, the surface of the original column concrete should be roughened. And then, the gap between the steel tube and the original column should be filled with new concrete. The specific size is shown in table 1. Full-section loading is selected as the loading case.

Table 1 Size of specimen (mm)

specimen numbers	size of original column		Thickness of steel tubes	thickness of filled concrete	diameter of longitudinal	diameter and spacing of stirrup
	diameter	height				
S-0	250	1000	0	0	6φ12	φ6φ150
S-1	250	1000	2	25	6φ12	φ6φ150
S-2	250	1000	3	25	6φ12	φ6φ150
S-3	250	1000	4	25	6φ12	φ6φ150

where, S-0 represents a unreinforced original column, S-1，S-2，S-3 represent the reinforced specimens. The standard strength of filled concrete and original column specimen are 38.1MPa and 36.3MPa.

Material properties of steel tubes and rebars are shown in table 2.

Table 2 Material properties of steel tubes and rebars

specimen	thickness of steel tube/ diameter of rebar (mm)	ultimate strength f_{uk} (MPa)	yield strength f_{yk} (MPa)	tensile Strength of weld f_{tk}(MPa)
steel tube	2	344	271	324
	3	316	262	298
	4	336	279	302
rebar	6.0	436	336	—
	12.0	476	350	—

The limit bearing capacity of pier after reinforced obtained by test is shown in table 3.

Table 3 Rhe test and calculational values for bearing capacity of reinforced conrete column

specimen numbers	test value $N_{e.}$(KN)	Calculation value $N_{c.}$(KN)	$N_{c.}/N_{e.}$
S-0	1460	—	—
S-1	3493	3348	0.95
S-2	3987	3814	0.96
S-3	4401	4464	1.01

N_c and N_e shown in table 3 represent the calculated value by the derived equation and experiment value, respectively. The results in the table 3 show that the computation values agree with experiment values well.

Summary

Based on the limit equilibrium method, a new computational formula is proposed to predict the axial bearing capacity of steel tube reinforced short column piers. Comparing the calculation results by the proposed formula with the correspondent experimental data shows that the proposed formula can provide a reasonable result for predicting the axial bearing capacity. The new calculating method of bearing capacity of reinforced structure that has clearly mechanics concept could be widely applied in engineering practices.

References

[1] L.H. Han, Y.F. Yang: *Modern steel tube-confined concrete structure technique* (China Architecture & Building Press, Beijing 2004).

[2] S.T. Zhong: *Steel tube-confined concrete structure*, (Tsinghua University Press, Beijing 2003).

[3] S.H. Cai: *Modern steel tube-confined concrete structure* (China Communications Press Press, Beijing 2003).

[4] S.H. Cai, Z.S. Jiao: Beijing: Journal of Building Structures. Forum Vol. 13-29 (1984), p.5 (6)

[5] W.B. Yuan: *The calculation of structure bearing capacity by limit equilibrium method* (China Architecture & Building Press, Beijing 1958).

[6] W. Liu: Research on work mechanicm of concrete-filled steel tube structure under local compression, (Fuzhou University press, Fuzhou, 2005).

Applied Mechanics and Materials Vols. 744-746 (2015) pp 13-16

doi:10.4028/www.scientific.net/AMM.744-746.13

Collapse Reason Analysis of a Steel Truss Building under Snow Disaster

Haoxiang Guo, Long Chen, Dan Yang and Hongyuan Tang

College of Architecture and Civil Engineering, Xihua University, Chengdu 610039, China

Corresponding author: Hongyuan Tang ,mryuanye@qq.com

Keywords: Steel truss structure; Collapse; Snow disaster.

Abstract. This paper analyzes the reason of a steel truss building which collapsed under a snow disaster. Firstly, the investigation and inspection in site are introduced. Secondly, based on the on site work, such as the property of the metal materials and the quality of the welding joint, the status of the structure is comprehensively determined. Thirdly, through calculation with the former results, the reason of the collapse accident is obtained. Finally, some related suggestions are proposed for the design and construction of this kind of structure.

Introduction

During a snow disaster, an auto repair factory collapsed. The building is about 1560 m^2, whose steel truss roof spans 20 m. The steel columns distance is 6 m, which are all 4.95 m height. The outside diameter of steel columns is 140 mm and thickness is 3 mm. The outside diameter of up and down chords in the steel arch truss is 60 mm, and thickness is 2.5 mm. The outside diameter of belly bars is 25 mm, and thickness is 2.5 mm. Purlins are C95x36x16x2 cold-formed steel, whose distances are 1.2 m. Structural plan layout is shown in Fig. 1.

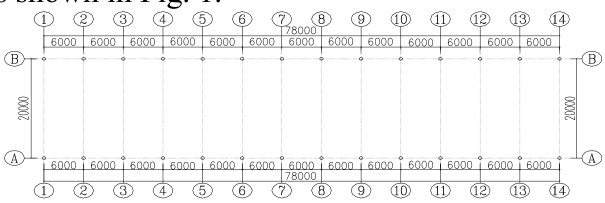

Fig. 1 Structure plan layout

In Site investigation and inspection

In site investigation: The collapsed situation is shown in Fig. 2. It shows that both sides columns in the structure collapsed inward. The field investigation found that the building has neither the construction drawings of the project, and nor construction records. So the actual situation and the structure can only obtained through asking the construction engineers and the on site survey.

Fig. 2 Collapse situation

Structure inspection: The quality of the weld spot checks was carried out and no weld cracks were found. Neither welding tumor, nor obvious weld defects were detected. In addition, the mechanical properties of truss and columns which were on site random sampled were tested. And the results meet with the design requirements. The bearing capacity of various types of connections between components was examined. The failure phenomenon was not found.

Collapse situation analysis

Snow load analysis: Overload snow is the direct reason of the accident, the overload from the concerted action. There are three main problems [1]:

Firstly, direct excessive snowfall. Meteorological Department data shows that most snowfall in this southern region is the largest snowstorm in nearly five decades. More than structural load norms (GB50009-2012) [2] digital requirements, and snow loads in the workshop area of 0.35 kN/m^2.

Secondly, it is the combination of rain and snow. Due to the relatively high temperature of the southern region， snowfall in the process will be accompanied by rain. The rains integrate into snow, when the temperature decreases, the rain in the snow freezes. The density is much greater than the general form of snowfall density, which increases the roof load. In addition, there are no corresponding insulation measures in the southern buildings, once hit by continuous low temperatures, snow and ice will accumulate on the building, it is difficult to melt. It is the same as a long period of additional external load which is equivalent to the building.

Thirdly, the problems caused by melting snow. Because of the low temperature status is not complete in the snow area; it will form the snow melt. When the surfaced snow melts, the building drain has not yet been thawed, snow melt into water and flow to the lower height, then integrate into snow which increase the density of this area. Statistics show that: natural snow density is about 150 ~ 200 kg/m^3, and the melted snow density can even reach 500 ~ 700 kg/m^3, According to reports of witnessing personnel, When the snow has just started, there are about 2cm thick layer of ice on the roof of the shop when the block collapsed.

Finally, overloading effect of snow load is not the only reason to direct snowfall. Especially in southern China, complex weather conditions (Not thorough enough low temperature, temperature fluctuations larger) makes the snow situation much worse after snow. Water integrates into snow then form into ice and snow (because of the snow melts into water, and quickly freeze into ice, and accumulates in the local place which causes the increased local road), it is beyond the scope of the snow condition of the standard.

Purlins Analysis: According to Cold-formed thin-walled steel structure technical specifications (GB50018-2002) [3], purlins should be set with at least a brace in 6 m span, but there is no brace on the spot. And the connection between the trussed and purlins is not strong enough, there are only drill screws used to fix compound trusses in the top flange of the truss, can't ensure that out-of-plane stability of the turss.

The purlin is bidirectional bending members, due to wind loads on roof system sometimes pressure, sometimes suction. Therefore, according to the two load cases check the strength and overall stability of trusses. The 1st load case is equal to 1.2 times structure weight + 1.4 times (Live load + 0.9 times fouling + 0.6 times wind load). The 2nd load case is equal to structure weight + 1.4 times wind suction loads. With equation (1) and equation (2), the 1st load case checks the truss strength and overall stability. The 2nd load case only checks the overall stability of the truss flange under pressure situations.

$$\frac{M_x}{W_{enx}} + \frac{M_y}{W_{eny}} \le f \quad (1)$$

$$\frac{M_x}{\varphi_b W_{enx}} + \frac{M_y}{W_{eny}} \le f \quad (2)$$

Results show that the strength, overall stability and deflection of trusses not meet the design requirements. And the overall stability of the truss occurs before the strength damage. This may cause almost all truss rollover occurs, severe bending completely consistent, which is shown in Fig. 3.

Fig. 3 Purlins overall rollover deformation

Stress analysis of trusses: The truss structure calculation diagram is shown in Fig. 4, which is obtained from the on site inspection. Firstly, the structure shown in Fig. 4, in theory, is not a static set, but a variable system. It is indicated by the relative positions of the ABCD four nodes.

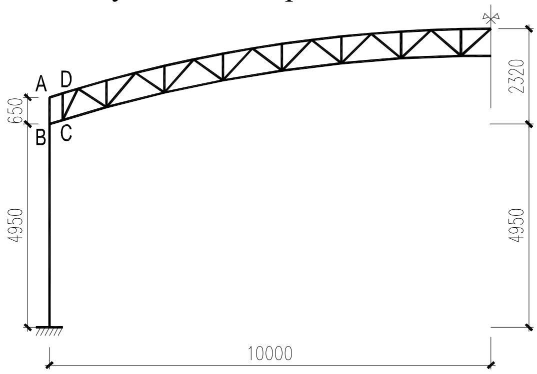

Fig. 4 Structure model

The structure is a symmetrical structure. According to the weather, the truss situation suffered loads are symmetrical. In addition, the overall instability and rollover damage of the truss are occurred, which indicates truss outside of the structure can not guarantee a stable truss plane. It is shown in Fig. 5.

Fig. 5 Truss deformation

Stress analysis of steel columns: When analyzing steel columns, using load 1st load case mentioned above. Through the calculation and analysis, steel cylinder moment is shown in Fig. 6.

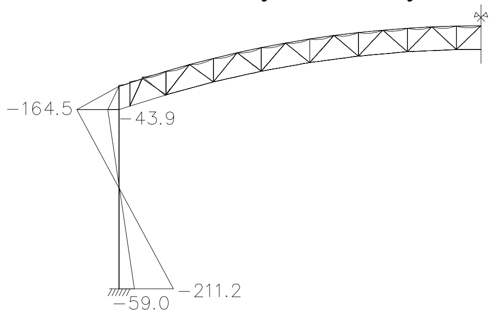

Fig. 6 Steel columns moment

Through Fig. 6, the structure calculation diagram point B in the vicinity of the steel columns and column foot larger than the moment, after checking showed that: steel columns in the carrying capacity of these two places are not enough, the intensity of the destruction occurred. This site is completely consistent with the checking result, damage steel columns is shown in Fig.7 (a) and (b) below.

(a) B position bending failure; (b) The foot of the steel column bending failure

Fig. 7 Steel columns failure

Conclusions and recommendations: Based on the above analysis of reasons for the collapse of a light steel structure, trying to make a few suggestions from the following aspects:

Firstly, standardize the construction arrangements and establish credibility mechanism. Light steel housing design and construction of strict management is the key. The auto repair factory in this snowstorm phenomenon reflects the collapse of the construction market confusion, as some manufacturers design their own, their own construction; On the design drawings are not strictly audited, thoughtful enough to consider structural measures, even as the cost down, reduce excessive "reasonable" amount of steel, making further reduce the carrying capacity of reserves; Therefore, the construction unit should employ the appropriate qualifications held by the construction and design of the unit in order to better ensure the quality of the project.

Secondly, actively carry out the experimental study of steel sheet, organization "pressing sheet metal design construction regulations" (216-88) YBJ revision or reweave work as soon as possible. The procedures for the pressed steel sheet the popularization and application of new technology played a very good guidance, with the emergence of new materials, the progress of technology, the development of the discipline has far cannot satisfy the need.

Finally, experiments for the portal rigid frame light steel structure should be strengthened. The rules for it should be revised as soon as possible [4]. The current rule in our country is less than the MBMA specified. In addition, the United States in the design manual for plant height across, parapet, height of roof house are prescribed according to the snow on the ground pressure and the actual size according to the formula to calculate the snow load increases value, the maximum can reach 4 ~ 5 times, this area also is larger than the snow distribution coefficient of 2.0, regulations when the revision should consider these problems.

Acknowledgments:

This is a project supported by scientific research fund of Sichuan provincial education department, Xihua University key fund, the Innovation Fund of Postgraduate of Xihua University.

References

[1] Y. Q. Wang, Z. W. Hu, Y. J. Shi, Y. Zhang and M. Liu: “Portal frame light steel structure houses the snow disaster accident analysis and reflection on”. Journal of Civil Engineering, 2009, 42, 65-70. (In Chinese)

[2] Load code for the design of building structures. (In Chinese)

[3] Technical specification cold-formed thin-wall steel structures. (In Chinese)

[4] X.Y. Gong: “Storm of light steel structure housing”. Journal of Steel Structure, 2007, 22, 89-91. (In Chinese)

Applied Mechanics and Materials Vols. 744-746 (2015) pp 17-24

doi:10.4028/www.scientific.net/AMM.744-746.17

Comparative Study of the Loads Acting on the Operating Cardanic Transmission in the Closed and Open Loop Configurations

Eugen Avrigean[1a,]

[1] Lucian Blaga University, no. 10, Victoriei Blvd., Sibiu, 550024, Romania
[a]eugen.avrigean@ulbsibiu.ro

Keywords: cardanic transmission, comparative analysis, finite elements.

Abstract. On the basis of a comparative study, this paper aims to determine the maximum loads that can occur in operating conditions on the cardanic transmission assembly of motor vehicles in the open or closed loop configurations. The research is conducted under static conditions using finite elements and shows the components with their maximum values obtained in normal operating conditions.

Introduction

The cardanic transmissions of the motor vehicles and various industrial machines belong to the kinematic chain of transmission of the rotary motion from the engine to the drive wheels or to the moving parts. [1]

Figure 1. Types of Cardan Transmissions made by the Eurocardan Company [6]

The cardanic transmission refers to a set of machine parts (joints, shafts, intermediate bearings etc.) used for the remote transmission of the mechanical energy by rotation without torque gain between units with a variable or invariable position in space. By judicious design of these machine parts and of the execution technology, an increase of the operational reliability and a low metal consumption are ensured.[3]

From a constructive point of view, the cardanic transmissions are mechanisms consisting of an assembly of machine parts – shafts, cardan joints, safety couplings, dampers, intermediate bearings etc., which constitute an independent functional unit, and serve for the distant transmission, without amplification of the torque, between different parts of the same machine or between different machines, their relative position being variable. [2]

Static Analysis Applied to the Cardanic Transmissions Assembly

The software employed for the finite element method analysis is Cosmos, a product incorporated into the Solidworks software package, which, through its facilities and the accuracy of its results is often used in researching the static and dynamic behavior of the technological system components. Actually, the Solidworks program is used for the geometrical modeling of the cardanic transmission components and for their assembling, whereas the Cosmos program, based on the geometry undertaken from the Solidworks, generates the finite element network, idealizes the contacts between the components and allows the application of strains and stresses. The Cosmos program has a set of modules dedicated to specific areas, such as: the analysis of structures in general, the fluid mechanics, and the thermal analysis. Each module, in turn, owns a complete set of analyses for linear or nonlinear, static or dynamic problems, through which a complete research can be conducted. [5]

The geometrical model used in the case of the static analysis was created in two configurations: one with a closed loop transmission and the other one with an open loop transmission (the maximum opening between the splined shaft and the splined hub is 180 mm). The cardanic transmission assembly of the Dacia 1307 vehicle was modeled on the following components: the flange towards the end of the actuator, Φ 630 tube, splined shaft, splined hub, cardan cross 1, hub fork 1, Φ 730 tube, hub fork 2, cardan cross 2 and the flanged fork at the end towards the differential and then the entire model was assembled. The bearings were also modeled and they were mounted on the ends of the cardan crosses. Figure 2 presents the model of the transmission in closed loop configuration.

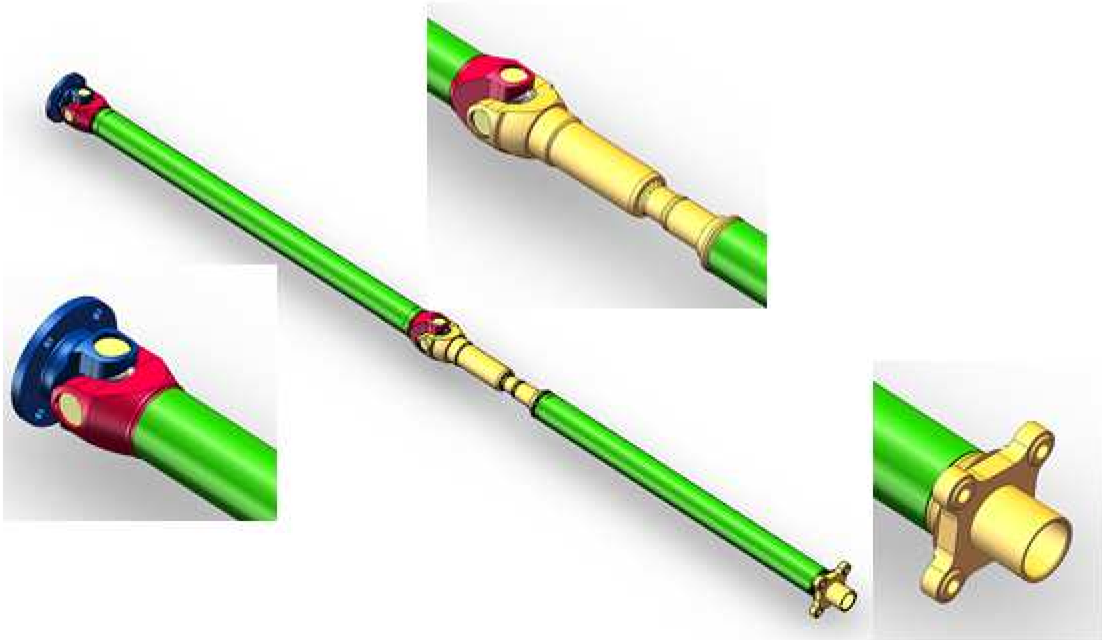

Figure 2. The cardanic transmission assembly modeled with Solidworks (general view)

In order to obtain a model with a behavior as close to reality as possible and trying to reach the shortest running time, the insignificant details have been removed (small fillet radii or niches) and the inhomogeneous areas on the structure were approximated with homogeneous finite elements. We thus obtained a uniform network of finite elements, shown in figure 3 (closed loop configuration).

The static analysis aims to determine the state of stresses and strains in loading the model in a static regime. This analysis was applied to the parameterized model of the cardanic transmission assembly of a Dacia 1307 vehicle, in the two types of construction: the closed loop transmission and the open loop transmission. The static behavior was studied in both cases, in order to compare the results of the finite element analysis on the cardan transmission structural elements.

In order to conduct a static analysis on the end towards the differential, we apply strains on the flange fork, in the form of annulling the degrees of freedom, so that this end is fixed. At the end located in the actuator, we apply a constant moment of 300 Nm. The position of strains and stresses can be observed in figure 3.

The materials that the cardanic transmission components are made of are the following: 1-flange fork, STAS 880 – 80; 2- hub fork, STAS 880 – 80; 3- hollow shaft encoder, STR 302-88; 4-cardan cross, 18 Mn Cr 10 – STAS 791 – 88; 5- safety ring, 6- needle roller bearing, 7- axle yoke, OLC 45, STAS 880 – 80; 8- intermediate shaft, 40 Cr 10 – STAS 791 – 88; 9- hollow shaft encoder, 10- flange, STAS 880 - 80.

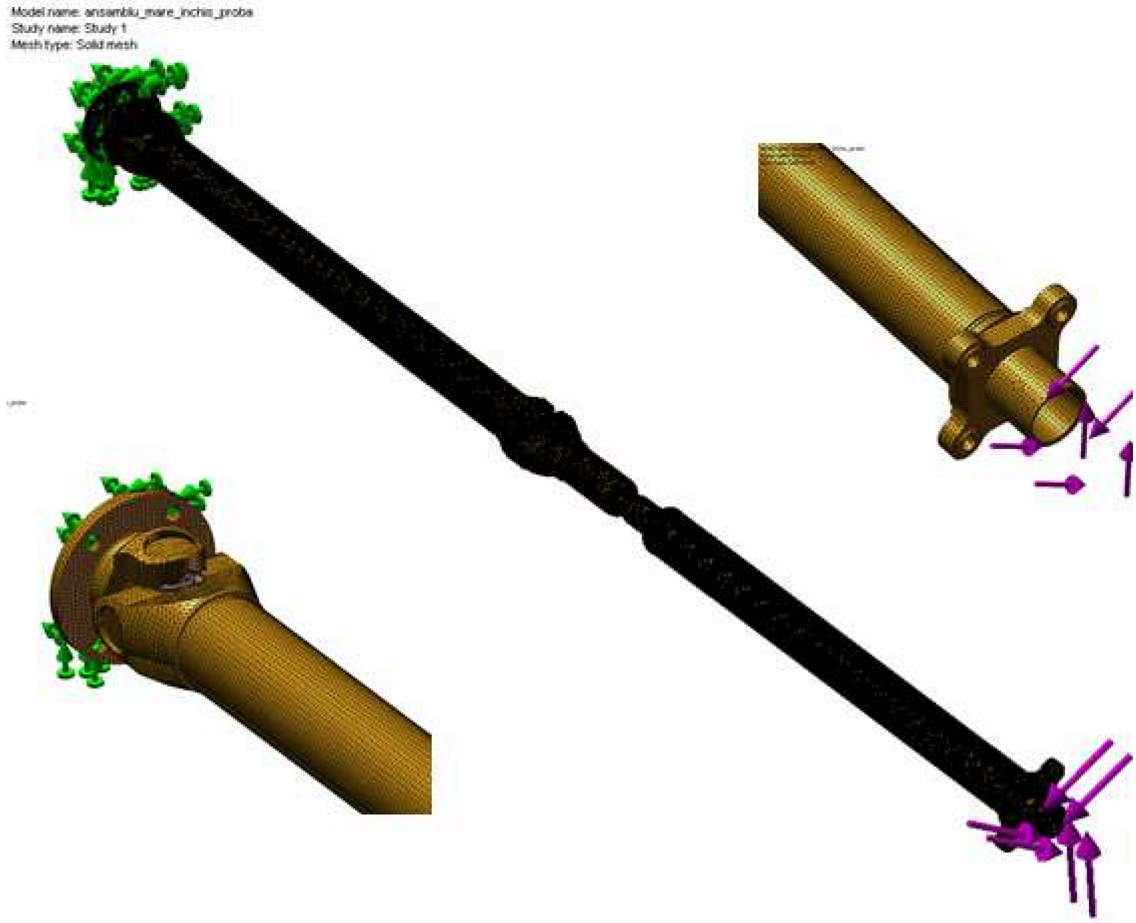

Figure 3. Application of stresses and strains on the cardanic transmission (general view)

The sequence of figures 4 to 11 presents the variation graphs of the von Mises stress, of the main stresses σ_1, σ_2, σ_3, the variation graphs of the unit strain, of the main strains ε_1, ε_2, ε_3, the graph of the resulting nodal displacements and the graph of the safety factor for the cardanic transmission assembly.

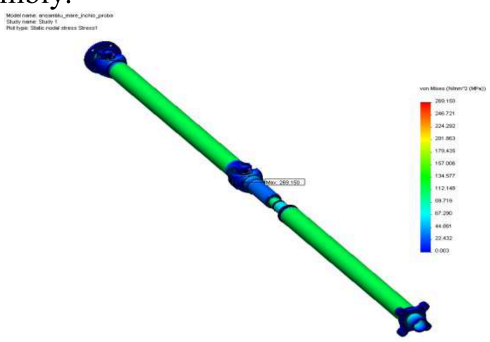

Figure 4. Variation graph of the von Mises stress – closed loop transmission (σ_{VM}=269,15 MPa)

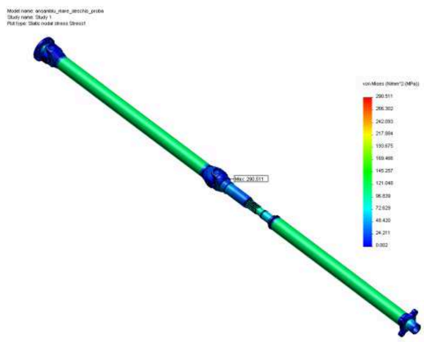

Figure 5. Variation graph of the von Mises stress – open loop transmission (σ_{VM}=290,51 MPa)

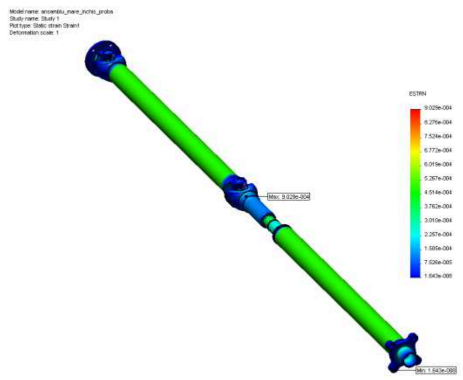

Figure 6. Variation graph of the unit strain – closed loop transmission (ε_{VM}=9,03·10^{-4})

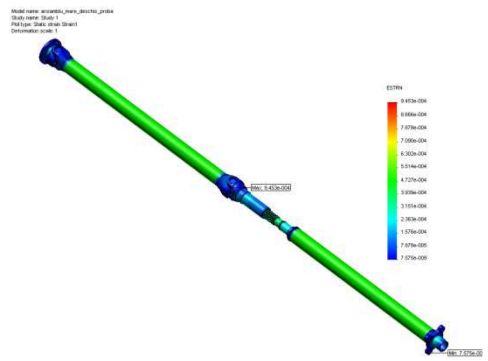

Figure 7. Variation graph of the unit strain – open loop transmission (ε_{VM}=9,45·10^{-4})

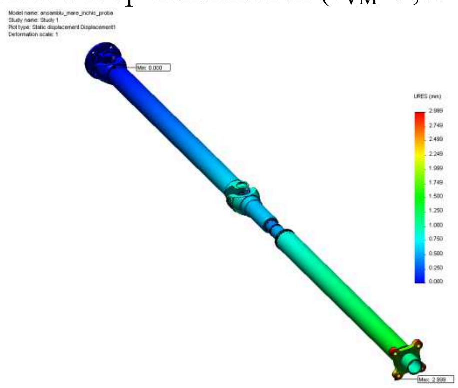

Figure 8. Graph of the resulted nodal displacements – closed loop transmission (d_n=2,99 mm)

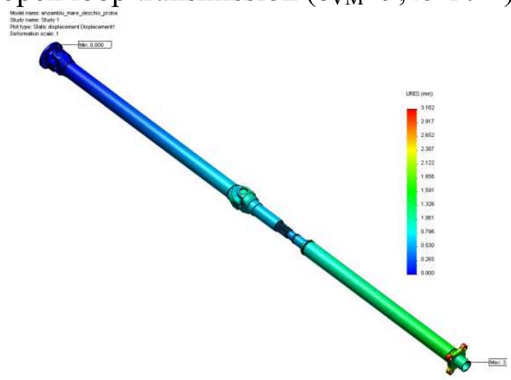

Figure 9. Graph of the resulted nodal displacements – open loop transmission (d_n=3,182 mm)

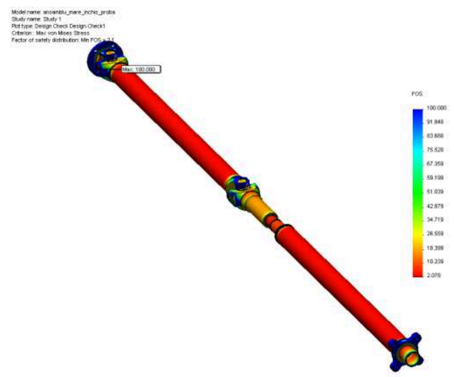

Figure 10. Graph of the safety factor – closed loop transmission (c=2,078)

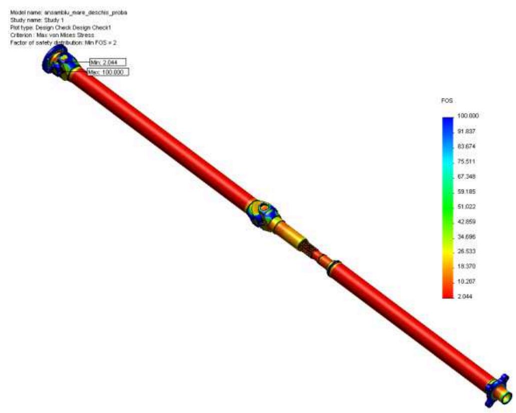

Figure 11. Graph of the safety factor – open loop transmission (c=2,044)

By analyzing the variation graphs of the von Mises stress for the entire cardanic transmission assembly (fig. 4 to 11) we notice that its maximum value is 290.511 MPa, which is obtained on the cardan cross 2 (the cardan cross situated closer to the vehicle's differential) in the case of the open loop transmission. For the closed loop transmission, the maximum value of the von Misses stress is also found in the cardan cross 2, but the maximum value is smaller (269.15 MPa). The von Mises stress in the other components of the transmission ranges from 0 to 180 MPa.

The sequence of figures 4 to 11 shows the variation graphs of the von Mises stress, the variation graphs of the unit strain, the graphs of the resulting nodal displacements and the graph of the safety factor for the components of the cardanic transmission in the two analyzed configurations: closed loop transmission and open loop transmission.

The maximum values for the cardanic transmission components shown in table 1 were obtained through the performed static analysis.

Table 1. Maximum values obtained on the cardanic transmission components

No.	Denomination of cardanic transmission components	Closed loop transmission				Open loop transmission			
		σ_{VM} [MPa]	ε_{VM} [10^{-3} mm]	d_n [mm]	c	σ_{VM} [MPa]	ε_{VM} [10^{-3} mm]	d_n [mm]	c
1.	Flanged fork	97.02	0.3	0.02	5.46	97.07	0.3	0.02	5.46
2.	Cardan cross 1	266.41	0.053	0.87	3.0	265.41	0.053	0.9	3.01
3.	Hub fork 1	77.6	0.17	0.067	8.53	80.7	0.17	0.067	8.43
3.	Hub fork 2	72.53	0.18	0.95	9.19	70.50	0.23	1.04	8.23
5.	Cardan cross 2	269.15	0.9	0.86	2.97	290.51	0.95	0.93	2.75
6.	Axle yoke	141.28	0.31	1.01	3.75	151.62	0.30	1.1	3.50
7.	Intermediate shaft	135.59	0.46	0.84	3.91	126.45	0.47	0.96	4.19
8.	Flange	91.2	0.38	2.99	5.81	90.6	0.38	3.18	5.85

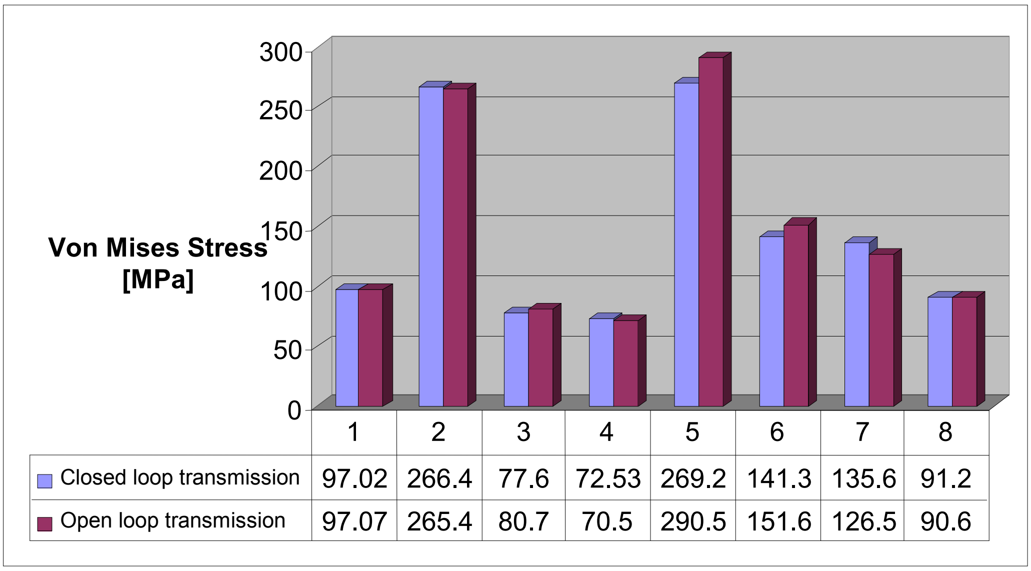

Figure 12. Von Mises stress for the components of the cardanic transmission

1. Flanged fork, **2**. Cardan cross 1, **3**. Hub fork 1, **3.** Hub fork 2,

5. Cardan cross 2, **6**. Axle yoke, **7**. Intermediate shaft, **8**. Flange

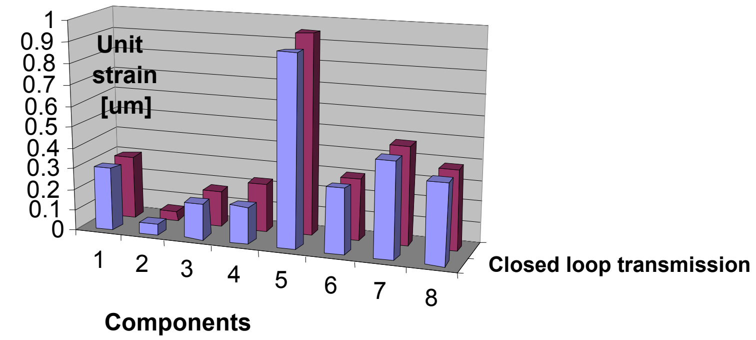

	1	2	3	4	5	6	7	8
Closed loop transmission	0.3	0.053	0.17	0.18	0.9	0.31	0.46	0.38
Open loop transmission	0.3	0.053	0.17	0.23	0.95	0.3	0.47	0.38

Figure 13. Unit strain of the components of the cardanic transmission

1. Flanged fork, **2**. Cardan cross 1, **3**. Hub fork 1, **3.** Hub fork 2,

5. Cardan cross 2, **6**. Axle yoke, **7**. Intermediate shaft, **8**. Flange

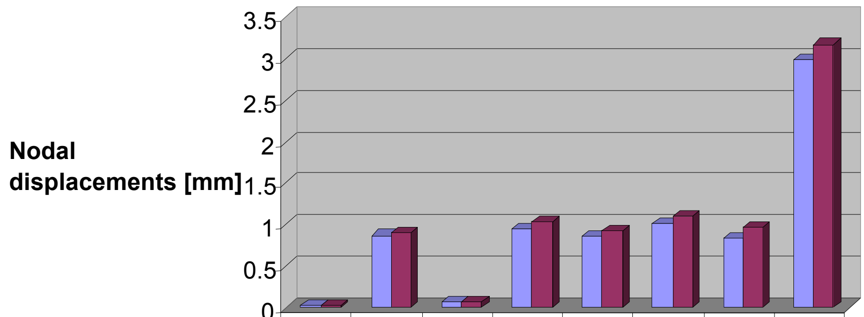

	1	2	3	4	5	6	7	8
Closed loop transmission	0.02	0.87	0.067	0.95	0.86	1.01	0.84	2.99
Open loop transmission	0.02	0.9	0.067	1.04	0.93	1.1	0.96	3.18

Components

Figure 14. Nodal Displacements for the components of the cardanic transmission

1. Flanged fork, **2**. Cardan cross 1, **3**. Hub fork 1, **3.** Hub fork 2,

5. Cardan cross 2, **6**. Axle yoke, **7**. Intermediate shaft, **8**. Flange

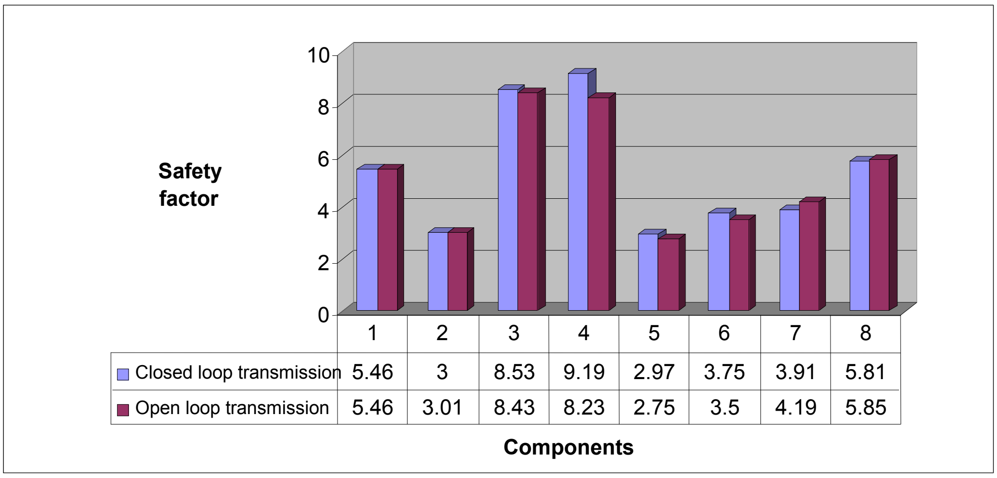

	1	2	3	4	5	6	7	8
Closed loop transmission	5.46	3	8.53	9.19	2.97	3.75	3.91	5.81
Open loop transmission	5.46	3.01	8.43	8.23	2.75	3.5	4.19	5.85

Figure 15. Safety Factor for the components of the cardanic transmission
1. Flanged fork, **2**. Cardan cross 1, **3**. Hub fork 1, **3.** Hub fork 2,
5. Cardan cross 2, **6**. Axle yoke, **7**. Intermediate shaft, **8**. Flange

By analyzing the previous charts, it is observed that the part which is loaded the most is the cardan cross, with the values presented above.

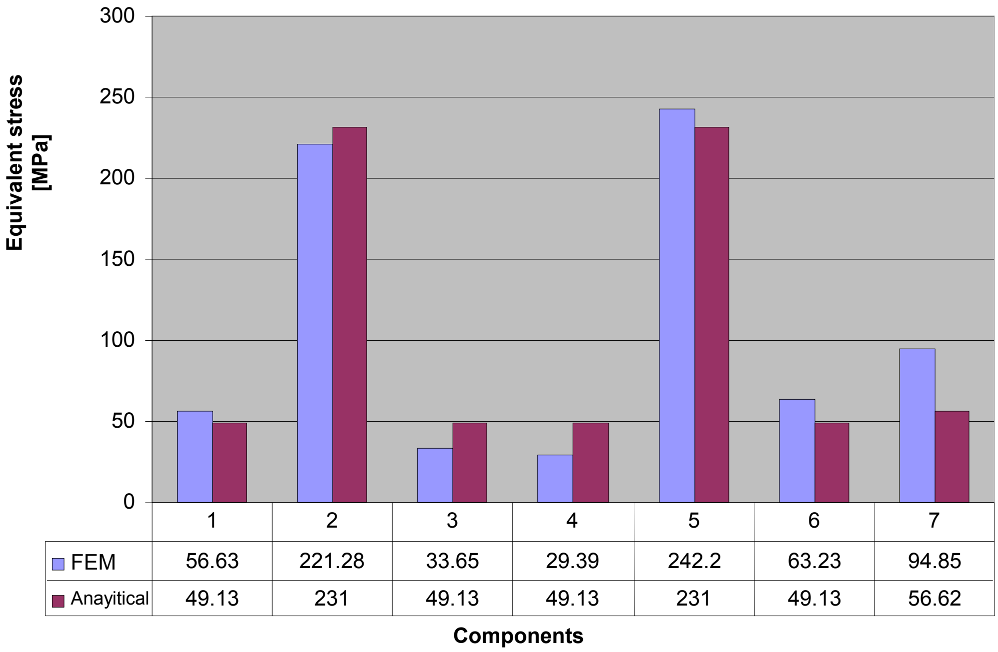

	1	2	3	4	5	6	7
FEM	56.63	221.28	33.65	29.39	242.2	63.23	94.85
Anayitical	49.13	231	49.13	49.13	231	49.13	56.62

Figure 16. Safety Factor for the components of the cardanic transmission
1. Flanged fork, **2**. Cardan cross 1, **3**. Hub fork 1, **3.** Hub fork 2,
5. Cardan cross 2, **6**. Axle yoke, **7**. Intermediate shaft.

Conclusions

- the cardanic transmission of a Dacia 1304/1307 vehicle was chosen in order to exemplify the theoretical and experimental researches on a real physical model;
- a checking calculation was performed for the chosen cardanic transmission assembly under a normal stress of 300 Nm in operation, comparing the results with those given in the literature, and observing that the obtained values comply with the given material values;

- after modeling the cardanic transmission, the closed loop and open loop configurations were chosen, resulting that the open cardan transmission is loaded the most, and therefore this will be used in the analysis;
- the analysis of the von Mises stress variation graphs for the entire cardanic transmission assembly shows that its maximum value is 290.51 MPa, a value that is obtained on the cardan cross 2 (the cardan cross which lies closer to the vehicle differential) in the case of the open loop transmission. For the closed loop transmission, the maximum value of this stress is also found in the cardan cross 2, but it is lower (269.15 MPa). The von Mises stress in the other components of the transmission ranges between 0 and 180 MPa;
- the results obtained from the static analysis were focused on determining the stresses and strains of the assembly components, but also on the evolution in time of certain characteristic measurements (stresses, displacements and velocities) for four nodes belonging to the finite element mesh, presenting the Von Mises stresses and the nodal displacements at two points in time t = 0.31 s and t = 0.5 s (at the moment when the load is maximum) for the entire assembly; 255 MPa.
- the values of the stresses and strains obtained in functioning conditions fall within the values given in the literature;
- a future analysis is suggested, concerning the case in which the value of the torque activating the cardanic transmission accidentally increases to a high value and determining the tendency of the cardanic transmission components to break.

References

[1]] Cristescu, D. s.a. Automobilul. Construcţie.Funcţionare.Depanare. Technical Publishing House, Bucharest, 1986.

[2] Dudita, Fl. Transmisii cardanice. Technical Publishing House, Bucharest, 1966.

[3] Sofonea, G., Fratila M., Vasiloaica, C., Pascu, A., Avrigean, E. Rezistenta materialelor - Indrumar de laborator. "Lucian Blaga" University of Sibiu Publishing House, 2000.

[4] Radu, GH. N., Munteanu, M. GH., Bit, C. S., Rezistenţa materialelor şi teoria elasticităţii, Vol. III. Macarie Publishing House, Targoviste, 2000.

[5]] Oleksik, V., Pascu, A.M. Proiectarea optimala a maşinilor si utilajelor, “Lucian Blaga” University of Sibiu Publishing House, 2007.

[6] www.eurocardan.it

Applied Mechanics and Materials Vols. 744-746 (2015) pp 25-28
© (2015) Trans Tech Publications, Switzerland
doi:10.4028/www.scientific.net/AMM.744-746.25

Comparison of Stability and Deformation Performance of Cable-Braced Grid Shell with Different Section Forms of Steel Tube

Zhiying Zhang[1],Xun Zhao[1,a]and HongyangWei[1]

[1] School of Human Settlement and Civil Engineering, Xi'an Jiaotong University,Xi'an, Shaanxi, 710045,China

[a]xjtu.zx@stu.xjtu.edu.cn

Key words: Cable-bracedgridshell, Section forms, Stability, Deformation performance

Abstract. Cable-braced grid shell is a hybrid structure combined rigid steel tube and flexible cable. The paper presents the variation law of stability and deformation performance of cable-braced grid shell with different section forms of steel tube, as section of cable, prestress of cable and span-to-height ratio vary. Economic and reasonable section form of steel tube is proposed as a reference for the practical engineering design.

Introduction

At the end of the 20th century, Germany engineer JorgSchlaichproposed cable-braced grid shell whichadopted quadrilateral meshand diagonally arranged prestressed cable [1], and the stability of the structure wasenhanced via increasing in-plane stiffness,as shown in Fig.1.Cable-braced grid shell with quadrilateral meshis convenient for the glass roof to process and install. Moreover, it has good lightpermeability, and it is lightweight and easy to choose section forms and construction.However, studies on cable-braced grid shell are still in its infancy.

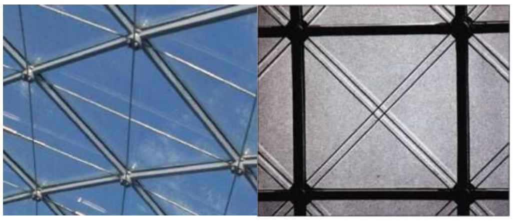

Fig. 1 The fundamental grid element of cable-braced grid shell

Withcable being used as strutsin lightweight grid shell, numerous relevant studies have beenperformed, for instance,Th.Bulendaanalyzed the effect of height-to-span ratio on the stability of elliptic paraboloid and cylinder cable-braced structure[2]. LiXin investigated the effect of load distribution, prestress and cable section on the load-bearing capacity of an elliptical paraboloid gridshell[3].JianguoCai investigated the buckling capacity of a hybrid grid shell[4].Zhang Zhiying analyzednumerous effects on the stability of circular steel tube cable-braced grid shell[5].

For the same cross section of steel tube, the variation law as for the effect of section form of steel tube on the stiffness and stability of cable-braced grid shell is proposed via the nonlinear finite element (FE) method in this paper, which provided an economic and reasonable section form of steel tube as a reference for the practical engineering design.

Analytical model

The effect of section form on the stiffness and load-bearing capacity of cable-braced grid shell was studied via FE software ANSYS. Four types of cross-sections are adopted, as Fig. 1 shows. The cable-braced grid shell with bi-directional grid is used as the research object, whose projection of the bottom is a square with sides of length 50m.The effect of section form on the stability and deformation of cable-braced grid shell with various cross sections, prestressof cable and height-to-span ratiois studied.

Table 1 Section forms of steel tube

	Circular	Vertical rectangular	Square	Horizontal rectangular
Dimension (mm)	Φ140×5.93 （Φ140×6）	80×140×6	110×110×6	140×80×6
Cross section (mm^2)	2496	2496	2496	2496
Icon	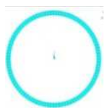		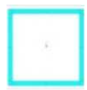	

The length of each steel tube is 1.43m, and Chinese Q345 steel is adopted.The yield stressof prestressed cableis 1500MPa. The joints are rigid and all nodes at the perimeter are fixed. Basic load on the structurecomprises dead load and live load. Dead load contains deadweight of structure and the self-weight of glass roof, whose standard value is 0.512kN/m^2; and standard value of live loadis 0.5 kN/m^2. The model is established by surfacetranslation method, as Fig. 2shows.

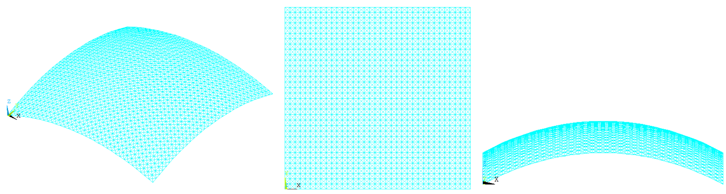

(a) Three-dimension graph(b)planar graph(c) elevation graph

Fig. 2 Finite element model diagram of cable-braced grid shell

In the FE analysis, BEAM188 element and LINK180 element are used to simulate steel tubes and cable, respectively. Both materialand geometric nonlinearity aretaken into account. Materialsare assumed to be ideal elastic-plastic. The effect of initial imperfection is considered. Its distribution is the same as the first buckling mode and maximum valueadopts Span/300.

The effect of section form on stability and deformation of grid shell

The variation of cross section of cable. Cable is one of the essential components of cable-braced grid shell. To investigate the variation law of stability and deformation performance of cable-braced grid shell with different section forms of steel tubeas section of cable vary, previous four section forms of steel tube are adopted and height-to-span ratio adopts 0.2.Prestress in the cable is 150MPa.Load factor, measured by themagnification of basic load, is used to express load-bearing capacity.

It is shown in Fig. 3(a) that as the cross section increases, the cable-braced grid shells with circular and vertical rectangular steel tube have a similar load-bearing capacity,which increases slowly in early prophase and increases greatlywhile cross section of cable exceeds a certain value. The stability of structurewith square steel tube varies in the same way, but it has a lower load-bearing capacity.The stability of cable-braced grid shell with horizontal steel tube is the lowest.In Fig. 3(b), the deformation of cable-braced grid shell with circular and square steel tube is relatively large. As for cable-braced grid shell with vertical rectangular steel tube, its deformationis relatively small, and for cable-braced grid shell with horizontal rectangular steel tube, the deformation varies as the diameter of cable increases, which might result from the change of instability of modes.

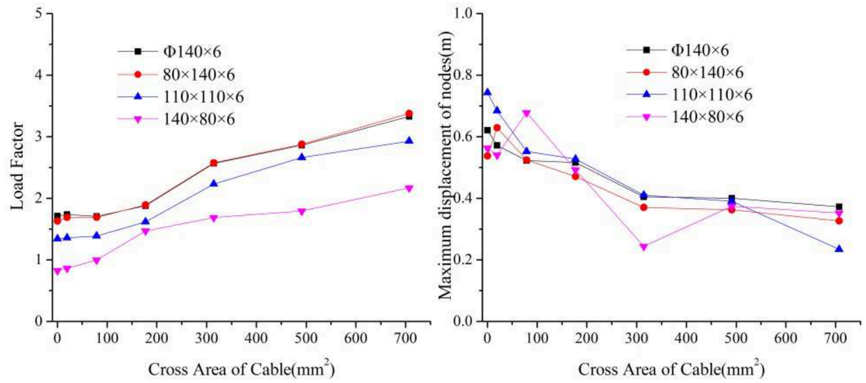

(a) stability(b) deformation performance

Fig. 3Stability and deformation performanceoffour kinds of cable-braced grid shells

The variation of prestress of cable. As anothersignificant influential factor,prestress affects stability of cable-braced grid shell as well. To investigate the variation law of stability and deformation performance of cable-braced grid shell with different section forms of steel tubeas prestress of cable vary, previous section forms of steel tube are adopted and height-to-span ratio adopts 0.2.Cross section of the cable is 314mm^2.

As Fig. 4(a) shows,that when the cross section of cable is small, the load-bearing capacity of cable-braced grid shell increases greatly as the prestress increases; while prestress of cable exceeds a certain value, the load-bearing capacity of cable-braced grid shellswith different section forms hardly vary. According to the load-bearing capacity, a descending order is given as follows: cable-braced grid shell with circular, vertical rectangular, square and horizontal rectangularsteel tube. Fig.4(b) indicates that the deformation of cable-braced grid shell with circular and square steel tube issimilar. The deformation of cable-braced grid shell with circular and square steel tube is large, and deformation ofvertical rectangular formis relatively small.As the prestress of cable increases, deformation of cable-braced grid shell with horizontal rectangular steel tube varies unstably due tothe change of instability of modes.

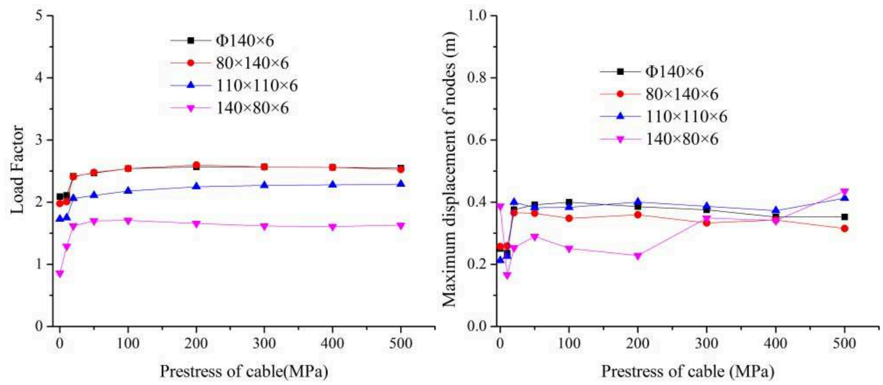

(a) stability(b) deformation performance

Fig. 4Stabilityand deformation performance of four kinds of cable-braced grid shells

The variation of height-to-span ratio. Height-to-span ratio affects the stability of grid shell greatly. To investigate the variation law of stability and deformation performance of cable-braced grid shell with different section forms of steel tubeas height-to-span ratio vary, previous section forms of steel tube are adopted.Cross section of the cable is 314mm^2 andits prestressis 150MPa.

It is illustrated in Fig.5(a) that, with height-to-span increasing, the stability of each structure increases, which elucidatesincreasing the height-to-span has benefits to improve stability. The cable-braced grid shell with circular and vertical rectangular tube is much higher, while the cable-braced grid shell with horizontal rectangular tube is the lowest. Fig. 5(b) shows thatthe deformation of cable-braced grid shell with circular, vertical rectangular and square steel tube is obvious. Moreover, height-to-span ratio has a limit effect on the deformation of cable-braced grid shell with horizontal rectangular steel tube, and its deformation is small. While the height-to-span ratio exceeds a certain value, deformationof each cable-braced grid shell becomes stable and close, which suggests that when the height-to-span ratio is large,the section form has a limit effect.

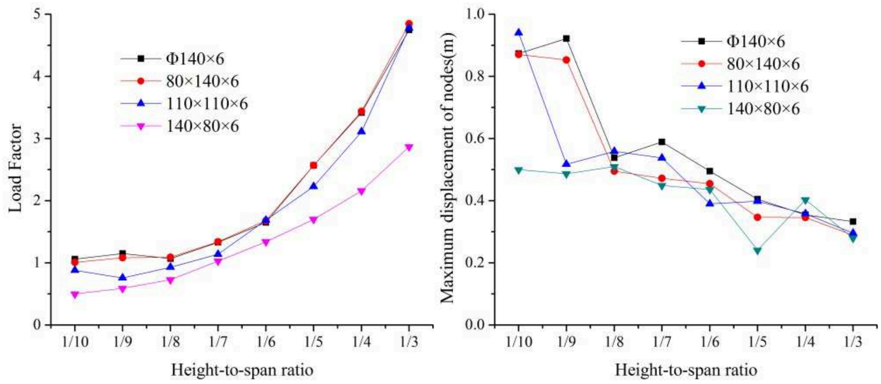

(a) stability(b) deformation performance

Fig. 5Stability and deformation performanceof four kinds of cable-braced grid shells

Summary

It isconcluded that the load-bearing capacity ofcable-braced grid shell with circular and vertical rectangular steel tube is higher than that of cable-braced grid shell with square and horizontal rectangular steel tube. The deformation of cable-braced grid shell with circular and square steel tube is larger in each condition. The deformation of cable-braced grid shell with horizontal rectangular steel tube becomes unstable for the buckling modes vary. To summarize, cable-braced grid shell with circular steel tube andvertical rectangular steel tube is relatively economic and reasonable.

Acknowledgements

This work was financially supported by theNational Natural Science Foundation of China (51478387).

Reference

[1]Annette Bogle. Light Structures [M]. China Architecture & Building Press, 2004.

[2]Bulenda. Th, Knippers. J. Stability of grid shells[J].Computers and Structures,2001,79: 1161-74.

[3]LiXin,WuYue. Grid shell-a new type of space structures[J]. Space structures, 2007,2:17-21 (In Chinese)

[4]JianguoCai, LemingGu, YixiangXu et al. Nonlinear stability analysis of hybrid grid shells [J]. International Journal of Structural Stability and Dynamics, 2013(13):1-16.

[5] Zhang Zhiying, Zhao Xun, Wei Hongyang. Stability analysis of circular steel tube cable-braced grid shells with initial imperfection [J]. Applied Mechanics and Materials, 2014: 695-699.

Applied Mechanics and Materials Vols. 744-746 (2015) pp 29-32
© (2015) Trans Tech Publications, Switzerland
doi:10.4028/www.scientific.net/AMM.744-746.29

Corrosion ProtectionTechnology of Steel Structure in Marine Environment

Xin Gao[1,2,a], LizhiGuo[3,b] JianboXiong[1,2,c]

[1]CCCC Fourth Harbor Engineering Institute Co.,Ltd. Guangzhou, Guangdong Province, China

[2]Key Laboratory of Harbor & Marine Structure Durability Technology Ministry of Communications, CCCC fourth Harbor Engineering Institute Co., Ltd., Guangzhou, Guangdong, China

[3]The Second Engineering Company of CCCC Fourth Harbor Engineer Co.,Ltd. Guangzhou, Guangdong Province, China

[a]myth2054@163.com,[b]glizhi@gzpcc.com,[c]xjianbo@gzpcc.com

Keywords: steel structure, anti-corrosion

Abstract: Harbor projects have to face harsh marine environment, and the corrosion damageof steel structures is rather serious. It is an insurance for structural safety and animportant measure of durable that strengthening of corrosion control, selecting theappropriate anti-corrosion technology, reasonable design, scientific construction andappropriate maintenance management, and it has an important economic and strategicsignificance.

Introduction

Seaport is a major and logistics infrastructure fortransport export trade.as China's sustained and rapid economic development, harbor projectsis presenting to large scale, complicated construction technology, deepwater and offshore features. steel structure with its excellent physical, mechanical, is favored in the environmentof large waves, complex geological conditions, urgent need of specialized portsand deepwater berths, which other materials cannot match these advantages.

But steel in the marine environment, such as not to take protective measures ,is vulnerable to be attacked by electrochemical corrosion and other damage,which makes steel thickness decrease, physical performance degradation and local stress concentration and directly affect use function andlife of engineering structures, even accidents[1]. Therefore, it's urgent and necessaryto enhance the control of steel anti-corrosion.In order to ensure the structural safety and durability of the harbor project,importantmeasures such as appropriate anti-corrosion technology, reasonable design, construction science and moderate maintenance can be taken, which has economic and strategic significance.

Protection methods of steel structure in marine environment

The corrosion rate of steel piles in seawater mainly depends on thecathodic process, and is influenced by the content of oxygen in unit time, which reach and spread to the steel surface. Actualamount of oxygen supply is closely related to environmental factors such as seawater velocity, salinity,temperature and sea creatures.The corrosion rate ofsteel structure varieswith the region, especially the splash zone with maximum corrosion rate, because of the range of alternating wet and frequent temperature fluctuations, coupled with seawater bubbles and floating debris impact damage to the surface and a protective layer, whichcreaterich supply of oxygen in the form of film near the steel surface, and can easily cause significant corrosion.In order to resist the corrosion, it's feasible to startfrom the mechanism of electrochemical corrosion.Firstly it's effective to forma surface barrier to reduce the oxygen concentration in the surface of steel surfaces, such as corrosion-resistant steel, protective coatings or surface coating,on the other hand measures can be taken to change steel corrosion characteristics of half-cell reaction and keep the steel piles from the electrochemical reaction,such as sacrificial anodes or impressed current cathodic protection method.

2.1 Corrosion Resistant Steel of Low-alloy[2] [3]

After alloying the steel components, Corrosion resistant steel of low-alloycan make rust dense and inhibit oxygen's penetration. To some extent, it has a lower corrosion rate.specific effectsof adding the element vary with the exposed environment, combine of the added elementsand the addition.Elements ofphosphorus, copper, nickel is generally added to the splash zone ,and other elements such asSi, Cr, Al, NI and Mois added in seawater zone to reduce seawater pitting of steel piles.Appropriate amount of Zn, Ti, Ni and other elements can be further improved corrosion resistance of steel.Currently, Corrosion resistant steelcan be divided according to the chemical composition of copper-phosphorus, chromium-copper and chromium-aluminum three major series. Meanwhile, In order to improve weldabilityand workability ofcorrosion resistant steel.Many countries have developed its own characteristics products such as copper-chromium-phosphorus, copper-chromium-aluminum-phosphorus, copper-chromium- molybdenum seawater corrosion resistant steel.

2.2 Corrosion Allowance Method

Corrosion allowance method refers to keeping appropriate corrosion allowance after taking the appropriate measures of steel anti-corrosion.Normally,it's determined according to the uniform corrosion rates and design life. The concept and view have been accepted by the designer and owners. Steel designin waterway engineering will generally refer to the relevant specifications and give some numerical of corrosion allowance. But corrosion allowance makes sense only to prevent even corrosion damage.For stress corrosion,crevice corrosion and hydrogen embrittlementand other non-uniform corrosion, it's not effective to take corrosion allowance ways to prevent steel corrosion, while select of corrosion materials or properly protection against corrosion is more important.

2.3 Coating Protection Method

Coatingprotection method is the most commonlyusedduring steel structurecorrosion.Steel structure corrosion in seawaterisa process of response depolarization of oxygen.Coating on the surface of steel structure can hinder the transmission of corrosive medium, thereby inhibiting corrosionreaction.

2.3.1 Heavy-duty Coatings

Under normal circumstances, steel corrosion coating system consists ofa composite component with a primer, intermediate coat and topcoat layer. Primer can be used anti-rust primer or metal thermal spraying. Anti-rust primer coating system is more common and can be divided into epoxy, urethane, glass flake type, silicone-based and fluorocarbon coatingwith dry film thickness of 200μm or 300μm or more generally, thickness up to 500μm~1000μm, even 2000μm.Thicker film coating cancreate a long-term life of steel andguarantee to extend the life of steel structure up to 10 years or 15 years.

2.3.2Corrosion Protection Technology of Metallic Thermo-spray

Technology of metallic thermo-spraycan form a layer of a metal adhesion layerin way of the meltand atomization of metal with a heat source. Metallic thermo-spray protection system includes a metal coating layer and paint sealant, while complex protection system also includes paint. Metallic thermo-spray protection system are generally used in waterway engineering such as aluminum-zinc-magnesium alloy or zinc alloy.The select ofmetallic thermo-spray materials, coating systems and coating thickness should be determined by the environment, maintenance, and use requirements. Thermal-spray galvanizing requiresa higher conditionof construction as well as a higher initial investment. Its protection life time should be longer than zinc-rich primerand other ordinary steel coating systems, and it is recommended and adopted when the life expectancy is more than 20 years.

2.4 Cathodic Protection Method

Cathodic protection is to make protected metal gaina protection current and cathodicpolarize. When its potential of cathodic polarization reaches a certain value, the metal corrosion nearly stopped. Cathodic protection can effectively prevent general and localized corrosion, commonly used in the underwater zone and mud area. Examples such as the southern port (Zhanjiang Port, Nansha Port, Huizhou Port,, Zhuhai Port etc.) has adopted anti-corrosion design.

2.4.1 Sacrificial Anode Method

Sacrificial anodemethodrefers to a connection between the protected metal and other metal or alloy with a more negative electrode potential.It’s effective toprotect metalthrough the dissolution and consumption of self-sacrificial anode. Its advantages is no power supply, simple construction and maintenancemanagement suitable forharbor engineering steel in seawater or brackish water ,or zone below the average level with resistivity less than 500Ω • m.While its drawback is short-lived, non-adjustable .Output current depends on the anode and environment. Sacrificial anodes is more economical in small quantities or scattered component unit.Waterwayengineering generally use aluminum or zinc alloy sacrificial anodes.

2.4.2 Impressed Current CathodicProtection[4]

Impressed current cathodic protection applys by an external DC power supply to the steel cathode current.it can make the potential of the steel negatively shift and get intocathodic protection zone. Impressed current cathodic protection systems typically includes an auxiliary anode, reference electrode, a DC power supply, control systems and cable,suitable for steel structure with different orhigher change ofresistivity .it’s of more economical when large projects, relatively concentrated component distribution.Meanwhile,itspost-maintenance requirements are relatively high.

2.5Coating Layer Technology[5]

Coating layer technology is a surface treatmentmethod combined with corrosion inhibitor and oxygen sealingtechnology withlow requirements,which can be used in wet or underwater.It can provide good protective layer thickness, mechanical properties and anti-corrosion performance according to the demand,and can be used as an effective protective measures for new steelstructure insplash zone , as well as an important choice for repairmen of old steelstructure.

Steel Protection Technology Research Prospects

Steel corrosion protection has been rapid developedin waterway engineering. But anti-corrosion measures for environmental friendly requirements have also been strengthened. Therefore, it need to continue to study in the following aspects:(1)environmental friendly coatings such as high-performance water-based coatings, solvent-free coatings, powder coatings;(2)inexpensive coating materials, lower cost of organic orinorganiccoating layer;(3)better performance of the anode material with longcathodic protection of life toreduce raw material and energy consumption.

Conclusions

During the construction of steel structure in waterway engineering,Design should consider the designed service life requirementand structure characteristics,andaccuratelychoose one or a combination of corrosion protection measure according to actual environmentsituation; meanwhile good quality control measure is necessary.

References

[1]Ji-Xun,Wu: Metal corrosion protection technology: Metallurgical Industry Press, 1998:16-28. In Chinese.

[2] Matsushima Iwa. Low alloy steel-development,development and research [M].BeiJing: Metallurgical Industry Press,2004.14. In Japanese

[3] Choi Yoon-Seok,Shim Jae-Joo,Kim Jung-Gu Corrosion behavior of low alloy steels containing Cr,Co and W in synthetic potable water[J].Materials Science & Engineer,2004,(01):148-156.

[4] NACE Rp0388-2001:Item No.21040,Impressed Current Cathodic Protection of Internal Submerged Surfaces of Carbon Steel Water Storage Tanks

[5]Jianbo Xiong,Huazhang,Zhang: Design and Application of Coating Proctection System in Maintenance of Steel Tubular for Piled Wharfs[J]:China Harbour Engineering,2011,(06):37-39.

Applied Mechanics and Materials Vols. 744-746 (2015) pp 33-37

doi:10.4028/www.scientific.net/AMM.744-746.33

Damage Identification of Space Truss Structure Based on Strain Modal and wavelet Transform

Weiran Liu[1,a],Qilian Li[1,b] and Hongliang Yue[1,c]

[1] School of Civil Engineering, Hebei University of Science and Technology, Shijiazhuang Hebei 050018,China

[a]26547806@qq.com, [b]lql6599@163.com,[c]yuehongliang2000@163.com

Keywords: space truss structure; damage identification; wavelet transform; strain modal

Abstract. Based on the characteristics of space truss structures, the concept of modal strain energy is introduced and square difference in elemental modal strain is presented. Through the square difference in elemental modal strain and wavelet transform, this paper presents a method for space truss structure damage recognition. The structural damage index is presented with the change of wavelet coefficients. Numerical simulation results show that: this method is effective to locate the single, multiple damages and light, severe damage with the first mode information. The preliminary tries for damage extent identification were made by the wavelet coefficients.

Introduction

Structural damage detection is an active research domain in current structure engineering. Many of researchers have made much effort on this subject and proposed many analysis methods. Shi and Low point out the methods concerned with the structural damage detection based on modal strain energy[1,2].Hou et al. make use the method of wavelet analysis to detect damage[3]. Yongmei Li points out the methods of the wavelet analysis of modal strain energy, numerical experiments indicate that the method is efficient for damage location to reticulated shell structures,with the changes of the elemental modal strain for damage locations of truss structures as the new dynamic fingerprints[4]. Limei Zhang points out damage detection method based on curvature mode difference and wavelet transform for the grid damage detection [5].

Theory of Damage Identification Based on Strain Modal

Modal strain energy can reflect local vary character of structures and it can be obtained by stiffness matrices and vibration. Modal strain energy is feasible to identify the structure damage localization and damage severity，low mode can gain well damage information. Element modal strain energy of the truss can be expressed by the following eq(1):

$$MSE_{ij} = \frac{1}{2} E_j A_j l_j \varepsilon_{ij}^2 \qquad MSE_{ij}^d = \frac{1}{2} E_j A_j l_j \varepsilon_{ij}^{d2} \tag{1}$$

Where MSE_{ij} and MSE_{ij}^d are represented as undamaged and damaged j element modal strain energy of mode i, ε_{ij} and ε_{ij}^d are represented as undamaged and damaged j element mode strain i, A_j is the j element cross-sectional area, l_j its length, and E_j its modulus of elasticity Based on the theory of modal strain energy, the method of damage identification with modal index is element modal strain energy change as follows eq(2)

$$MSEC_{ij} = MSEC_{ij}^d - MSEC_{ij} = \frac{1}{2} E_j A_j l_j (\varepsilon_{ij}^{d2} - \varepsilon_{ij}^2) \tag{2}$$

In this paper, propose a damage detection index based on the square difference in elemental modal strain can be written as eq(3):

$$\Delta = \varepsilon_{ij}^{d2} - \varepsilon_{ij}^2 \quad (k = 1, 2, \cdots, N) \tag{3}$$

The Theory of the wavelet analysis

Wavelets function and transformation are becoming increasingly important for scientists and engineers in damage detection field. Wavelet transform is a very useful tool of signal processing, the one called mother wavelet function is made the displacement *b*, and than do the inner product under different scales *a* and the signal to be analyzed.Wavelet coefficients can be got from convolution of *a* scale mother wavelet function and the analysis of signal,the wavelet function can be Written as eq(4), wavelet coefficients transform is expressed as eq(5):

$$\psi_{a,b}(\mathrm{x}) = \frac{1}{\sqrt{|a|}}\psi(\frac{x-b}{a}) \tag{4}$$

$$W_{a,b}(f(x),\psi) = \frac{1}{\sqrt{a}}\int_R f(x)\psi^*(\frac{x-b}{a})dx \tag{5}$$

Where is the basic wavelet function that satisfies certain very general conditions,*a* is a scale factor, *b* is the translation factor, $f(x)$ is the original structural damage signal. Structural damage $f(x)$ can be identified by wavelet transform coefficients as eq(6):

$$f(x) = \varepsilon_{ij}^{d2} - \varepsilon_{ij}^{2} \tag{6}$$

One-dimensional continuous wavelet function is defined as that we choose L2(R) Space function $f(x)$ which Carried out under wavelet-basis arbitrary,and call this kind launches as continue Wavelet transform of $f(x)$.

Structural model

To demonstrate the advantages of the proposed method, the finite element analysis model of the space truss structure is established for damage identification of single and multiple simulated damage conditions.The structural model is shown in Figure1.the structure has 61 nodes and 200 elements, the space truss structure material properties are as follows: modulus of elasticity E=2.06e11Pa,steel density 7850kg/m^3,link sectional size A=456mm^2.The length of the lower chords and upper chords is 3m, the height of space truss structure is 2.2m.It is assumed that mass of this structure keeps unchange when structure damage occurs.Various degrees of each damage were simulated by the reduce its elasticity in several parts of the modal.In this paper ,six damage conditions are shown as table 1.

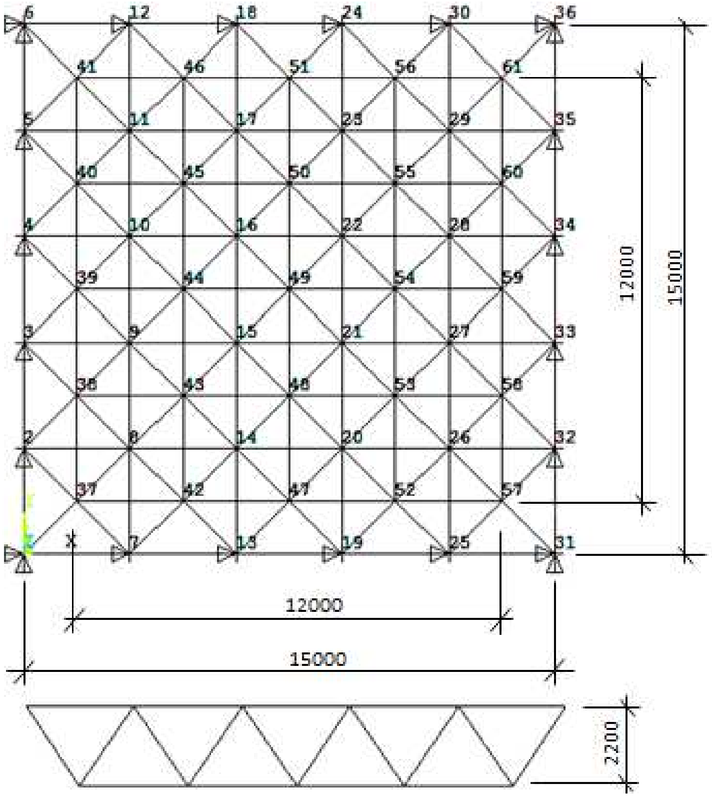

Fig.1 Space truss structure model

Tab.1 Element damage cases

damage cases	damage element	damage degree
1	top chords 12	10%
2	top chords 12	50%
3	web member 51, web member67	30%,30%
4	Lower chords44 , web member 115	50%, 50%
5	Lower chords 88,top chords 14, Lower chords 53	30%,30%,30%
6	Lower chords 9,top chords 17,web member 67and115	70%,70%,70%

Single damage cases

Wavelet transform coefficients of different degree damage under the single damage cases are shown in figure2,from the figure2, the method can very accurately identify space truss structural damage location (12 element) and can identify degree extent preliminary by the wavelet coefficients.When the damage degree increases, the wavelet coefficients aslo follow to increase.

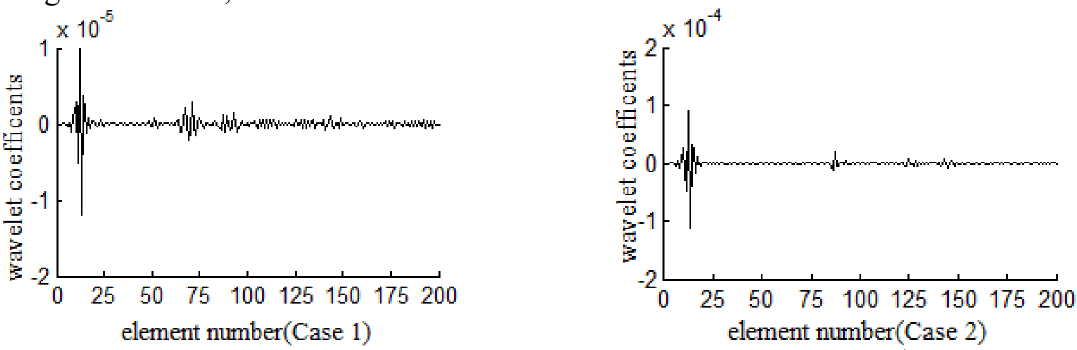

Fig.2 Wavelet transform coefficients of damaged modal (1st mode)

Multiple damage cases

The identification of multiple damaged locations in structures is also studied, The results are shown in figure3 and figure4. The results show that the peak values of the damage indices are observed at the exact damage locations pre-determined from the numerical model.It can be shown figure3 that the

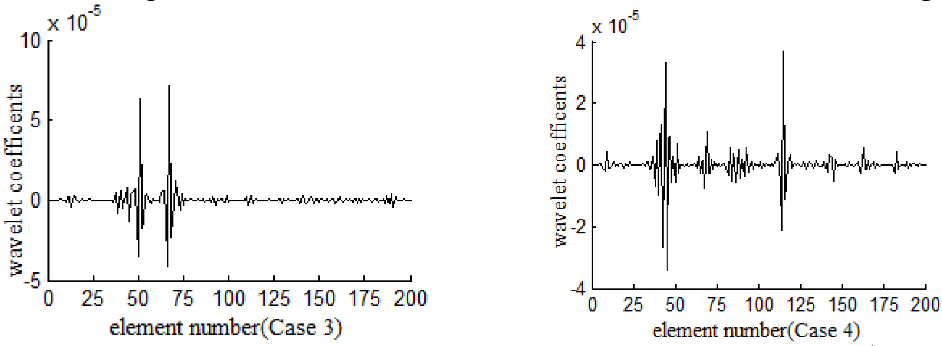

Fig.3Wavelet transform coefficents of double damaged modal (1st mode)

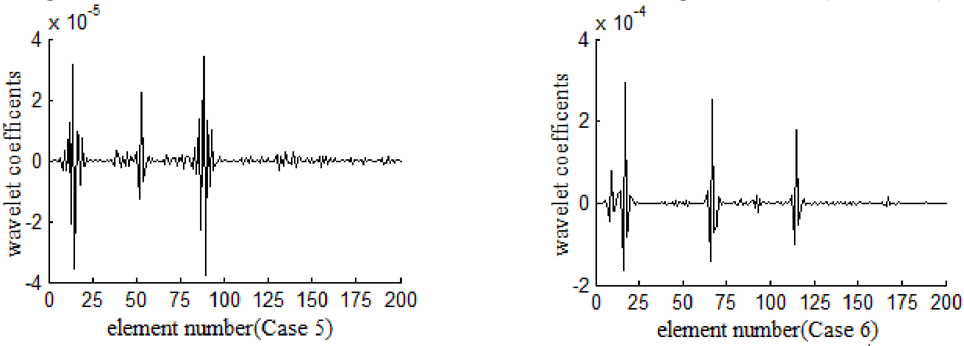

Fig.4Wavelet transform coefficents of multiple damged modal (1st mode)

double damage locations can be determined by wavelet transformation. It also can be shown figure4 that the three damage locations (case 5)and four damage locations (case 6)can be determined by wavelet coefficients.

The estimation of damage degree based on wavelet coefficients

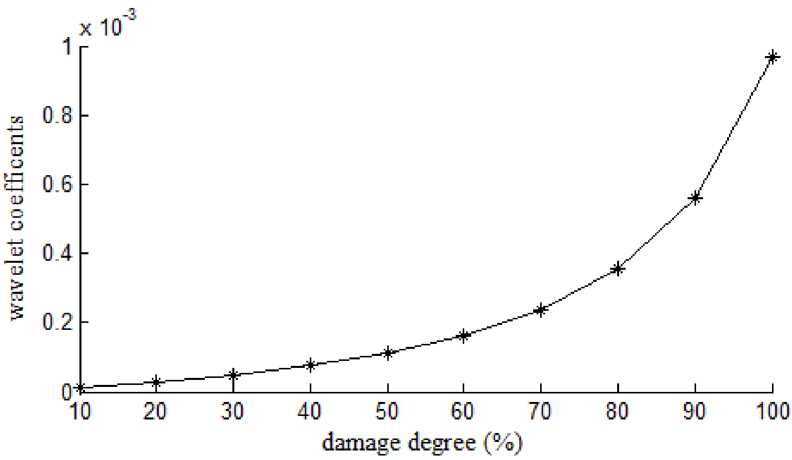

Fig.5 Wavelet coefficients and different damage levels(12 element)

With the same damage location(12 element), the relationship between wavelet coefficients and degree of damage is discussed. To take the element 12 of space truss structure for an example, wavelet coefficients of the index varied with the damage degree are shown in Figure5, wavelet coefficients increases with the increasing of the damage degree of the element 12. On the basis of this rule, the damage degree of space truss structure can be identified using the wavelet coefficients.

Conclusion

In this paper, the study results indicate that it is a feasible way to identify the damage based on the change of the square difference in elemental modal strain with the help of wavelet transform. By numerical simulation analysis of the localization result, the results show that the wavelet coefficients is very effective with the first mode of space truss structure with single or multiple damage position. This index had high sensitivity to space truss damage with the first modal information. Therefore, the research had important practical for the early diagnosis. The damage degree of the structure can be determined evaluated by the wavelet coefficents.

Acknowledgements

Project Funding: Hebei Science and Technology Research Young College Fund(2011229);
Project(XL201033) supported by University Fund of Hebei University of Science and Technology.

References

[1] Shi Z Y, Law S S, Zhang L M. Structural damage localization from modal strain energy change[J]. Journal of Sound and Vibration, 1998, 218(5): 825-844.

[2] Shi Z Y, Law S S, Zhang L M. Improved damage quantification from elemental modal strain energy change [J]. Journal of Engineering Mechanics, 2002, 128(5): 521-529.

[3] Hou Z, Noori M, Amand R S. Wavelet-based approach for structural damage detection [J]. Journal of Engineering Mechanics, 2000, 126(7): 677-683.

[4] Yong mei Li, Bing Zhou, Wei Wei Zhou.Study on location to reticulated shell structures based on wavelet analysis of modal strain energy[J].Spatial Structures,2012,18(4):24-29.In Chinese.

[5] Meng Fan, Li mei Zhang. Grid damage detection based on curvature mode difference and wavelet transform[J].Journal of Hebei University of Science andTechnology,2014,35(4):384-391.in Chinese.

Applied Mechanics and Materials Vols. 744-746 (2015) pp 38-45

doi:10.4028/www.scientific.net/AMM.744-746.38

Degradation mechanism of reinforced concrete beam subjected to fatigue loads and seawater erosion

Zijian LIU [1, 2,a] Bo DIAO [1 ,b] Xiaoning ZHENG[1, 2,c]

[1] School of Transportation Science and Engineering, Beihang University, Beijing 100191, China;
[2]State Laboratory of Subtropical Building Science, South China University of Technology, Guangzhou 510640, China

[a]sunsword@163.com, [b]diaobo@buaa.edu.cn, [c]zxn@buaa.edu.cn

Keywords: concrete durability, fatigue, seawater corrosion.

Abstract. The durability of coastal reinforced concrete bridge structures will be deteriorated during service due to fatigue loads and Chloride erosion. Through the microscopic tests of reinforced concrete beams after fatigue and seawater corrosion, 10 reinforced concrete beams divided into 5 groups subjected to different fatigue loads were investigated under the alternative action of seawater corrosion, where the deterioration of concrete was degraded. From the experiment, it can be concluded that there was significant self-healing phenomenon on the cracked beams by fatigue loading; And there was regular and clear microcracks in the beams when the maximum fatigue load between 0.16~0.24Pu; the cracks of the beams became obvious， micro cracks increased and crystals can be significantly seen in cracks and low lying location when the maximum fatigue load exceeds 0.24Pu.

Introduction

A large amount of cracks appeared in costal reinforced concrete bridges due to fatigue loads caused vehicles. Also, the deterioration of the structures' circumstance affects the durability. Some bridges in coastal area of Shandong Province suffer severe cracking and steel corrosion [1] after about 10 years' service, which directly affect the normal use and durability of the structure.

Recent research has focused on concrete durability to assure reinforced structures' life and safety. And the degradation study has turned to microscopic from mechanical properties. Ringota E, Bascou A [2] introduced the methods of observation and analysis of microscopic cracks in the concrete and defined the parameters of the two-dimensional and three-dimensional cracks. Zuquan Jin[3] studied the corrosion mechanism of chloride, sulfate and their mixed solution to concrete and analyzed the crystal composition of the corrosion product. Rundong Gao [4] studied the degradation of the mechanical properties of concrete after sulfate corrosion in different environments, and discussed deterioration mechanism based on the internal micro-crystals. Bo Diao [5~ 8] conducted concrete structures freeze-thaw and corrosion test, using experimental methods such as scanning electron microscopy to observe changes in the microstructure, analyze concrete hydration products and crystals, and thus analyze the degradation mechanism of freeze-thaw cycles in the saltwater in depth.

Scholars who study the microscopic corrosion mechanism of concrete materials under chloride and sulfate corrosion have achieved a lot. However, few have studied the microscopic corrosion mechanism of concrete with fatigue cracks under chloride corrosion. Here in the paper, dry-wet in seawater cycle experimental study is conducted on RC beams under different fatigue loads. Deterioration mechanism of concrete is studied through observation of microscopic cracks and SEM analysis of concrete materials.

Specimen preparation and test methods

Specimen preparation

Specific ratio of concrete materials in reinforced concrete beam specimens is shown in Table 1. PC.32.5R cement is used as concrete mix; coarse aggregate is gravel with diameter of 5 ~ 8mm; fine aggregate is sand with fineness modulus of 2.6, moisture content 2%; II grade fly ash is used as admixtures; Admixtures are TK-PC02-type super plasticizer.

Table1 Concrete Mix

Water-cement ratio	Water	Cement	Sand	Stone	Fly-ash	Concrete
0.4	3kg	7.5kg	10kg	18.5kg	0.6kg	40kg

The detailed dimensions and reinforcement layout of test beams are shown in Figure 1. Longitudinal reinforcement is 8mm HPB235 steel bar, while stirrups 6mm HPB235 steel bar. Measured yield strength of steel bar is 439.17Mpa, ultimate strength 542.19MPa and reinforcement rate 0.67%.

11 reinforced concrete beams were prepared, in which one is tested under static load as reference beam. And the tested ultimate load of this reference beam (Pu) is 57.5KN. The other 10 beams are divided into 5 groups for fatigue load and seawater corrosion tests, as shown in Table 2.

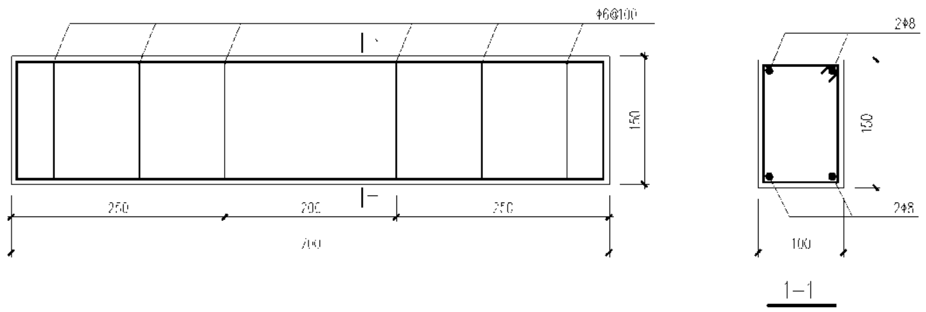

Figure 1 Specimen Reinforcement Detailing

Table 2 Beam specimens grouping

Number	Fatigue-stress ratio	Fatigue load	Fatigue cycles	Seawater dry-wet cycles
L1,L2	0	0	0	100
L3,L4	0.16	0.16Pu--0.08Pu	2×105	100
L5,L6	0.24	0.24Pu--0.08Pu	2×105	100
L7,L8	0.32	0.32Pu--0.08Pu	2×105	100
L9,L10	0.40	0.40Pu--0.08Pu	2×105	100

Test methods

The specimens were removed from conservation in age of about three months. Fatigue tests are conducted on the MTS fatigue testing machine, using four-point bending fatigue testing method, with loading frequency 4 Hz. After fatigue tests artificial seawater immersion dry-wet cycles test were conducted. Artificial seawater corrosion solution is a mixed of 3% sodium chloride (NaCl) and 0.34% magnesium sulfate ($MgSO_4$). There are 100 dry-wet cycles, and the specimens were in seawater for 12h and in air for 12h in each cycle.

Results and analysis

Experimental phenomena of fatigue bending test

None visible cracks appear on beam L3, L4 while loaded. There are visible cracks appeared on L5, L6 after 10000 times cycle loading, which grow, widen and extend by time. Visible cracks appeared on L7 ~ L10 as soon as the cycle loading starts, which also grow, widen and extend with time. A little of concrete mortar flakes on loading point of L9, L10. Specific crack width under peak (valley) loads is shown in Table 3.

Table3 Crack width under fatigue loads

Series number	Crack width(mm) 50000 times	Crack width(mm) 100000 times	Crack width(mm) 150000 times	Crack width(mm) 200000 times
L5	0.17(0.08)	0.19(0.10)	0.19(0.10)	0.20(0.13)
L6	0.15(0.07)	0.18(0.09)	0.20(0.11)	0.20(0.14)
L7	0.20(0.13)	0.22(0.13)	0.23(0.15)	0.23(0.15)
L8	0.21(0.12)	0.21(0.12)	0.21(0.14)	0.24(0.14)
L9	0.27(0.15)	0.29(0.15)	0.29(0.15)	0.30(0.12)
L10	0.20(0.10)	0.21(0.10)	0.21(0.10)	0.21(0.10)

Surface morphology changes of specimen beams after fatigue loads and seawater corrosion

While the fatigue loading test is completed, dry-wet cycle test is conducted on the beams. The surface morphology changes of beams are shown in Figure 2-4. As loading and cycle times increase, more crystals appear on the surface of beams, especially in the depression areas which make the color of beam surface turn to light yellow from pale. After fatigue loading, the crack width of beams decrease. Some of the cracks cannot be observed by eyes.

With the increase of dry-wet-cycle numbers, crack healing phenomenon is increased apparently. When fatigue stress ratio is larger, the initial cracks are wider and the self-healing phenomenon is less obvious. With the same fatigue stress load, the healing phenomenon of beam with two initial cracks is obvious than that with one initial crack, indicating beams with two cracks have narrower width and shallower depth.

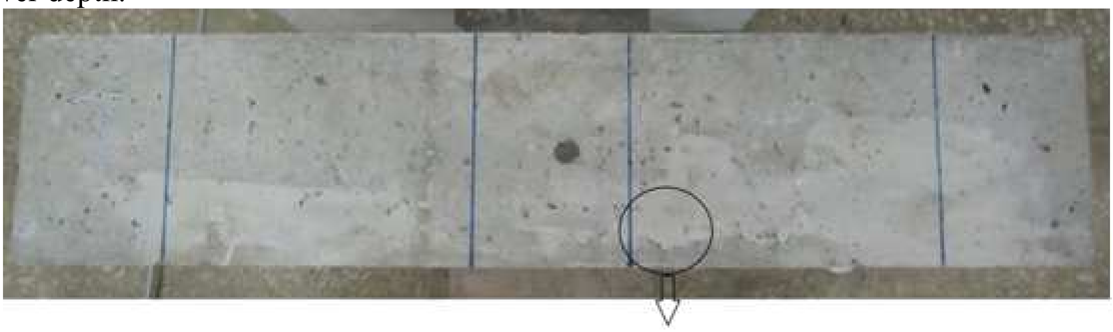

L5 Before dry-wet cycles in artificial seawater

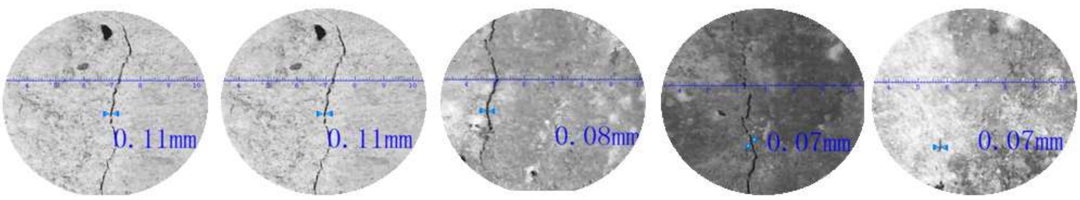

0 cycle 25 cycles 50 cycles 75 cycles 100 cycles

L5 After dry-wet cycles in artificial seawater

Figure 2.Changes of surface morphology of L5in dry-wet cycles in seawater

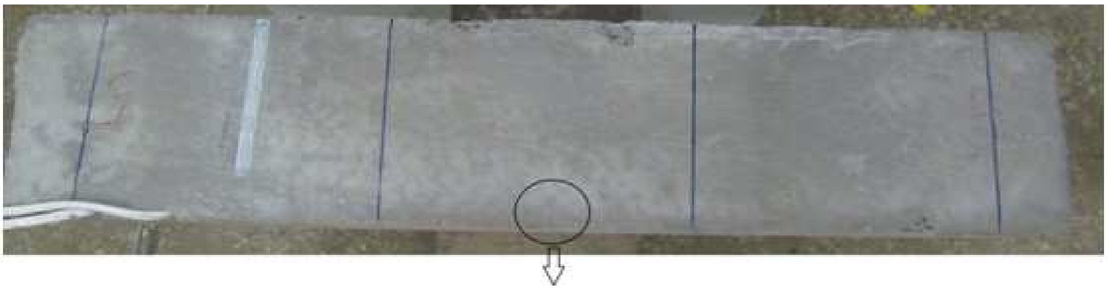

L8 Before dry-wet cycles in artificial seawater

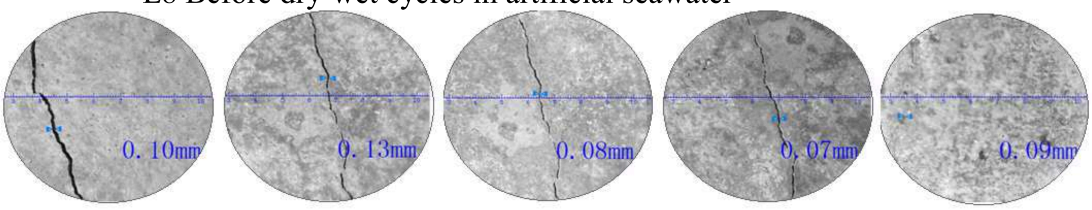

0 cycle 25 cycles 50 cycles 75 cycles 100 cycles

L8 After dry-wet cycles in artificial seawater

Figure 3. Changes of surface morphology of L8in dry-wet cycles in seawater

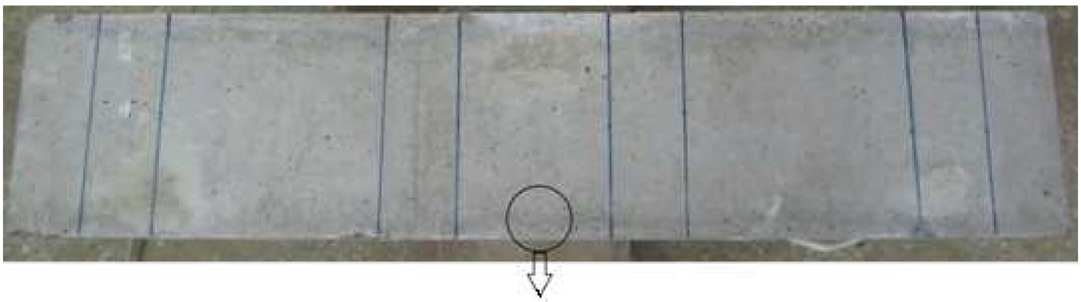

L10 Before dry-wet cycles in artificial seawater

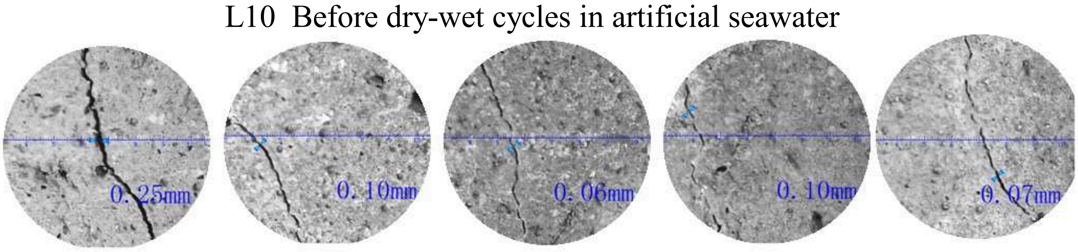

0 cycle 25 cycles 50 cycles 75 cycles 100 cycles

L10 After dry-wet cycles in artificial seawater

Figure 4. Changes of surface morphology of L10in dry-wet cycles in seawater

Microscopic changes of specimen beams after fatigue loads and seawater corrosion

After static tests of specimen beams, which are affected by fatigue loading and sea water corrosion, the cracks are broken at the pulled area of the beam cross-section. Test pieces with length of about 3~5mm long are taken from the area about 10 ~15mm far from the pulled edge. And the pieces are analyzed by SEM tests after drying.

2.3.1 Analysis of micro-morphology and micro-crack of concrete materials

Micro-cracks (1000 times) of concrete pieces are shown in Figure 5. There are regular, relatively clear micro-cracks on beams with maximum fatigue load ranged from 0.16 to 0.24Pu, which are relatively small. For beams under fatigue load greater than 0.24 Pu, micro-cracks are more obvious, wider and deeper. Crystals obviously exists in cracks and depression areas.

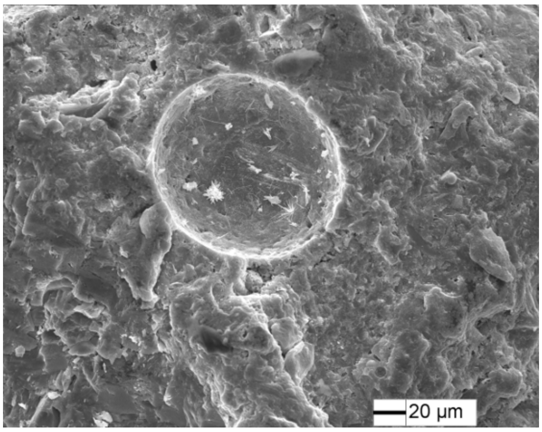

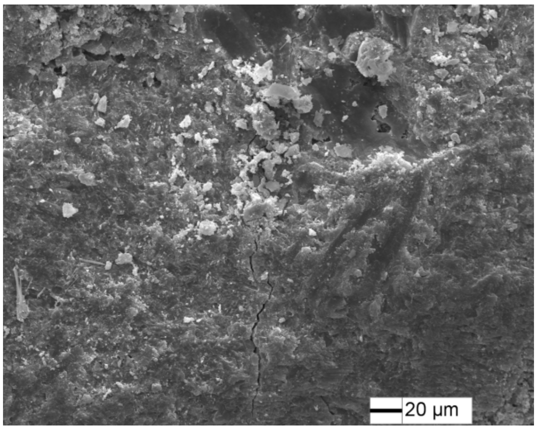

(a) Beams without fatigue load (b) Beams with 0.16Pu fatigue load

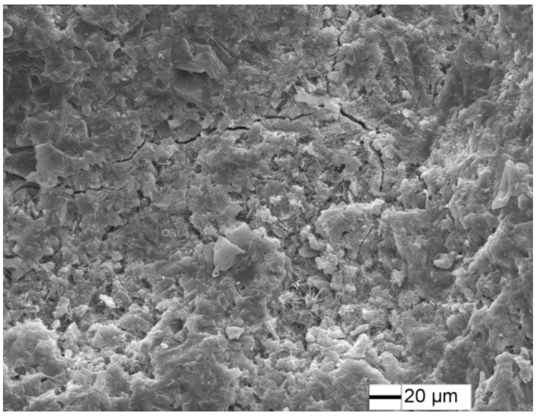

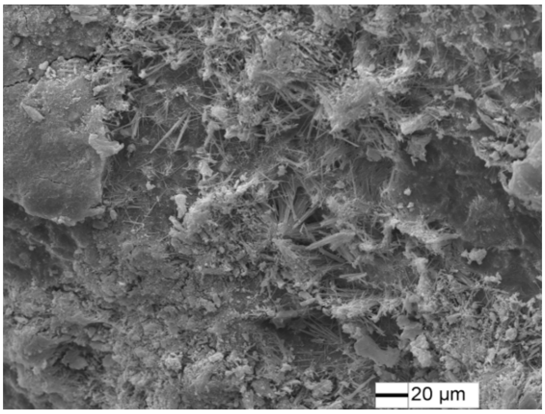

(c) Beams with 0.24Pu fatigue load (d) Beams with 0.32Pu fatigue load

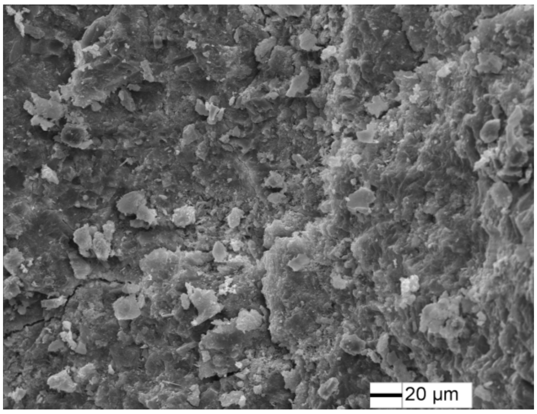

(e) Beams with 0.4Pu fatigue load

Figure 5 Micro-cracks on beams under different fatigue loading amplitude (1000times)

Crystals analysis of concrete materials

Concrete material crystals (4000 times) and the components analysis are shown in Figure 6.

After 100 times corrosion，tiny filamentous crystals can be observed on the reference beams without fatigue load. For beams with a maximum fatigue load of 0.16Pu and 0.24Pu, apparently larger number of bundles of crystals appear in cracks and depressions, which are also thicker. For beams with a maximum fatigue load of 0.32Pu, a large number of clustered crystals, which are thick like columns, appear not only in cracks and depressions, but also on surface. Beams with a maximum fatigue load of 0.4Pu have the largest number of crystals, which are flaky.

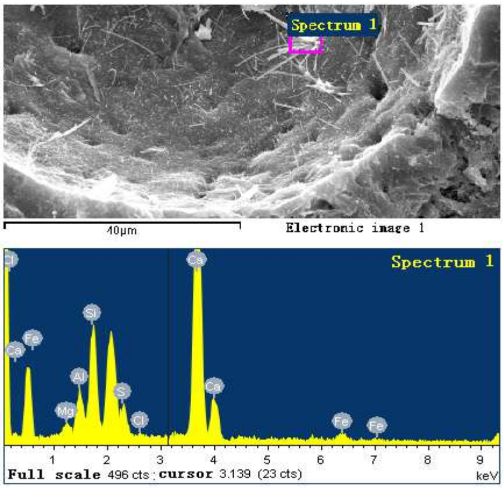

(a) beams without fatigue load

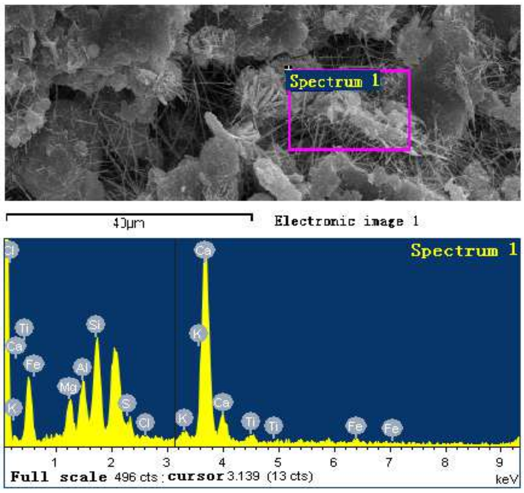

(b)beams with 0.16Pu fatigue load

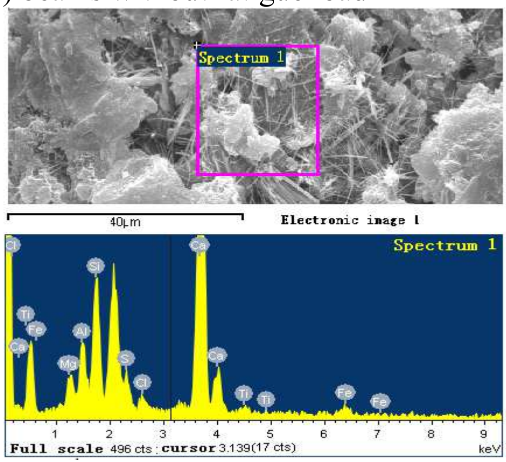

(c) beams with 0.24Pu fatigue load

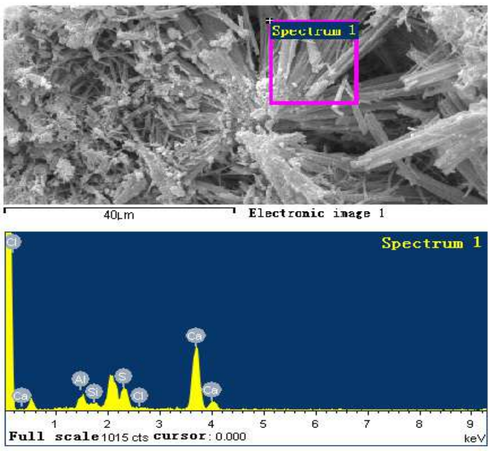

(d)beams with 0.32Pu fatigue load

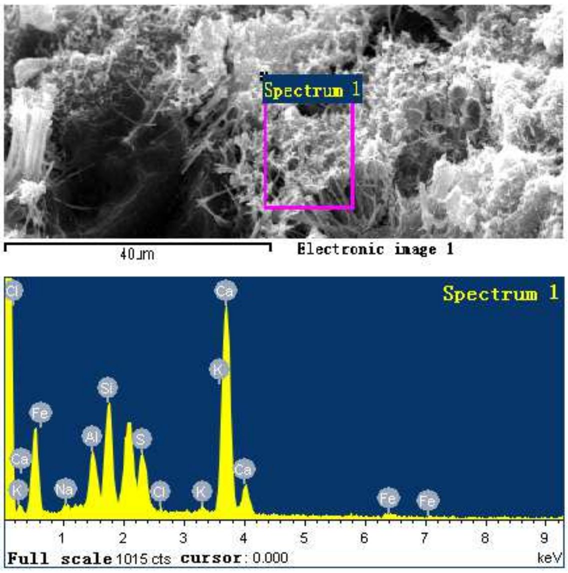

(e) beams with 0.4Pu fatigue load

Figure 6 Crystals condition and component analysis of concrete materials (4000times)

The mass percentages of Cl and S element in the concrete beams by SEM under different fatigue stress are shown in table 6. It can be seen that when the maximum fatigue load is greater than 0.16Pu, visible cracks appeared in the concrete. S element content increases while fatigue load increase until the concrete crack width is greater than 0.14 mm. And it believes that concrete crack width has a great impact on the concentration of the S element in concrete. For Cl element, Cl element contents in concrete beams subjected to fatigue load are significantly higher than the reference group (at least double), while less affected by different cracks' width. Thus, in connection with Fig 4, it may be considered that invisible micro-cracks generated by the fatigue loading will conduct to Cl invasion.

Series Number	**Reference Group**	**Group1**	**Group2**	**Group3**	**Group4**
Fatigue load ratio	0	0.16	0.24	0.32	0.40
Max crack width(mm)	0	0	0.10	0.14	0.25
S element mass percentage	1.38	0.89	2.02	7.54	7.07
Clelement mass percentage	0.54	1.67	2.54	1.01	2.21

Conclusion

Through experimental study of the static performance and microstructure properties of reinforced concrete beams, which subjected to different fatigue loads, and then suffered 100 sea water corrosion cycles, the following conclusions can be drawn:

(1) Fatigue loads may cause cracking of reinforced concrete beams, and the crack width increases with amplitude fatigue load and loading times.

(2) Marine sediment generated during dry-wet cycles fills the cracks of concrete beams. 100 seawater dry-wet cycles may heal the cracks whose widths are less than 0.15mm and narrow the cracks whose widths are greater than 0.15mm.

(3) After fatigue loading and seawater corrosion, with increasing fatigue load ratio, micro-fractures in concrete beams get more and deeper with more crystals. When the fatigue load is greater than 0.24Pu, S element concentration in concrete rise rapidly. The upward trend doesn't slow down until the fatigue load is greater than 0.32Pu. For Cl element, invisible micro cracks caused by fatigue loads can make its concentration increase rapidly, while fatigue load and crack width growth makes less affection on its concentration.

Acknowledgements

This work was financially supported by National Natural Science Foundation of China(51108015), and the Open Project of State Key Laboratory of Subtropical Building Science, South China University of Technology (2012KA03).

References

[1] Naiqian FENG, Junwang CAI, Quanlin NIU, Shuhe Zhang. Study of the deterioration and its countermeasures of Shandong coastal highway reinforced concrete bridge, Durability and durability design of concrete structures Proceedings[C]. Beijing: Tsinghua University, 2002:141-147(in Chinese)

[2] Ringota E,Bascou A. About the analysis of microcracking in concrete[J]. Cement&Concrete Composites,2001,22(3):261-266

[3] Zuquan Jin, Wei Sun, Yunsheng Zhang,et al. Damage of concretein sulfate and chloride solution[J]. Journal of the Chinese Ceramic Society,2006,34 (5):630-635(in Chinese)

[4]Gao Rundong, Li Qingbin. Micro-Macro degradation regularity ofsulfate attack on concrete under complex environments[D]. Beijing: Hydraulic Engineering, Tsinghua University,2010(in Chinese)

[5]Diao Bo, Sun Yang, Shaohong Chen, Yinghua Ye, Effect of mixed-erosion freeze-thaw cycles and persistent loading on the behavior of reinforcement concrete beams， ASCE, Journal of Cold Regions Engineering，2011(3)，

[6] Zheng Xiaoning, Diao Bo, Sun Yang. Properties deterioration mechanism of RC beams sustained loading under alternative actions of mix-aggressive solution and freeze-thaw circles[J]. Journal of Building Structures,2009,12:287-291(in Chinese)

[7] Zheng Xiaoning, Diao Bo, Sun Yang, Zhang Wuman. Study of deterioration mechanism of concrete in mix-aggressive and freeze-thaw environment[J]. Journal of Building Structures, 2010, 02: 111-116 (in Chinese)

[8] Geng Jiao, Diao Bo, Chen Shenggang. Degradation mechanism of air-entrained concrete under the alternative actions of freeze-thaw cycles and seawater immersion[J]. Journal of Beijing University of Aeronautics and Astronautics.2013.10:1-5(in Chinese)

Applied Mechanics and Materials Vols. 744-746 (2015) pp 46-52

doi:10.4028/www.scientific.net/AMM.744-746.46

Detection Indicator of Structural Nondestructive Damage Based on Flexibility Curvature Difference Rate

Chang-sheng Xiang[1, 2,a], Yu Zhou[1,b], Sheng-kui Di[1, 2,c], Li-xian Wang[1, 2,d], Jian-shu Cheng[1,e]

[1]School of Civil Engineering, Lanzhou University of Technology, Lanzhou 730050, China

[2]Northwest Center for Disaster Mitigation in Civil Engineering, Ministry of Education, Lanzhou

[a]xiangcs@lut.cn, [b]sakuragi923@foxmail.com, [c]disk@lut.cn, [d]wanglxian@lut.cn, [e]chengjs0207@foxmail.com

Key words: Flexibility Matrix; Curvature Difference Rate; Detection Indicator; Damage Orientation; Numerical Simulation Examples

Abstract: Applied to the structural damage identification, Modal Flexibility is better than the Modal Frequency and Modal Displacement, the indicators of Flexibility Curvature are effective and sensitive. This paper proposes a new detection indicator which is Flexibility Curvature Difference Rate (FCDR) that by using the change rate of diagonal elements of flexibility curvature difference when before and after damage. The numerical examples of a simple beam, a continuous beam and a frame with the damage conditions of the different positions and different degrees are used to verify FCDR. The result shows that FCDR can well identify the numerical examples damages, and sensitively diagnose the damage near the supports of beam and the nodes of framework.

Introduction

Occasional roles such as construction defects, improper uses or earthquakes can cause structural damages [1], which will increase structural flexibility. In recent years, some scholars [2,3,4] used the indicators of flexibility matrix to identify the structural damage, Raghavendrachar M and Aktan AE analyzed the three-span concrete bridge to verify that flexibility indicator has a better recognition sensitivity for damage diagnosis than frequency index and vibration mode index[5], Zhao J and Dewolf JT introduced the sensitivity analysis method which was also proved this conclusion [6]. Zhang and Aktan proposed the Flexibility Curvature with difference method to apply for structural damage identification [7]. Hui Cao proposed Modal Flexibility Curvature, and validly verified the indicators in the damage frame structure identification [8,9]. Yong-mei Li proposed δ-Flexibility Curvature Matrix Diagonal, and validly verified the indicators in various supporting forms of beams [10,11]. Flexibility Curvature methods applied to structural damage identification, which can effectively identify damage's appearance, accurately locate damage's position and qualitatively judge the extent of damage.

This paper proposes a new damage identification indicator: Flexibility Curvature Difference Rate (FCDR), which is obtained by calculating main diagonal elements change rate of δ-Flexibility Curvature Matrix Diagonal. A simple beam and a two-span continuous beam numerical examples with different degree and different position damages, also a single-span three-storey frame structure numerical example with varying cases damages at beams and columns are established to verify the effectivity of FCDR index, which can be analyzed by extracting the model's first three orders modal parameter.

Indicator Definition

Pandey [12] proposed a method to construct the modal flexibility matrix, which can be calculated from the natural frequency matrix $[\Lambda]$ and the mode shape matrix $[\Phi]$ shown as Eq. 1:

$$F = [\Phi]^T [\Lambda]^{-1} [\Phi] = \sum_{i=1}^{n} \frac{1}{\omega_i^2} \phi_i(x) \phi_i^T(x) \tag{1}$$

where $\phi_i(x)$ is the normalized i^{th} mode of vibration vector quantity, ω_i is the i^{th} modal frequency. From the Eq. 1, the higher modal parameter has a small contribution to flexibility matrix, only the low modal parameter can meet the requirement of actual engineering requirement. In Eq. 1, a central difference is calculated at each row of flexibility matrix, shown as Eq. 2:

$$F' = \frac{2l_{i(i+1)}\left[F_j(i+1) - F_j(i)\right] - 2l_{(i-1)i}\left[F_j(i) - F_j(i-1)\right]}{l_{(i-1)i} l_{i(i+1)} l_{(i-1)(i+1)}} \tag{2}$$

in which, $F_j(i)$ is the element of the row difference matrix in i^{th} row and j^{th} column, $l_{(i-1)i}$, $l_{i(i+1)}$, $l_{(i-1)(i+1)}$ is the distance between the element (i-1) and i, i and (i+1), (i-1) and (i+1) respectively.

In Eq. 2, a central difference is calculated at each column of flexibility matrix, shown as Eq. 3:

$$F'' = \frac{2l_{j(j+1)}\left[F'_{(j+1)}(i) - F'_j(i)\right] - 2l_{(j-1)j}\left[F'_j(i) - F'_{(j-1)}(i)\right]}{l_{(j-1)j} l_{j(j+1)} l_{(j-1)(j+1)}} \tag{3}$$

where $F'_j(i)$ is the element of the column difference matrix in i^{th} row and j^{th} column, $l_{(j-1)j}$, $l_{j(j+1)}$, $l_{(j-1)(j+1)}$ is the distance between the element (j-1) and j, j and (j+1), (j-1) and (j+1) respectively.

After twice difference, the dimension of the linear elastic symmetrical structure's flexibility curvature matrix will transform from n×n into (n-1)×(n-1). The flexibility curvature difference matrix can be calculated as following Eq. 4：

$$\Delta F'' = F''_d - F''_u \tag{4}$$

where the subscript u indicates the amount before damage; the d indicates the one after damage.

The main diagonal elements as row order are extracted from the flexibility difference curvature matrix, and lined into a column vector as Eq. 5:

$$FCD = diag(\Delta F'') = [f''_1, f''_2, \cdots, f''_i, \cdots, f''_{(n-2)}, f''_{(n-1)}]^{-1} \tag{5}$$

where f''_i is the element of i^{th} row and i^{th} column.

Last, the flexibility curvature difference's rate of change (FCDR) is acquired by doing a central difference in Eq. 5, shown in Eq. 6:

$$FCDR = diff(FCD) = \left[\delta_1, \delta_2, \cdots, \delta_i, \cdots, \delta_{(n-3)}, \delta_{(n-2)}\right]^{-1} \tag{6}$$

in which $\delta_i = \left|\left(f''_{i+1} - f''_i\right)/l_i\right|$, l_i is the distance between the element i and (i+1) of FCD column vector in Eq. 5.

Numerical Example and Damage Case

The 1st example is a simply supported beam with sectional dimension 0.15m ×0.20m, span 2.0m, the elastic modulus of material is 33.242Gpa, density 2549kg/m^3, Poisson's ratio 0.2. It is divided into 100 beam elements from left to right. The schematic diagram is shown in Fig.1.

The 2nd one is a two-span continuous beam with sectional dimensions 0.3m×0.5m, the left and right span is 2.0m and 3.0m respectively. It is divided into 20 and 30 beam elements accordingly from left to right, material properties are same as the 1st example, shown in Fig.2.

The 3rd one is a three-storey single-span frame with beam cross-sectional dimension 0.2m ×0.4m and column 0.4m ×0.4m, the other properties are in accordance with the 1st example. The height of each storey from the bottom to the top is 3.9m, 3.3m and 3.3m, span of the frame is 6.0m. The 0.3m step length is applied into the beam and column elements division. The three sections of the left column and right one is considered as a whole that means two long columns, shown in Fig.3.

Each case of structural damage is realized by the way of reducing element elastic modulus in 5%, 10%, 15%, 20%, 30% and 40% to simulate local stiffness declination, the element section and mass is not changed. Each case of three examples is listed in the Tab. 1.

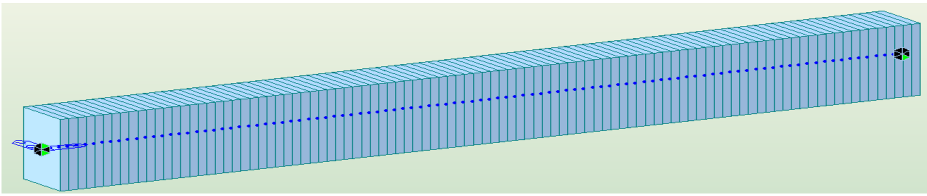

Fig.1. Finite element model of a simple beam

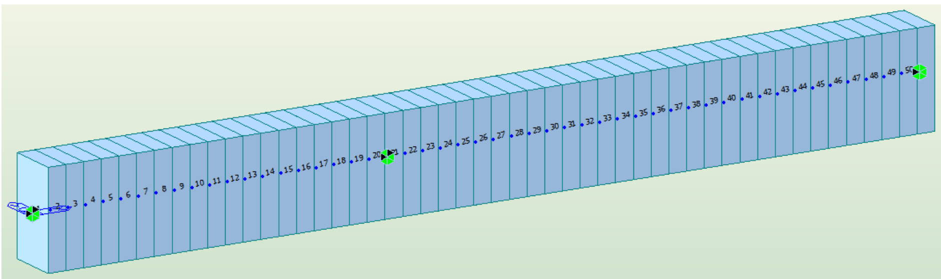

Fig.2. Finite element model of a continuous beam

Table1 Damage cases

Damage Cases		Damage Location(Element Number)	Damage Extent (%)	Result
Simple Beam	One-Damage	Mid-Span(51,52)	5, 10, 20, 30, 40	Fig.4
		Near support(99,100)		Fig.5
	Two-Damage	Mid-Span, 3/4th Span(50,51&75,76)		Fig.6
		Mid-Span, Near Support(51,52&99,100)		Fig.7
Continuous Beam	Multiple Damage	Left- Mid-Span, Right- 3/4th -Span, All Supports (1,2&10,11&20,21&40,41&49,50)	5, 15, 40	Fig.8
Frame	Beam-Damage	1st-Floor-Beam(1,2&10,11) 2nd-Floor-Beam(21,22&35,36) 3rd-Floor-Beam(50,51&59,60)	5, 15, 40	Fig.9
	Column-Damage	Right-Column(61,62&72,73&85,86) Left-Column(96,97&114,115&129,130)		Fig.10

Identification Result

The finite element model of each example is established by using MIDAS/Civil software with beam element model. The new damage identification indicator which we propose: Flexibility Curvature Difference Rate (FCDR) can be calculated from the first three orders modal parameters by MatLab programming, which can be drawn into damage index graphs for identification. It should be pointed out that the vertical modal vector is applied for the first two examples and frame beams, the horizontal modal vector in X-Z plane for frame columns [9] to solve flexibility matrix.

Identification Result of Simple Beam

The simply supported beam one-point and two-point damage identification results are shown in Fig.4~ Fig.7.

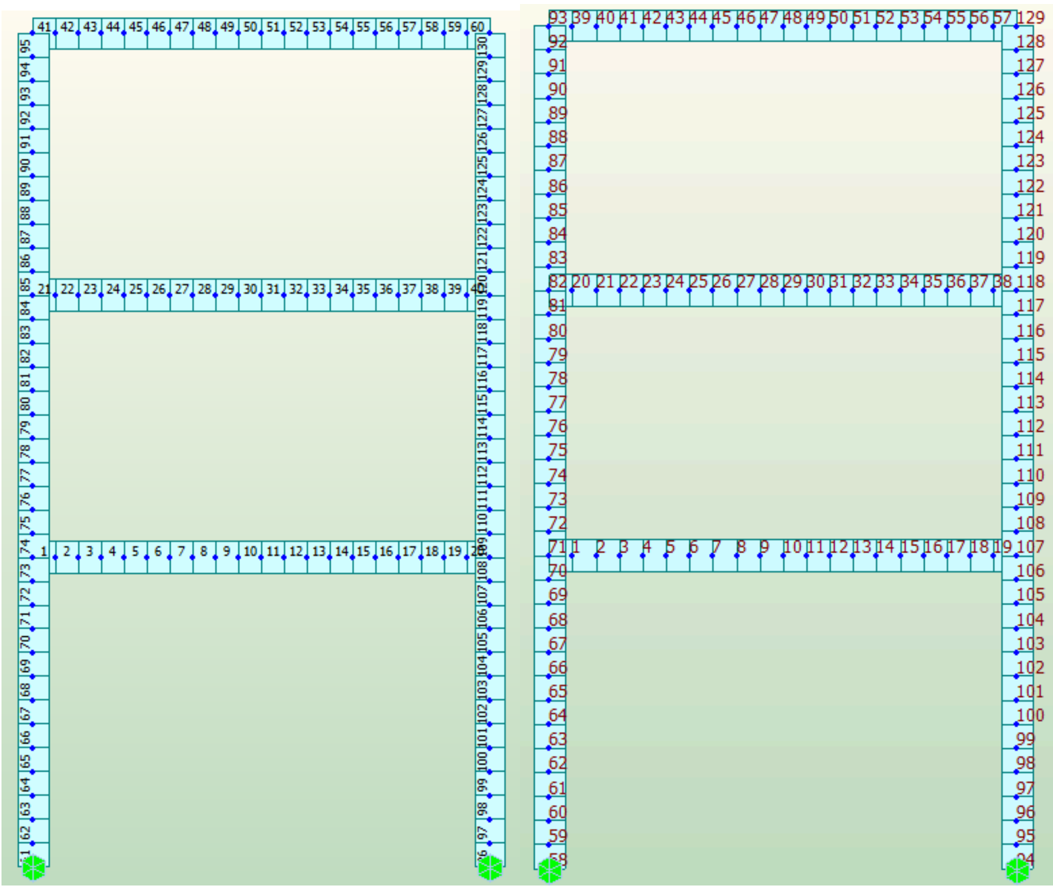

(a) Element Number **(b) Node Number**

Fig.3 Finite element model of a three-layer of single span frame

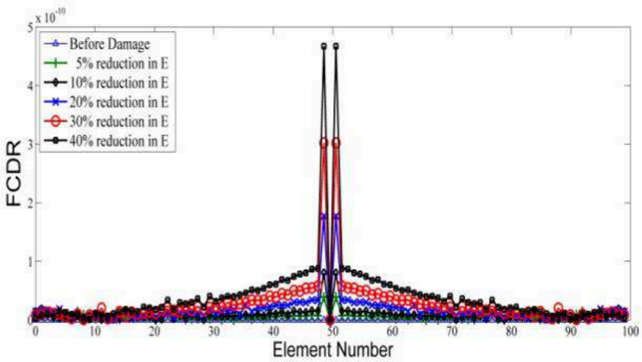

Fig.4. Damaged in the mid-span

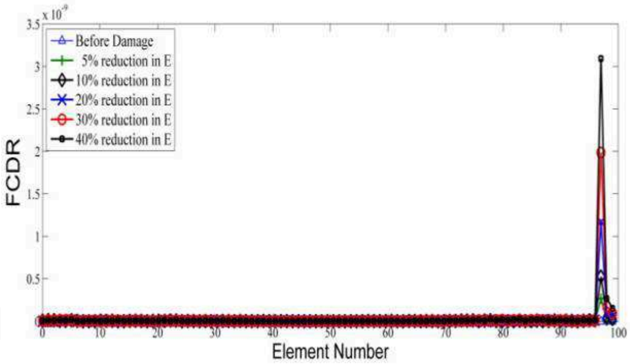

Fig.5. Damaged near the support

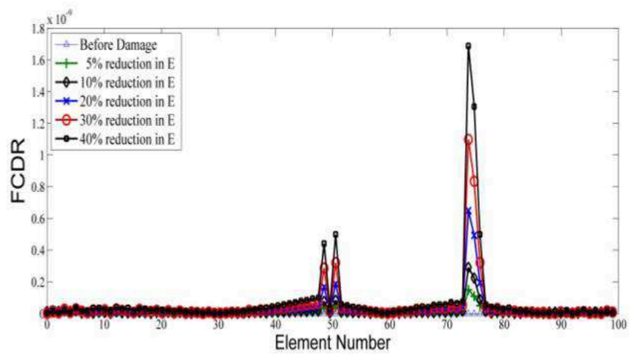

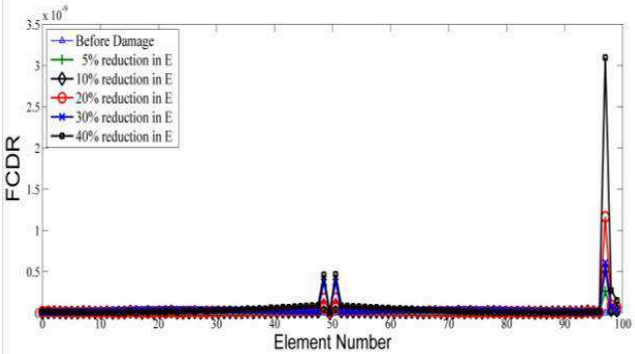

Fig.6. Damaged in the mid-span & the 3/4th span **Fig.7. Damaged in the mid-span & support**

From Fig.4~Fig.7, the peak position appeared of each case in the FCDR indicator curve at the mid-span, 3/4th span and near the support, can be observed visually to match with the damage position in Table 1, and the amplitude differences at the peak position can also be obviously indicated the reduction degrees. From the above results, FCDR indicator applied to identify simply supported beam damage can locate the damage position precisely, and determine the extent of damage qualitatively. It can be seen by comparing the curve of Fig.6 and Fig.7, the magnitude of the mid-span is significantly less than the 3/4th span damage, and those at the support are higher than other position which means that FCDR indicator is more sensitive to identify support damage.

Identification Result of Continuous Beam

The continuous beam multiple damage identification curves are shown in Fig.8:

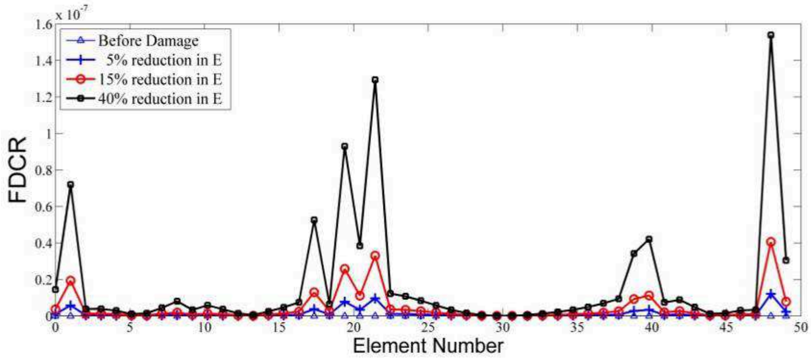

Fig.8. Multiple damaged in a continuous beam

In the Fig. 8, the peaks position appeared at the 1, 2, 17, 19, 20, 21, 39, 40, 49, 50 element are well agree with the location of each element damage listed in Tab.1, the peak at the left mid-span damage is lower than others. FCDR indicator curve magnitude near the support is significantly greater than the magnitude of the left mid-span and right 3/4th span damages, which proves that the indicator used to identify damage near the support of continuous beams is more sensitive than other locations.

Identification Result of Frame Structure

The frame structure multiple damage FCDR indicator curves are shown in Fig.9 and Fig.10:

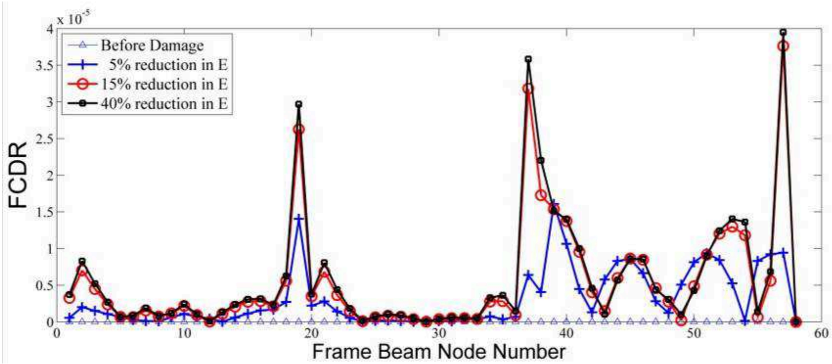

Fig.9. Multiple damaged in frame beam

In Fig.9, FCDR indicator curves show that the location of peak can be identified the damage element at 1, 2, 21, 36, 51and 59 of the frame beam, which is accurately coincide with the location in Tab.1. From Fig.10, the peak of the frame column appears at 61, 62, 72, 73, 85, 86, 96, 97, 114, 115, 129 and 130 element, which is consistent with the damage location that is introduced in the damage case. Therefore it can be proved that the FCDR index is valid and reliable to verify the frame damage, and more sensitive at the nearby nodes of frame than other positions.

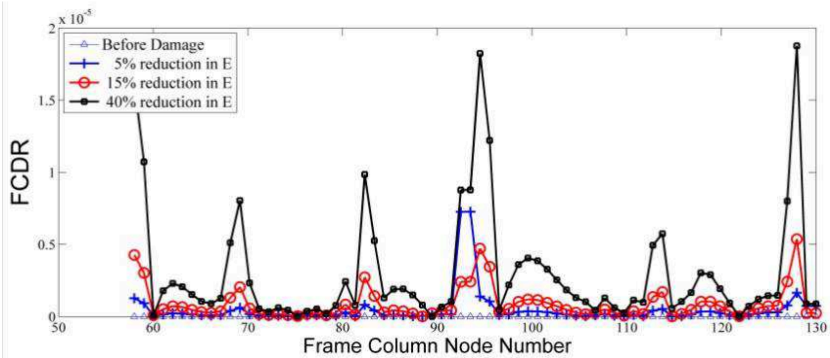

Fig.10. Multiple damaged in frame column

Conclusions

This paper proposes a new damage identification indicator: Flexibility Curvature Difference Rate (FCDR), which is deduced by main diagonal elements change rate of δ-Flexibility Curvature Matrix Diagonal. Three numerical examples of the simple beam, continuous beam, and single-span three-storey frame structure are analyzed to verify the proposed indicator. The result shows that:

(1) FCDR index can be used as the damage identification indicator of simple beam, continuous beam and frame structure. The indicator is a reliable and accurate method that can locate damage and judge the extent in structural damage detection.

(2) The result of numerical examples shows that FCDR indicator can better identify the appearance of damage near the nodes. By contrast, the damage far away from the nodes is less sensitive, but it can be deduced by the peak location.

(3) The influence of noise in field test is not considered in this article, the anti-noise effect of FCDR index should be verified further.

Acknowledgements

This work is sponsored by the Colleges and Universities Basic Research Foundation of Gansu Province and the Natural Science Foundation of Gansu Province Project, China (Grant No. 2014GS02269).

References

[1] RayW. Clough, Joseph Penzien. Dynamics of Structures [M]. Beijing: Higher Education Press, 2006
[2] Pandey A K, Biswas M, Samman M M. Damage detection from changes in curvature mode shapes [J]. Journal of Sound and Vibration, 1991, 145: 321~332.
[3] Toksoy T, Aktan A E. Bridge-condition assessment by modal flexibility [J]. Experimental Mechanics, 1994, 34: 271-278.
[4] Doebling SW, Farrar CR, Prime MB, Shevitz DW. Damage identification and health monitoring of structural and mechanical systems from changes in their vibration characteristics: a literature review. Report no. LA-13070-MS, Los Alamos National Laboratory, Los Alamos (USA); 1996. 2: 1114~1116.
[5] Raggavendrachar M, Aktan A E. Flexibility by multi-reference impact testing for bridge diagnostics [J]. Journal of Structural Engineering, 1992, 118(8): 2186-2203.
[6] Zhao J, DeWolf J T. Sensitivity study for vibrational parameters used in damage detection [J]. Journal of Structural Engineering, 1999, 125(4): 410-416.
[7] Zhang Z & Aktan A E. The damage indices for the constructed facilities [C]. Proc. 13th Int. Modal Analysis Conf. 1995. 2: 1520~1529.
[8] Hui Cao, Michael I Friswell. Nondestructive damage evaluation indicator based on modal flexibility curvature [J]. Engineering Mechanics, 2006, 24(4): 33-38. (in Chinese)
[9] Hui Cao, Xinliang Zhang, Yingmin Li. Identify frame damage based on the modal flexibility curvature difference [J]. Journal of Vibration and Shock, 2007, 26(6):116-120. (in Chinese)
[10] Yongmei Li, Xiyuan Zhou, Xiangyu Gao. Detection indicator of structural non-destructive damage based on curvature-flexibility difference matrix [J]. Engineer Mechanics, 2009, 26 (2): 188-195. (in Chinese)
[11] Yongmei Li, Xiyuan Zhou, Xiangyu Gao, et al. Damage diagnosis of beam structures by flexibility curvature method [J]. Journal of Beijing University of Technology, 2008, 34 (11):1173-1178. (in Chinese)
[12] Pandey A K, Biswas M. Damage detection in structures using changes in flexibility [J]. Journal of Sound and Vibration, 1994, 169: 3~17.

Applied Mechanics and Materials Vols. 744-746 (2015) pp 53-58

doi:10.4028/www.scientific.net/AMM.744-746.53

Discussion About the Development Principles of Reinforced Location Test Instrument Calibration Components

Zhengyue Ren[1,a], He Huang[2,b],Lu Liu[3,c] and Jing Liu[4,d]

[1]Institute of Building Materials,Dalian University of Technology,Dalian 116024,China

[2]Institute of Building Materials,Dalian University of Technology,Dalian 116024,China

[3]Institute of Highway Science ,Ministry of Transport,Beijing 10088,China

[4]Institute of Highway Science ,Ministry of Transport,Beijing 10088,China

[a]110760@qq.com,[b]172334511@qq.com,[c]lu.liu@rioh.cn,[d]jing.liu@rioh.cn

Keywords:calibration components;calibration;reinforced location tester;protective layer thickness; error value

Abstract: The calibration of the concrete-rebar detection system use the calibration components made by the various metrological verification units commonly,and the value cannot be traced back.In this paper, the development principles of the calibration components is analyzed systematic. The position of the reinforced bar on the influence of the result of the test was tested by using the HC - GY61 reinforced location tester,from which come to a conclusion of the design reference of Φ12,Φ16,Φ20 and Φ25 while the value error is in ±1mm and 0mm,which also can provide a reference for industries developed calibration components.

Introduction

The reinforced concrete location tester is mainly used for testing reinforced protective layer thickness, rebar diameter and bar spacing in building engineering, transportation engineering, water conservancy projects and port engineering. Besides, the test results can be used as reports of the engineering quality appraisal. As a result, the accuracy of the test results is directly related to the engineering quality evaluation.

At present, various industries did not establish measurement standard of calibration components which are used to calibrate the reinforced concrete location tester. The construction industry has only the calibration specification of reinforced location meter, so the value of the concrete reinforcement position meter can not be effectively traced. The calibration of the concrete reinforced location is meter mainly referenced as "the testing technical specification of the reinforcement in the concrete"(JGJ/T152-2008) [1] and "the calibration specification of the steel protective layer, floor thickness measurement instrument"(JJF1224-2009)[2]. But these standards are mainly used in the construction projects, no corresponding calibration standards or specifications for other industries, the provincial or municipal units mainly based on the calibration standard of the construction projects to develop different components.Calibration components material normally uses concrete,the same material as the actual project. Due to the choice of the steel bar diameter size and reinforced location setting generally have no specific reference, there are a lot of problems in the calibration components. For instance, concrete reinforcement position tester can't accurately measure the steel bars number, diameter of steel bars and reinforced protective layer thickness, etc. under the condition of small steel spacing. Under this circumstance, the design and manufacture of unified calibration components is very important. Meanwhile,in order to implement the value dissemination and traceability, a measurement standard about calibration components needs to be established.

Problems in Researching Calibration Components

This part mainly analyzes some good research methods from the database.

Engineer Li by his actual testing work, refering to relevant data and combined with the specific characteristics of the equipment (Swiss production PROFOMETER type 5) designed and made out the standard calibration components of reinforced concrete refer to his article[3] - put four steel bar respectively with same diameter in the position of the steel protective layer thickness of 30 mm, 35 mm, 40 mm and 45 mm , then to establish the "reinforced protective layer thickness detector calibration method". This method had been put on records in bureau of technical supervision ,xinjiang autonomous region. However, the test error is larger. on one hand, the same diameter steel quantity is little, only repeated measurement was used to determine the deviation of the value. on the other hand, the position of the steel can't guarantee its level ,which would lead to big error value.

Put Φ35,Φ28,Φ20,Φ15 and Φ10 on a right triangle steel frame with concrete pouring into an organic whole is another way as Zhang Duxian stated[4] ,a researcher at Nanjing measurement test. If The height error of the reinforcedis not more than± 0.20 mm, the distance error of the steel bars would within 90± 0.10 mm.Such verification device can ensure the accuracy of the protective layer and the level of the steel. But when calibration instrument was implemented, the steel frame will affect reinforced secondary magnetic field distribution, directly impact the value accuracy.

Other researchers [5-7] tested and analyzed of affecting factors of steel bar diameter, reinforced protective layer thickness and reinforcement spacing through designed standard specimens by themselves , but the content is too little,and there is no systematic research. Thus it requires to research the influence of the measured true value the on different diameter steel, protective layer thickness and the different distance of steel bars.

Developed Basis of Calibration Components

According to the need of the calibration of instruments and the measurement of the calibration component, reinforced position meter calibration components' development need to comply with the following principles.

Refer to the Relevant Testing Standards, Rules or Regulations

The calibration of reinforced location meter is used ultimately for ensuring the accuracy of the test, so the calibration component needs to accord with the actual relevant test procedures. Now it can reference in the construction engineering industry standard — " construction quality acceptance specification of concrete structure engineering (GB 50204-2011)"[8], "the standard of building structure detection technology (GB/T50344-2004)"[9], "the test technical specification of reinforcement in the concrete (JGJ/T152-2008)" [1] and"the technical specification of testing reinforced protective layer thickness and steel bar diameter with the electromagnetic induction method (DB11 / T365-2006)"[10].

Specification [3] has been clear about the allowable error of the protective layer thickness design values in testing the reinforced concrete protective layer thickness(beam type is from -7mm to +10mm and plate type is from -5mm to +8mm).

It is only given allowed error(±1mm) for testing the reinforcement protection layer thickness in 10 mm to 50 mm range, not involved in detection permissible error when more than 50mm range refer to 3.2.1 in specification[1].And testing steel bar diameter takes the method of combining testing , drilling and carved slot refer to 3.2.1 in specification[1],which also notes the accuracy of measurement is in 0.1mm.

It made following provisions about the allowable error of testing the reinforced protective layer thickness refer to 4.3.2 in specification[10]: the allowable error is ±1mm in below 40mm (including) and ±2mm from 40mm to 60mm (including),reinforced protective layer thickness in more than 60 mm, and its measurement error should be allowed no more than 10% of the reinforced protective layer thickness design value. The allowed error is ±2mm in testing steel bar diameter refer to 4.4.2 of specification[10].

From these rules and regulations, we can analyze the industry standards and local standards not form a good docking, and at present, only BeiKing introduced a local standards.

Refer to Relevant Calibration Specification

Calibration specification is written for calibration components, but it can be referenced in the measurement standard only "the calibration specification of the steel protective layer, floor thickness measurement instrument (JJF1224-2009)" [2]. Requirements about error in the specification(the H_0 as the lower limit of measurement, the H_s as the upper limit of measurement,the H as the protective layer thickness) :the maximum permissible error is ±1mm when steel bar diameter is 8mm~12mm and protective layer thickness is from H_0 to 40mm(including),and is ±1mm when steel bar diameter is 14mm~20mm and protective layer thickness is from 40mm to 60mm(including), and is ±(1mm+3%H_S) when steel bar diameter is greater than or equal to 22mm and protective layer thickness is from 60mm to H_S(including). In appendix B, ignoring the measurement of reinforcement spacing and uncertainty analysis, production requirements for standard piece only gives a protection layer thickness value and a reinforced value. For reinforced location tester, only with a steel bar to calibrate instruments is not enough, because components have at least two steel bars in engineering test. With a steel bar to the calibration will neither unstandard nor represent of the actual detection error; Moreover, when measured reinforcement with adjacent, measurement error of the measured reinforcement will increase under near reinforced magnetic interference.

Refer to Relevant Design Specifications

Reinforced protective layer thickness selection principles: according to "concrete structure design Specification(GB 50010-2010)" described in 8.2[11],the outermost layer of reinforced protective layer thickness should be consistent with the provisions of table 8.2.1 while the design use year of concrete structure is 50 years ,and the outermost layer of reinforced protective layer thickness should be not less than 1.4 times of table 8.2.1 while the design use year of concrete structure is 100 years.In table 8.2.1, the minimum thickness of protective layer is 15mm for the board, wall, shell of environmental categories(one) ,and the biggest thickness of protective layer is 50mm for the beam, column, bar of environmental categories(three b), namely the scope of cover design is from 15mm to 50mm.According to the requirement of the design use year ,100 years ,the cover design scope should be from 21mm to 70mm, so the test of reinforced protective layer thickness in the design of test range selected from 15mm to 70mm. Some erosion seriously environmental need to increase the thickness of protection layer, but at home and abroad the measurement accuracy of the reinforced location tester will be greatly reduced when covering more than 70mm .

Steel bar diameter selection principles: as the detection accuracy of the steel meter for small diameter and large diameter steelbar is not high, so we can use the steel bar diameter of 8mm , 10mm, 12mm, 16mm, 20mm, 25mm, 28mm and 32mm in design of test.

Steel bar spacing selection principles: the choice of reinforcement spacing generally depends on the reinforcement ratio, thus the spacing can be chose 80mm, 100mm ,150mm, 180mm and 200mm. But according to common sense,we can know the distance to add is meaningless when steelbar spacing gradually increases to a certain distance. The setting of bar spacing can't be designed too small to affect the precision of the instrument ,which is the design principle of spacing for the calibration components.

The Effect of the Reinforced Location on the Result of Measurement

For the error of measurement instrument manufacturer just gives the rough error of measurement, but did not give the overall error for the different reinforcement under different distance or reinforced protective layer thickness value. In addition, even if the selection principles of steel bars covers thickness, rebar diameter and steel spacing, it is not perfect since the actual is combined with three options.

The innovative development of reinforced location tester, named HC - 2013 GY61, has intuitive thickness detection mode, can accurately display position, protection layer thickness value and reinforcement spacing value. It displays only a true value in the absence of magnetic medium interference, while other reinforced location tester gives more value, so we use it to test on the effect of the reinforced location on the result of measurement.In the test, the reinforced protective layer respectively is set to 10mm, 20mm, 30mm, 40mm, 50mm , 60mm and 70mm.Reinforced bar spacing of the initial spacing is steel bar diameter (that means the net spacing of the reinforcing bar is 0mm). Then the spacing increases gradually according to 1/2 times diameter of the measured steel bar, until the spacing is no longer affecting true value of the reinforced protective layer,which means the error is 0mm.The reinforced diameter have Φ12, Φ16, Φ20 and Φ25, if necessary can test other diameter of reinforcing steel bar.

Measured reinforcement only one.It is freely to determine the tested steel bar when there are two bars, and the middle bar is the tested bar when there are three bars.The tested bar does not been moved after setting each protective layer until it is tested over in setted protective layer. We concluded that the value error of different reinforced protective layer for four kinds of diameter of reinforced , this article only gives the value error in ±1mm and 0mm for the reference of setting reinforced location , as shown in Table 1 and Table 2.

Table 1. The reference of setting reinforced location when the value error of protective layer thickness test is in ±1mm

layer thickness (mm)	the number of reinforcement (root)	Φ12(mm)	Φ16(mm)	Φ20(mm)	Φ25(mm)
10	2	J≥2.5D	J≥2.5D	J≥1.5D	J≥1.5D
	3	J≥3.0D	J≥2.5D	J≥2.0D	J≥1.5D
20	2	J≥3.5D	J≥2.5D	J≥2.0D	J≥1.5D
	3	J≥4.0D	J≥3.0D	J≥2.0D	J≥2.0D
30	2	J≥3.5D	J≥3.0D	J≥2.0D	J≥2.0D
	3	J≥4.0D	J≥3.5D	J≥2.5D	J≥2.5D
40	2	J≥4.5D	J≥3.5D	J≥3.0D	J≥2.5D
	3	J≥5.0D	J≥4.0D	J≥3.0D	J≥3.0D
50	2	J≥5.0D	J≥4.5D	J≥3.0D	J≥2.5D
	3	J≥6.0D	J≥5.0D	J≥3.0D	J≥3.0D
60	2	J≥6.0D	J≥5.0D	J≥3.5D	J≥3.0D
	3	J≥7.0D	J≥5.5D	J≥4.0D	J≥3.5D
70	2	J≥7.0D	J≥5.0D	J≥4.0D	J≥3.5D
	3	J≥7.0D	J≥5.5D	J≥4.5D	J≥4.5D

Note: J as bar spacing; D as the tested steel bar diameter (mm).

Table 2. The reference of setting reinforced location when the value error of protective layer thickness test is in 0mm

layer thickness (mm)	the number of reinforcement (root)	Φ12(mm)	Φ16(mm)	Φ20(mm)	Φ25(mm)
10	2	J≥3.5D	J≥4.0D	J≥2.0D	J≥2.0D
	3	J≥3.5D	J≥4.0D	J≥2.5D	J≥2.0D
20	2	J≥4.5D	J≥3.0D	J≥2.5D	J≥2.0D
	3	J≥5.0D	J≥3.5D	J≥3.0D	J≥2.5D
30	2	J≥4.5D	J≥3.5D	J≥2.5D	J≥2.5D
	3	J≥5.0D	J≥4.0D	J≥3.0D	J≥3.0D
40	2	J≥5.0D	J≥4.5D	J≥3.5D	J≥3.0D
	3	J≥5.5D	J≥5.0D	J≥3.5D	J≥3.5D
50	2	J≥6.0D	J≥5.5D	J≥3.5D	J≥3.0D
	3	J≥7.0D	J≥6.0D	J≥3.5D	J≥3.5D
60	2	J≥7.0D	J≥6.5D	J≥5.0D	J≥3.5D
	3	J≥8.5D	J≥7.0D	J≥5.0D	J≥4.0D
70	2	J≥7.5D	J≥5.5D	J≥5.0D	J≥4.0D
	3	J≥8.5D	J≥6.5D	J≥5.0D	J≥5.0D

Note: J as bar spacing; D as the tested steel bar diameter (mm).

Stability of the Materials

The calibration components require that material is not affected by the external environment, reinforced don't deformation and be corroded, etc. Therefore reinforced is best round stainless steel, medium material can use other materials, such as organic glass, quartz glass,etc.

The Use and the Traceability of Reinforced Location Tester

Reinforced location tester will encounter many problems in the process of use and traceability, so research and discuss these problems is important begin desigh calibration components. The investigation table about the use and traceability of reinforced location tester as shown in Table 3. According to the research on three detection unit in DaLian area and a detection unit in GuangXi province, we can see that the source parameters only displayed the reinforced protective layer thickness,and the instruments existed much effect in the process of test,such as drift, near steel, the protective layer thickness,etc,which should lead biggermeasurement error to the test of the reinforcemen spacing and diameter.

Table 3. The research table on the use and the traceability of reinforced location tester

unit name	instrument model	traceability way	traceability parameter	problems in using
Guangxi innovation construction engineering quality test and consulting co., LTD	KON-RBL(D)	calibration	measurement uncertainty of reinforced protective layer thickness : U = 1 mm, k = 2	measurement error of the steel bar diameter is larger and small bar spacing cannot test the number of steel bar root and position, etc
Dalian BoHai detection co., LTD	KON-RBL(D)			test error is bigger while partial big protective layer thickness
Dalian construction engineering quality test center	HC-GY6			close bars affect test result
DUT modern engineering detection co., LTD	PS200S			measuring instability and exist drift

Outlook

Reinforced location tester is now widely used to reinforced concrete nondestructive testing, also can meet the needs of engineering detection. But ,there is no calibration and measurement standard for calibration components,so various industries dedicate concrete reinforced location tester metrological verification procedures and standards of measurement become the important direction of the reinforcement position meter calibration.In the future,after implementing of concrete reinforced location meter measurement standard device research and development, this kind of measuring instrument will be applied to metering stations, which can ensure the accuracy of the reinforced concrete position meter measuring results and achieve its value traceability.

References

[1] JGJ/T152-2008:The Detection Technology Discipline of Rreinforcement in Concrete [S].Beijing:China Building Industry Press(2008).

[2] JJF/1224-1224:Calibration Specification of the Reinforced Protective Layer Thickness, Floor Thickness Measurement Instrument[S]. Beijing: China Metrology Press(2009).

[3] Fei Li and Yi Li:Calibration Method of Reinforced Protective Layer Thickness Detector [J].Measurement and Testing Technology,Vol.10(2006).

[4] Duxian Zhang and Zheng Qian:Development of Reinforced Location Meter Calibration Device[C].Academic Papers of Measurement of JIANGSU Province (2006),P.21 ~ 22.

[5] Qiming Zhang:The Test And the Main Influence Factors of Reinforced Protective Layer Thickness Analysis [J].HENAN Science,Vol. 28 (2010),P.201 ~ 203.

[6] Hui Zhao,Xiaoming Wu,Guanguo Liu and Li Huang: The Influence Factors of Reinforced Concrete Protective Layer Thickness Precision [J]. JIANGSU Traffic Science and Technology, Vol.4(2012) ,P.60-62.

[7] Weiping Li,Conghui Wang:The Dand Resolution on the Location, Protective Layer Thickness of Steel Bars and Ssteel Bar Diameter[C].The 8th National Construction Engineering Nondestructive Testing Technology Conference, in GUILIN, China(2004).

[8] GB 50204-50204:The Concrete Structure Engineering Construction Quality Acceptance Specification[S].Beijing:China Building Industry Press (2011).

[9] GB/T50344-2004:The Detection Technology Standard of The Building Structure[S]. Beijing: China Building Industry Press (2004).

[10] DB11/T365-2006:The Technical Specification of Testing Reinforced Protective Layer Thickness and Steel Bar Diameter with the Electromagnetic Induction Method[S].Beijing:China Building Industry Press (2006).

[11] GB 50010-50010:The Design Specification of The Concrete Structure[S].Beijing:China Building Industry Press(2010).

Applied Mechanics and Materials Vols. 744-746 (2015) pp 59-64
© (2015) Trans Tech Publications, Switzerland
doi:10.4028/www.scientific.net/AMM.744-746.59

Durability design of marine concrete structure considering the influence of load

Jianbo Xiong [1,2,a], Chunlin Deng[2,b]

[1] Department of Materials Science and Engineering, South China University of Technology, Guangzhou, Guangdong 510640, China

[2] CCCC Fourth Harbor Engineering Institute Co., Ltd., Key Laboratory of Harbor & Marine Structure Durability Technology Ministry of Communications, PRC, Guangzhou, Guangdong 510230, China

[a]xjianbo@gzpcc.com, [b]dchunlin@gzpcc.com

Keywords: Bending tensile stress, Diffusion coefficient, Durability design, Stress level

Abstract. In this paper, based on accelerated testing indoors, under the action of bending tensile stress on a marine high-performance concrete chloride ion diffusion coefficient, the results show that: Subjected to bend under the action of tensile stress and do not withstand the test piece chloride diffusion coefficient increases with increasing stress levels, different tensile stress and does not bear the stress of the concrete chloride ion diffusion coefficient ratio(D_η/D_0)exponential relationship with the stress level(η). In addition, addition, for a domestic Bridge, preliminary design to determine typical parameters of components and their environment is proposed to consider the durability of concrete structure load control index calculation method, to establish a "design life - chloride ion diffusion coefficient controlled targets" the correspondence between, for similar projects designed to provide a reference durability.

Introduction

As we all know, in ocean environments, chlorine salt erosion leading to steel corrosion is one of the main causes of premature damage of concrete structures. During concrete structure's durability design, now a representative of service life prediction of concrete structures in a chloride environment model, including United States Life-365 calculation software model, Europe is represented by the FIB and Dura Crete reliability model [1-4]. These models assume that diffusion of chloride ion in concrete to meet conditions of Fick's second law of diffusion theory, on this basis, to adopt the necessary laboratory and field exposure test pieces test, to complement the model parameters; calculations in the model force factor do not take into account the structure of the actual load effect on the durability. However, the mainly root cause of premature failure of concrete structures is that any kind of concrete materials and structures are subjected to external loads at the same time experiencing the environmental effects [5-6]. A combination of factor's effect on durability of marine concrete, has caused more and more concrete scientific workers attention [7-10].

Existing research has shown that concrete durability and loads in a service environment have a very close relationship [11-14]: With increased levels of loading, tension zone of concrete resistance to chloride ion erosion reduced capacity, compression zone of concrete resistance to chloride ion erosion increased capacity; withstand tensile stress than under compressive stress of concrete structure faced more serious problems of interaction between load and environment [15-16]. While some scholars on the permeability of concrete under loading must be explored, but the test results vary, test conditions and substantial service of concrete in the stress state, the substantial materials used in concrete, there are still major differences. In addition, marine engineering high-performance concrete with low water-Binder ratio, admixture of high content quality characteristics, load on its resistance to chloride ion permeability effects may differ from ordinary concrete.

This article is a 100-year design life of the bridge project as an example, for its preliminary design to determine the tower, pier, girder, pile and other components of the basic parameters of the introduction of bending stresses its role in the drop-down used marine high-performance concrete resistance to chloride ion penetration performance, designed for durability, and ultimately gives life to meet the design requirements of the concrete life of chloride ion diffusion coefficient control targets.

Bending Tensile Stress under the Action of Marine Engineering High-performance Concrete Chloride Ion Penetration Resistance

Specimen Molding. Marine high-performance concrete cross sea bridge by using C40~C50 ranks more concrete [17,18], water cement ratio is generally 0.32~0.36. In this paper, according to the water binder ratio 0.35, cementations materials dosage 420kg/m^3, which with 20% fly ash, ground granulated blast furnace slag powder content 40%, forming the 100mm × 100mm × 500mm concrete specimens.

Test materials are as follows: Guangzhou Zhujiang Cement Limited production of Portland cemented Yue Xiu PII 42.5; Shajiao power plant in Guangzhou to provide of I grade fly ash; Guangdong Shaoguan Shaogang Jiayang S95 granulated blast furnace slag powder; Guangdong Xijiang freshwater sand; Huizhou Sun Taiji 5 ~ 20mm granite quarry gravel; Guangzhou four aircraft polycarboxylate superplasticizer, water-reducing rate is 25% .

Test Method and Process. Test loading device design is shown in Figure 1.[19], physical loading process diagram as shown in Figure 2.

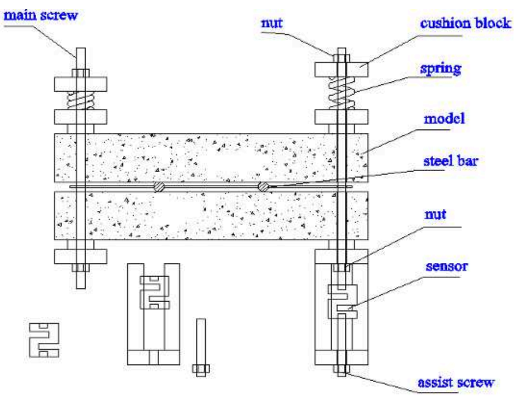

Figure 1 Device schematic.

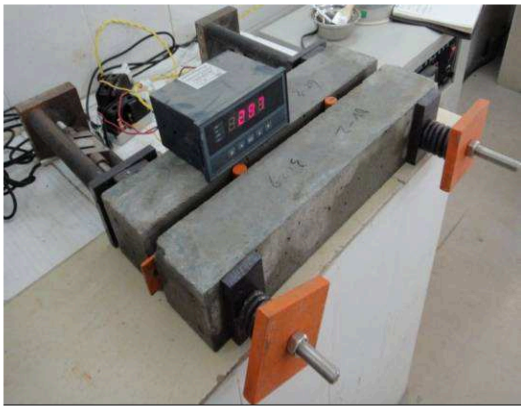
Figure 2 Loading test photos.

Bending load used four points bending loading mode, the tensile stress levels were flexural strength of concrete 28 days 0%, 10 %, 30 %, 40 %, 50%. Specimens cured for 28 days after the implementation of the load, and then placed in artificial seawater splash zone simulation chamber exposure, artificial seawater concentrations at 5%(NaCl concentration). Frequency is set to spray every six hours, a 3-minute exposure test age of 60 days. After the exposure test, the specimen centered 100mm section position (pure bending segment tension zone) along the penetration direction by 1,2,3,4,6,8,10,12 mm drill powder samples of eight layers, testing concrete chloride ion content.

Test Results. The test piece that stress levels are 0%, 10%, 30%, 40%, 50%,each layer of concrete chloride ion concentration measurement values shown in Figure 3. The concentration of chloride ion in concrete with the increase of stress level, using the least-squares regression concrete bending the chlorine ion diffusion coefficient D, the results were 0.91×10^{-12}, 1.11×10^{-12}, 1.47×10^{-12}, 1.79×10^{-12}, $2.17\times10^{-12}m^2/s$.

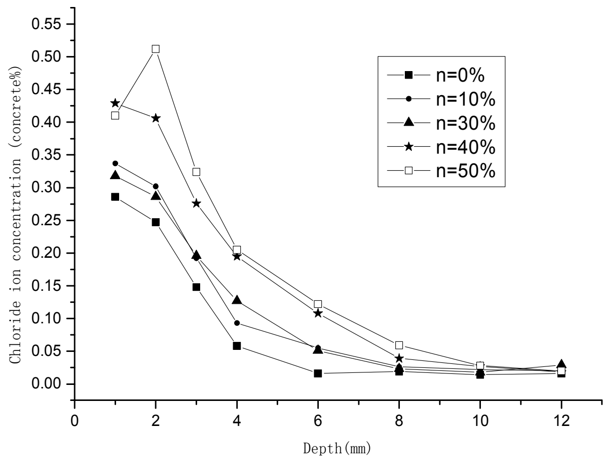

Figure 3 Under different stress level distribution of the concentration of chlorine ion in ioncrete

Data Analysis. Different stress levels chloride diffusion coefficient of the fitted values shown in Table 1. The stress level of 10 %, 30 %, 40 %, 50 %, the chloride ion diffusion coefficients were 1.22, 1.62, 1.97, 2.38 times when no load. It can be seen: the bending tensile stress will increase marine high-performance concrete chloride ion diffusion rate, the higher the stress level, the greater the chloride ion diffusion coefficient of concrete [15]. So during the durability of concrete structure's design, in order to meet the intended design life of concrete structures subjected to bend down stress, the diffusion coefficient was no control indicators should load when the control index 0.819,0.619,0.508,0.419 times.

Table 1 Different levels of stress on chloride diffusion coefficient of the control value

Stress level η	0%	10%	30%	40%	50%
D （$\times 10^{-12} m^2 \cdot s^{-1}$）	0.91	1.11	1.47	1.79	2.17
D_η/D_0	1	0.819	0.619	0.508	0.419

D_η/D_0 is the variable stress level as the independent variable, after fitting, the diffusion coefficient under load control values with and without load the control value relations conform to Equation 1, shown in Figure 4.

$$D_\eta = D_0 * （0.995e^{-1.69}) \tag{1}$$

η is the bending load tensile stress level; D is the stress level of the role of the diffusion coefficient of concrete indicators; D_0 is no diffusion coefficient of concrete under load control indicators, shown in Figure 4.

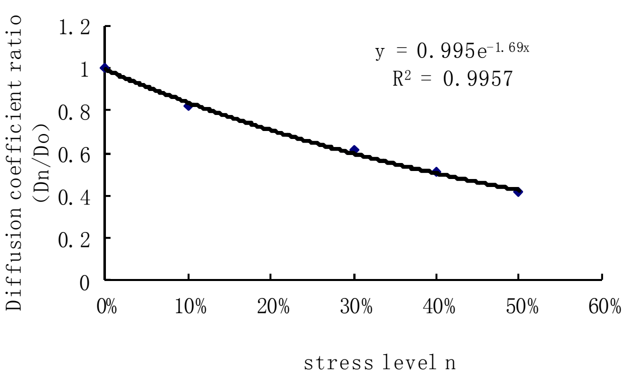

Figure 4 Different levels of stress on chloride diffusion coefficient.

From Figure 4, D_η/D_0 and Load level have a good load level exponential correlation, regression correlation coefficient $R^2=0.9957$; that is, with the increase of load level, meet the same useful life, the chloride diffusion coefficient control indicators should be presented index decreased.

Life Prediction of Concrete Structures

Life Prediction Model. Fick's second law is widely used to simulate the chloride ion in concrete migration law, see Equation 2.

$$\frac{\partial C}{\partial t}=D_t\frac{\partial^2 C}{\partial x^2} \tag{2}$$

C is the concentration of chloride ions in the concrete (accounting for the quality of cementations material %); t is the chloride ion in concrete diffusion time (a); x is the thickness from the surface of the concrete (mm); Dt as chloride ion in a concrete effective diffusion coefficient (mm2/a).

Assumed surface chloride concentration C_s, the initial concentration of chloride ions in concrete C_0, take concrete reinforcing steel and chloride ion concentration reaches a critical concentration C_{cr} as durability limit state design (design life), you can calculate the specific components to meet the design life of t years , the chloride ion diffusion coefficient D_t effective control values , see Equation 3.

$$D_t=\frac{c^2}{4\cdot t\left[erf^{-1}\left(1-\frac{C_{cr}-C_0}{C_s-C_0}\right)\right]^2} \tag{3}$$

Erf is the error function.

According to the research results, the relation between the concrete chloride ion diffusion coefficient D_{rcm} and the effective diffusion coefficient D_t see Equation 4.

$$D_{rcm}=D_t\cdot\exp^{-1}\left[\frac{U}{R}\left(\frac{1}{T_0}-\frac{1}{T}\right)\right]\cdot\left(\frac{t_{rcm}}{t_0}\right)^{-m} \tag{4}$$

D_{rcm} is the chloride ion diffusion coefficient (m^2/s) determined the age of the t_{rcm} (this paper is 28d); U is the chloride diffusion activation energy, 35000 (J/mol); R is the ideal gas constant 8.314 (J/K/mol); T_0 is the reference temperature, 293(K); T is the temperature of the concrete, taking 25℃; t_0 is the chloride ion diffusion coefficient of the attenuation cycle, the reference value 25a; m is the diffusion coefficient of the age of the attenuation coefficient, when mixed with 20% fly ash and 40% granulated blast furnace slag , the attenuation coefficient value of m is 0.59.

Selection of Basic Parameters.

1) Concentration of chloride ions on the surface

To determine the Specimen surface chloride concentration C_s, For example a cross-sea bridge close to the project site has been built similar projects conducted an investigation, and use the second law of FICK curve fitting. It is concluded that the regional atmospheric zone, splash zone, the water level changes in area concrete theory of chloride ion concentration C_s were 0.14%, 0.40%, 0.40% (representing the concrete mass%).

2) Critical chloride ion concentration

According to the project findings [20],reference to foreign-related information, atmospheric zone , splash zone , the water level changes in areas C_{cr} values were 0.10%, 0.05%, 0.10% (Cl^- accounted concrete mass percentage) .

3) The initial concentration of chloride ion

According to “Durability Of Concrete Structures Designs Specifications" (GB 50476-2008), bridges and other critical infrastructure initial chloride ion concentration should be less than 0.08 % (representing the percentage of cementitious materials quality), prestressed structure initial chloride ion content of no more than 0.06% (representing the percentage of gelled material quality), translated into concrete mass ratio, respectively accounting for 0.013% and 0.010%.This calculation, tower, pier, pile the initial chloride ion content of C_0 takes 0.013% (representing concrete mass percentage), box C_0 value takes 0.010% (representing concrete mass percentage).

Durability of a Sea-crossing Bridge engineering Design Examples

A cross-sea bridged engineering design life of 100 years, the preliminary design to determine the tower, pier, pile cap, box girder concrete cover thickness, respectively 50,50,60,45 mm. Towers and the pier is mainly exposed to pressure loads. Taking into account the eccentric may have some tensile stress, the main girder subjected to bending loads and prestressed pressure loads. This article assumes that tower, pier, girder bending strength of the internal stress level of 15%,cap is mainly exposed to compressive stress, consider some eccentric, assuming the flexural stress level of 5%. Depending on the selected parameter by Formula 2 , Formula 3 , Formula 4 life calculated to meet 100a 28d chloride ion diffusion coefficient of concrete control indicators D28, considering the effects of flexural load chloride ion diffusion coefficient of 28d control index for the D28,η, calculation parameters and calculation results are shown in Table 2.

Table 2 Durability design parameter selection and calculation results

Category	Pylon (atmospheric zone)	Pier (splash zone)	CAP (water level fluctuation area)	Box girder (atmospheric zone)
C_s（The percentage of concrete quality%）	0.15	0.15	0.40	0.15
C_{cr}（The percentage of concrete quality%）	0.10	0.05	0.10	0.10
C_0（The percentage of concrete quality%）	0.013	0.013	0.013	0.01
c The protective layer thickness (mm)	50	50	60	45
To Assume that stress level η	15%	15%	5%	15%
$D_{28}(\times10^{-12}m^2/s)$	41.6	7.5	9.2	35.8
$D_{28,\eta}(\times10^{-12}m^2/s)$	32.1	5.8	8.4	27.6

Conclusions

Flexural load increases chloride ion diffusion rate in marine engineering high-performance concrete, the higher the stress level, the greater the chloride ion diffusion coefficient of concrete.

Other parameters under consistent conditions withstand the bending loads and do not withstand loading test diffusion coefficient control relationship between the ratio of indicators D_η/D_0 and stress level η exponentially.

Taking a cross-sea bridge project as an example, select the model parameters, environmental conditions, component parameters, environmental parameters, and so on, the establishment of a "design life-control index of chloride ion diffusion coefficient" correspondence, can provide durability design reference for similar works.

Acknowledgements

This work was financially supported by the State Department of Transportation Science and Technology Project (201132849A1140).

References

[1] Concrete Structure Design and Construction Guide [S]. Beijing : China Building Industry Press,(2004)54-58.
[2] Life-365 Service Life Prediction Model TM and Computer Program for Predicting the Service Life and Life-Cycle Costs of Reinforced Concrete Exposed to Chlorides. January 8, 2008.
[3] DuraCrete, Final Technical Report, The European Union-Brite Euram III, Contract BRPR-CT95-0132, Document BE95-1347/R17, May, 2000.
[4] fib Model Code for Service Life Design, fib Bulletin 34, February 2006.
[5] SUN W, ZHANG Y M,YAN H D,et al. Damage and damage resistance with different strength grade under double damage factors [J]. Cem Conc Comp, 21(1999)439-442.
[6] MEHTA P K. Concrete in the marine environment[M]. [S.l.]: Taylor&Francis Group (1991)5-10.
[7] Wangshengnian. harbour engineering concrete durability technology development and the present situation in China.[J]. Port &Waterway Engineering, 10(2010)1-7.
[8] Sun Wei. loads and environmental structural concrete durability and service life of the coupling [J]. Journal of Southeast University, 11 (36) (2006)7-14.
[9] Jin Weiliang, Yanyongdong, Wang Hailong. transfer in concrete under chloride ions in the load progress [J]. Journal of Portland. 38 (11)(2010) 2218-2224.
[10] Zhang Yitao, Fang Yonghao, Zheng Bo. load and other factors under combined action of durability of concrete progress [J]. Materials Review, 17 (9) (2003)48-50.
[11] Mu Ru . Freeze-thaw cycle and the external bending sStress , salt solution combined with the durability of concrete under life prediction [D]. Nanjing : Southeast University , 2000 .
[12] Guan Yu. Single and life evaluation of high strength concrete under multiple damage factors [D]. Nanjing: Southeast University, 2002
[13] B. Gerard, D. Breysse, A. Ammouche, O. Houdusse, O. Didry. Cracking and permeability of concrete under tension. Mater Struct, 29(1996)185-194
[14] KONIN A, FRANFOIS R,ARLIGUIE G. Penetration of chlorides in relation to the micro-cracking state into reinforced ordinary and high strength concrete[J]. Mater Struct , 31(5) (1998)310-316.
[15] Fang Yonghao, Lee Chi ching, Zhang Yitao. Permeability of concrete under sustained pressure load [J]. Journal of the Chinese Ceramic Society, 33 (10) (2005)1281-1286.
[16] Zhao Shang, Gong Jin-Xin, water Jin feng. Water level fluctuation area subjected to bending load experimental study on chloride diffusion in concrete [J]. China Journal of Highway and Transport, 4(2007).
[17] Zhang Hanbin, Tang Minghan, Zhang Shaojun. Brief introduction of Hangzhou Bay Cross-Sea Bridge project and a number of technical programmes [J]. Prestressing technique, 4 (2006) 32-40.
[18] Wang Jun. research and application of concrete of Zhenjiang-Yangzhou Yangtze River highway bridge [D]. Nanjing: Hehai University, 2005:11-14.
[19] He Shiqin, Gong Jin-Xin. Bending load effect on chloride diffusion in concrete [J]. Journal of building materials, 8 (2) (2005)134-138.
[20] Wang Shengnian, Pan Deqiang. Hong Kong-Zhuhai-Macao Bridge preliminary design and durability of concrete durability assessment test of main engineering topical research reports [R]. Guangzhou, four Institute of aviation engineering limited, 2010.

Applied Mechanics and Materials Vols. 744-746 (2015) pp 65-70
© (2015) Trans Tech Publications, Switzerland
doi:10.4028/www.scientific.net/AMM.744-746.65

Dynamic analysis of concrete frame structure with story-adding steel structure at the top

Xianghong Sun[1, a], Lieping Xie[1,b] and Feng Ji[1,c]

[1]School of Civil Engineering, Chang'an University, Xi'an, Shaanxi, 710061, P.R. China

[a]xianghongsun@163.com, [b]575537551@qq.com, [c]517363502@qq.com

Keywords: RC structure, Story-adding steel structure, Modal analysis, Dynamic analysis.

Abstract. After steel structure was added on top of a concrete frame structure, the mass, stiffness, natural period and damping ratio of the original frame structure has changed significantly. Using finite element software ANSYS and software PKPM respectively, model of the original frame structure and the new structure with story-adding steel structure were built. Furthermore, seismic performance of the three structures was studied. Weak location of the structure was found out. Finally, the main factors were analyzed. Results show that whiplash effect is not obvious when one-story steel structure was added on the top of the original frame structure. Also, seismic performance of the frame structure with two-story steel structures on the top is perfect. Some suggestions are put forward for designing the similar structure.

Introduction

Nowadays, within the development of urban industrialization and commercialization, construction industry has been gradually transformed from the period of larger-scale building to the period of building combined with renovation [1]. Many of the existing buildings have been unable to meet the cultural and material needs with the growing prosperity, and the needs of social development, since their limited function. But, most of those buildings are far from reaching their design reference period, still having the potential to be renovated. Destroying and rebuilding will lead too much of waste, and will be harmful to the environment. However, buildings that have not reached their using life can still meet people's needs, by renovating and adding story-adding. This method has a much practical value for settling some social problems, such as current shortage of land resources and construction waste momentum [2].

The Key Issues of Existing-structure with Story-adding Analysis

Strengthening Design. Before designing the adding-story steel structure of the building, an evaluation of the main load-bearing components and the foot foundation of the structure should be taken. Then, the parts that can't meet the load requirements should be reinforced. During making the strengthening design, the following steps should be conformed. Firstly, the construction situation should be deeply survived. Secondly, the damage and defect of the construction should be professionally analyzed. And then, the degree of the building intact should be looked into. Next, the anti-knock of the construction should be completely identified. The strengthening design scheme should be based on the identification of anti-knock. When maintaining the building, the renovation should be combined with anti-knock strengthening simultaneously. The reinforcement approach should be simple, be easy to practice, be possible to avoid interfering people's life [3, 4].

Whiplash Effect. Whiplash effect is a kind of response which is harmful to the story structure, and will be more obvious on the story-adding structure. The practical experience shows that with the number of added-story increasing, whiplash effect will be more and more obvious, since the stiffness and quality of the steel story structure will have mutations in the adding-story near the floor; the vibration acceleration of the structure with adding-story structure will be higher than the original structure. For the structure with adding-story on the top of the original structure, the difference vibration cycle between the original structure and the adding-story structure will cause relatively obvious local vibration, and whiplash effect will be generated [5].

Example Analysis

Original Structure. The office building located in a Xi'an's middle school is a five-story reinforced concrete frame structure, cast-in-situ. The building was constructed in the 1990s, 5 stories, the upper height 3.6 meters. The standard plane layout is shown in Fig.1.

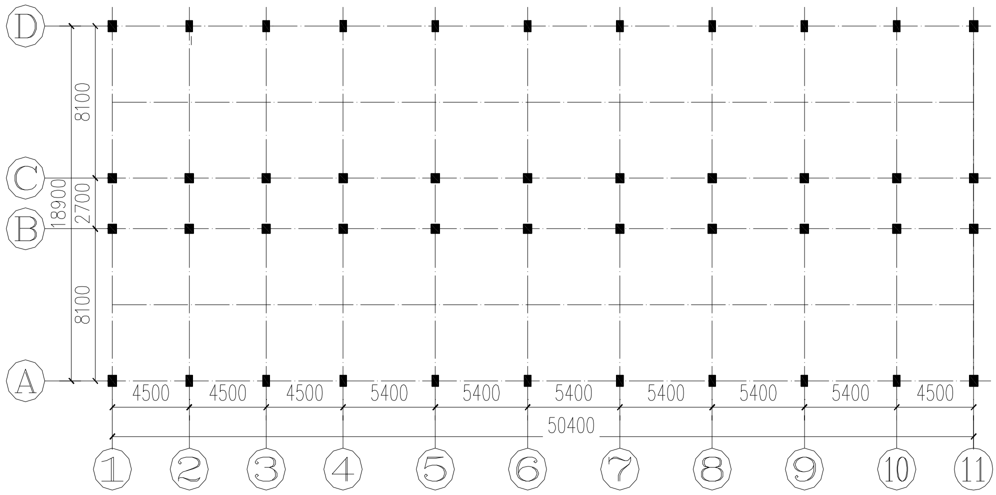

Fig.1 Standard plane layout

For the using requirement, the structure needs to add steel structure on the top. The height of the adding-story steel structure is 3.6m. The wall of the adding-story steel structure is selected the composite panels. Floor of the adding-story steel structure is the reinforced concrete slab which is made in site. The roof of the adding-story structure is colorful-steel composite panels with 85mm width. And the adding-story's beams and column should choose the weld I-shaped steel. The component sections are shown in Table 1.

Table 1 Component section

Sectional size of beam-column for original structure		Sectional size of beam-column for adding-story steel structure	
component	Sectional size[mm]	component	Sectional size[mm]
Z1	500×550	Z1	400×400×10×14
Z2	500×600	Z2	400×500×10×14
L1	300×700	L1	300×650×10×14
L2	300×500	L2	250×500×10×12

Analysis Using PKPM. The original structure is a five-story reinforced concrete frame structure, and the adding-story structure is steel structure. However, it's lack of current design code to reference. Therefore, when designing the adding-story steel structure, the selection of most related parameters should be rigorous argued. The selection of the damping parameters should be chosen by the material of main stress components, and selecting the damping parameters for the overall structure. The damping coefficient of the reinforced concrete composite structure is 0.05, the damping coefficient of the steel structure is 0.02, and the damping coefficient is determined 0.04 according to the engineering experience value.

As a powerful tool for dynamic analysis, ANSYS is a good way for three dimensional finite element simulations. And combining with the original structure, the refinement is in a high degree. To verify the correctness of the ANSYS modeling, software PKPM should be used for structure design and analysis firstly. It could provide a test for the subsequent ANSYS modeling, too. Using software PKPM to conduct the integral calculation for the structure with 5-story original structure adding

2-story steel structure (abbreviated for 5+2 structure), using SATWE analyze the new structure. Structural model was analyzed to obtain the vibration period of the model, and to extract first 8-order formation using software SATWE. The translational coefficient of (X+Y) direction and the reverse coefficient are shown in Table 2.

Table 2 Period, Translational coefficient and Reverse coefficient

Mode of vibration	Period	Translational coefficient (X+Y)	Reverse coefficient
1	1.162	1.00 (0.99+0.01)	0.00
2	1.095	0.98 (0.01+0.97)	0.02
3	1.030	0.03 (0.00+0.03)	0.97
4	0.589	1.00 (1.00+0.00)	0.00
5	0.441	0.95 (0.00+0.95)	0.05
6	0.407	0.05 (0.00+0.05)	0.95
7	0.316	1.00 (1.00+0.00)	0.00
8	0.278	0.88 (0.00+0.88)	0.12

It can be seen from analysis data in table 2 that the first vibration mode of the structure is the translation of X direction, the second vibration mode is the translation of Y direction, and the third mode is reverse. The translational and reverse coefficient of the first, second and third vibration mode are close to 1. It shows that the structural layout is rational, and the center of mass and centroid are close. The ratio of the first period to the third mode period is 0.886, which is less than the specification requirement of -0.9. The effective mass coefficient of the first vibration mode is 98.09%, and the effective mass coefficient of the second vibration mode is 97.70%. Both of them meet the requirements of specification. The correctness of the structural modeling is verified.

Analysis of The Finite Element Model. After adding the steel structure story on the top of reinforced concrete frame structure, dynamic performance of the original structure will face a great change, since the stiffness of the entire structure which distributed along the height direction will become very uneven after adding-story steel structure. Dynamic performance of the adding-story was analyzed by using software ANSYS. In this paper we assume that the steel columns and the beam, and column foot of the adding-story steel structure are made as rigid connection, the floor slab is rigid, and the in-plane stiffness is infinite, ignoring the out-of-plane stiffness.

Linear element BEAM188 are choosing for the frame beams and columns of the structure, and shell element SHELL63 is choosed for the floor of the structures. In modal analysis, steel and concrete are considered to be elastic material. It is defined by the Poisson's ratio, elastic modulus and density [6]. Unit grid division is maped by mapping grid, and the underlying nodes are consolidated in this model, no processing for other nodes. Using the command stream or GUI operation to complete the establishment of the model. According to the research, the subspace method is choosed to analyse the model structure, since it could ensures the accuracy of the calculation results and the computation speed.

To verify the correctness of the structural model, the extracted results of the cycle and the story drift should be compared with that of ANSYS. The results are shown in Table 3 and Table 4, and the results of the contrastion are shown in Fig.2 and Fig.3.

Table 3 Vibration period by SATWE and ANSYS

Mode of vibration		1	2	3	4	5	6	7	8
Period[s]	SATWE	1.162	1.095	1.030	0.589	0.441	0.407	0.346	0.288
	ANSYS	0.980	0.942	0.843	0.481	0.328	0.296	0.281	0.246

Table 4 Story drift by SATWE and ANSYS

Storey number		1	2	3	4	5	6	7
Story drift	SATWE	1/1782	1/1332	1/1412	1/1561	1/1701	1/1319	1/1580
	ANSYS	1/1694	1/1202	1/1265	1/1468	1/1639	1/1396	1/1655

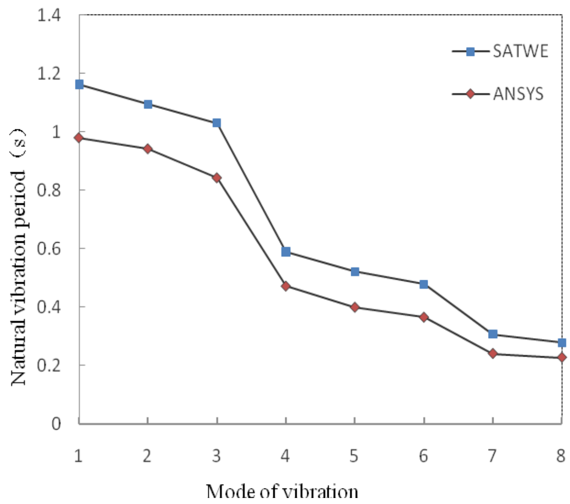

Fig. 2 Structure vibration period

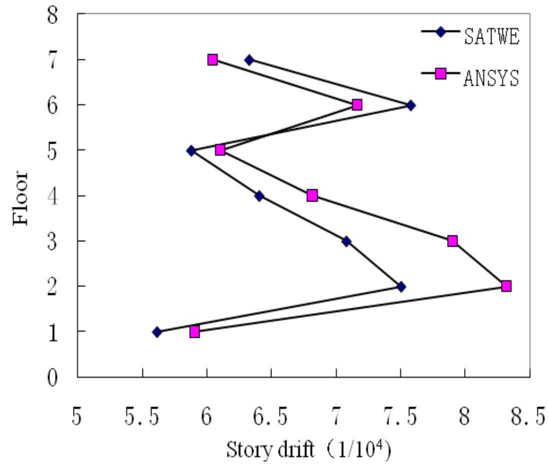

Fig. 3 Story drift

Comparing the results of structure vibration period between SATWE and ANSYS, It can be found that the difference between the numerical results are not obvious, and the trend of changes is basically identical. It can be said that the results of the the model and the analysis are correct. The results can be used as foundation for the further finite element dynamic analysis, too.

Influence of the Numberof Adding-story to the Original Structural Stress. the method of direct story-adding adopting the steel structure should not be used to anlyze new structure with too much storys, since the great influence of the weak story between the two kinds of structures. On the basis of the 5-story original structure, 1-story, 2-story, 3-story and 4-story steel structure are added on the top of the original structure, respectively. And then, modeling and analys of each kind of structures are carried out using software ANSYS. First 8-order modal vibration form are extracted, respectively. The natural vibration period of the order modal form one to eight is shown in Fig.4. The results of the story drift under five condition are shown in Fig.5.

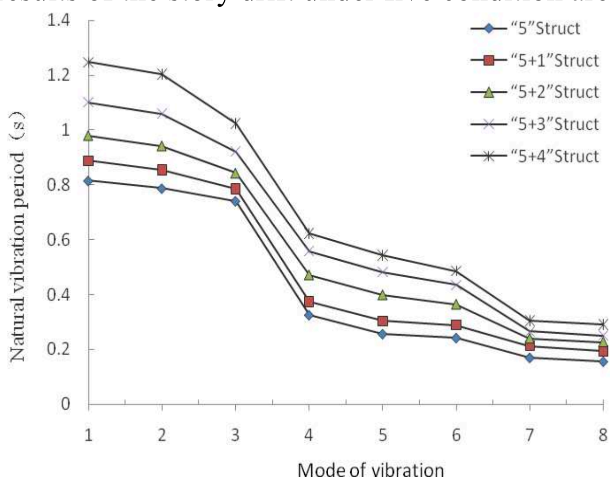

Fig. 4 Comparison diagram of natural vibration period

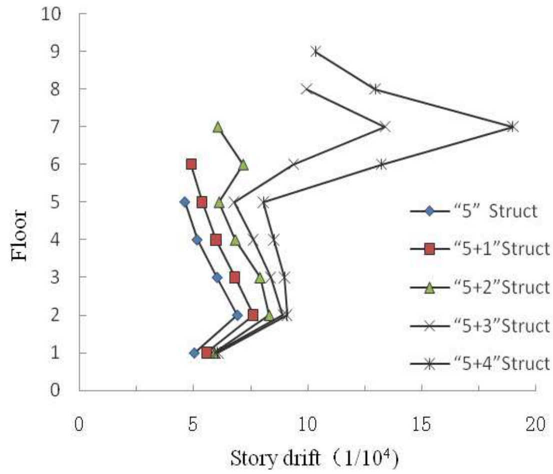

Fig. 5 Comparison diagram of Story drift

It can be seen from Fig.4 and Fig.5, with the increasing of the storys number of the adding steel structure, the flexibility of the structure will become larger, and with the increasing of the natural vibration period, the maximum story drift will become larger, too. In the structure of "5 + 1", the story drift in the adding-story steel structure has no obvious change, but it is find that the story drift of the structure of "5 + 2" will increase significantly. With the increasing of number of the adding-story steel structure, the displacement value will be more and more significant. It shows that whiplash effect in the structures that have only one adding-story structure will be not obvious. But if the structures have more than 2 story steel structure added, the whiplash effect will be more and more obvious with the number of adding-story structure increasing. The analysis results of the story drift of the five kinds structure in Fig.5 show that: In the structure of "5 + 4", the story drift occurs in 7th floor with 1/526. It is larger than the specification requirement 1/550, which does not meet the requirement of seismic deformation. Therefore, the maximum number of adding-story on the top of the original structure is 3 for this structure.

It can be found from the Fig.5 that story drift of the five kinds of structure are increased sharply in the second floor. It shows that the second floor of the original structure is the weak story. So some measures should be taken for strengthening the second story.

Influence of The original Structure. The whiplash effect usually becomes more and more significant with the increasing of the structural height. When using the method of direct story-adding steel structure, since the weight of the steel structure is lighter than that of the original reinforced concrete structure, the effect will be more significant. To analyze the influence of different original structural height, a two-story steel structure is chosen. The original structure component sectional size and other conditions are the same. Original structures are chosen as 2-story, 3-story, 4-story, and 5-story respectively. Thus, the five structure are the structure of "2 + 2", the structure of "2 + 3", the structure of "2 + 4" and the structure of "2 + 5", as shown in Fig.6 and Fig.7.

For the structure of "2 + 2", the structure of "3 + 2", the structure of "4 + 2" and the structure of "5 + 2", the natural vibration period from the first to eight order modal are extracted, as shown in Fig.6. Then, the response spectrum analysis is made. The results of the story drift are shown in Fig.7.

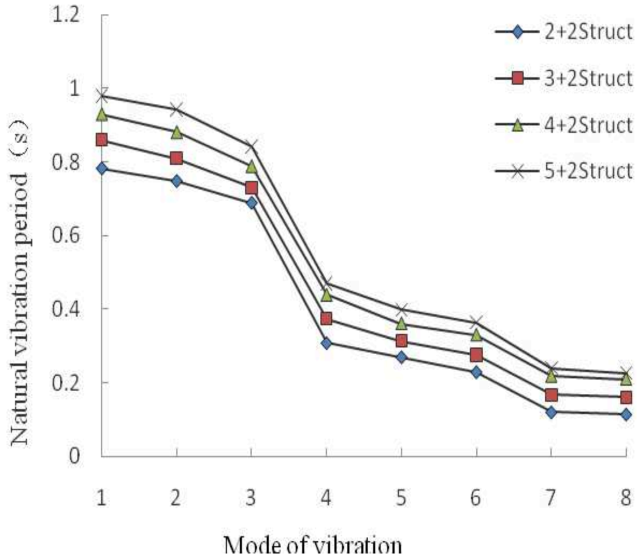

Fig. 6 Natural vibration period of four structures

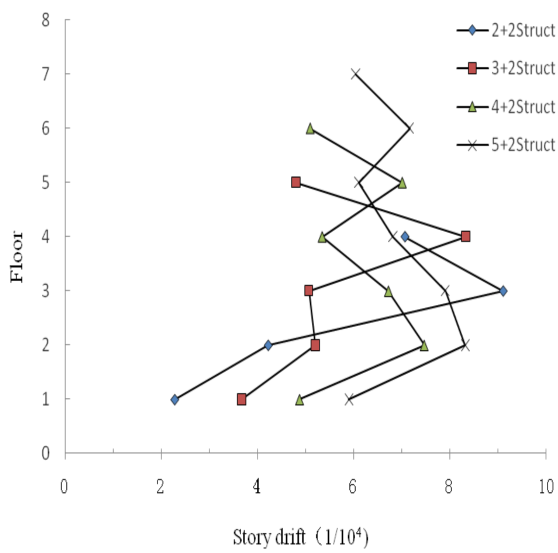

Fig. 7 Comparison diagram of Story drift

It can be found from Fig.6 that with the decreasing story number of the original structure, the whole structural stiffness will increase when the number of adding-story steel structure is constant. It is similar to the general frame structure. From the distribution of the four kinds of structural story drift, it can be seen that the four kinds of structural story drift sharply increase in the adding-story and the second story. In the structure of "2 + 2", the phenomenon in the second story is more obvious. The reasons of the phenomenon are analyzed. Firstly, the second story is the weak story of the original structure. Secondly, the structure of "2 + 2" is the least kind of adding-story structure in several primary structures. Thirdly, the height of the adding-story steel structure is equal to the height of the original structure, so the whiplash effect is significant. So, it is wrong that the few the original structural story is, the better its performance will be. Especially, when the height of the adding-story steel structure is equal to or even greater than that of the original structure, we should attach great importance to the earthquake energy concentrates in the structural transformation location.

Conclusions

The office building that built in a Xi'an's middle school is chosen as the research object, using the finite element analysis software ANSYS and PKPM, the reinforced concrete frame structure with adding-story steel structure are analyzed. The following conclusions are obtained.

As the number of the adding-story increases, whiplash effect will be more and more serious, and the maximum story drift will be larger. The second floor of the original structure is the weak story. It is necessary to analyze the dynamic characteristics of the structure to find out the weak parts and take reinforcement before designing the adding-story steel structure. The maximum number of the adding-story steel structure for the original 5-story reinforced concrete structure is 3. When the number story-added are more than 3, it needs to take some measures to strengthen the weak positions, like adding some energy dissipation bracing or dampers.

For the method of direct story-adding to the steel structure, the number of story-added is 2. In a certain range, the larger the number of the original structural story is, the weaker the whiplash effect in adding-part will be. And the story drift in adding-part will be smaller, too. When designing the adding-story steel structure, the height of adding-story steel structure should not be higher than that of the original structure.

References

[1] Tao Zhang, D. Integral Design and Seismic Resistant Property Analysis of the Adding Steel Stories on the Top of the Original Buildings. Beijing, Tsinghua University (2004). In Chinese

[2] Tian Luo, D. Seismic Analysis and Study on Structures with Light-steel-frame Additional Constructed on It. Hefei: Hefei University of Technology (2005). In Chinese

[3] Jianping GAO, A Review of Story-adding and Upgrading for Existing Building Structures in China and Abroad [A]. Journal of East China Jiao tong University (2006). 23(2):3-4. In Chinese

[4] Institute of Seismic Strengthening. Seismic strengthening of reinforced concrete structures technology [M]. Beijing: China Building Industry Press (2010)

[5] D. Kakaletsis, J.k. Comparison of CFRP and Alternative Seismic Retrofitting Techniques for Bare and Infilled RC Frames J. Compos. Constr (2011). 15:565-577.

[6] Xinmin Wang. ANSYS Structural analysis unit and apply [M]. Beijing: China Communications Press (2011). In Chinese

Applied Mechanics and Materials Vols. 744-746 (2015) pp 71-77
© (2015) Trans Tech Publications, Switzerland
doi:10.4028/www.scientific.net/AMM.744-746.71

Dynamic nonlinear analysis of semi-rigid steel frames based on the Finite Particle Method

YU Ying[a], JIN Lin[b] and XIA Ping[c]

Department of Civil Engineering of Shantou University, Shantou, Guangdong 515063, China;

[a]yuying@stu.edu.cn, [b]13ljin@stu.edu.cn, [c]s_xiaping@stu.edu.cn

Keywords: Finite Particle Method (FPM), semi-rigid steel frame, nonlinear spring model, dynamic nonlinear analysis.

Abstract. The Finite Particle Method (FPM), based on the Vector Mechanics, is a new structural analysis method. This paper explores the possibility of the proposed method being applied in the dynamic nonlinear analysis of semi-rigid steel frames. Taking the two dimensional beam element as an example, the formulations of the FPM to calculate the dynamic and geometric nonlinear problems are derived. Spring model with zero-length is adopted to simulate the relationship between internal forces and deformations of the semi-rigid steel connections. The nonlinear strengthen spring model is used to analyze the nonlinear behavior of the semi-rigid connection. Explicit time integrations are used to solve equilibrium equations. Comparing to traditional Finite Element Method, iterations and special modifications are not needed during the dynamic nonlinear analysis, which is more advantageous in structural complex behavior analysis. Two numerical examples are presented to analyze the behaviors of rigid and semi-rigid steel frames, and behaviors of linear and nonlinear semi-rigid connections, which demonstrate the accuracy and applicability of this method in dynamic nonlinear analysis.

Introduction

Beam-to-column joints of steel frames are usually assumed to be rigid or pinned connections in structural design. This assumption causes an inaccurate estimation of the response of frames since real beam-to-column joints are between fully rigid and pinned connections [1]. Mathematic models for semi-rigid connections could be grouped into two categories: linear semi-rigid connection models and nonlinear semi-rigid connection models. In linear semi-rigid connection models, the stiffness of connections is assumed to be constant. This model can be simply implemented without consideration of the nonlinear behavior of semi-rigid connections [2]. In nonlinear semi-rigid connection models [3], the stiffness of connections varies corresponding to different loading magnitudes and therefore these models can accurately capture the moment-rotation relationship as well as consider the energy dissipation.

The Finite Particle Method (FPM), based on the Vector Mechanics [4], is a new structural analysis method, which has been successfully applied to structural dynamic buckling analysis [5], deployable structures analysis [6], and progressive failure analysis of structures [7].The objective of this study is to extend the application of the FPM to the dynamic nonlinear analysis of semi-rigid steel frames. The formulations of two dimensional beam elements to calculate the dynamic and geometric nonlinear problems are derived. Spring model with zero-length is adopted to simulate the relationship between internal forces and deformations of the semi-rigid steel connections. The nonlinear strengthen spring model is used to analyze the nonlinear behavior of the semi-rigid connection. Two numerical examples are presented to demonstrate the accuracy and applicability of this method in dynamic nonlinear analysis.

Fundamentals of the FPM

The FPM models the analyzed domain to be composed by finite particles, as shown in Fig.1. The structural mass is assumed to be represented by each particle. Particles in the structure are connected by elements. Elements have no mass. Thus, they are in static equilibrium. The deformations of elements can represent the force relationship and position variations between particles.

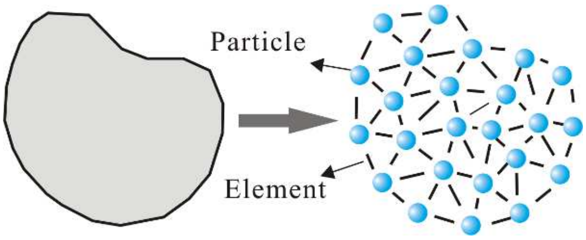

Fig.1 FPM model of an analysis domain

Regarding the particle α connected to a 2D beam element, the motion variables of the particle can be decomposed to two translations and one rotation, which are corresponding to two forces and one moment. Motions of all particles in the discrete model follow Newton's second law,

$$\mathrm{m}_\alpha \ddot{\mathrm{d}}_\alpha = \mathrm{F}_\alpha^{\mathrm{ext}} - \mathrm{F}_\alpha^{\mathrm{int}}. \tag{1}$$

where m_α is the mass value, including the nodal mass and the equivalent mass of elements connected to the particle; $\ddot{\mathrm{d}}_\alpha$ is the displacement vector of particle α; $\mathrm{F}_\alpha^{\mathrm{ext}}$ and $\mathrm{F}_\alpha^{\mathrm{int}}$ are the external force vector and internal force vector of particle α, respectively.

Fictitious motion is used to calculate pure elemental deformations in the FPM. Taking a 2D beam element shown in Fig. 2 as an example, the position vectors of Element 12 at time t_a and t_b ($t_a+\Delta t$) are ($\mathrm{x}_1^{\mathrm{a}}$, $\mathrm{x}_2^{\mathrm{a}}$) and ($\mathrm{x}_1^{\mathrm{b}}$, $\mathrm{x}_2^{\mathrm{b}}$), the rotation vectors are (θ_1^{a}, θ_2^{a}) and (θ_1^{b}, θ_2^{b}), as shown in Fig. 2(a). If taking the element at time t_a as the reference configuration, the relative displacement of node 1 and 2 are $d\mathrm{x}_1= \mathrm{x}_1^{\mathrm{b}}- \mathrm{x}_1^{\mathrm{a}}$, $d\mathrm{x}_2= \mathrm{x}_2^{\mathrm{b}}- \mathrm{x}_2^{\mathrm{a}}$, $d\theta_1=\theta_1^{\mathrm{b}}-\theta_1^{\mathrm{a}}$, and $d\theta_2=\theta_2^{\mathrm{b}}-\theta_2^{\mathrm{a}}$, as shown in Fig. 2(b).

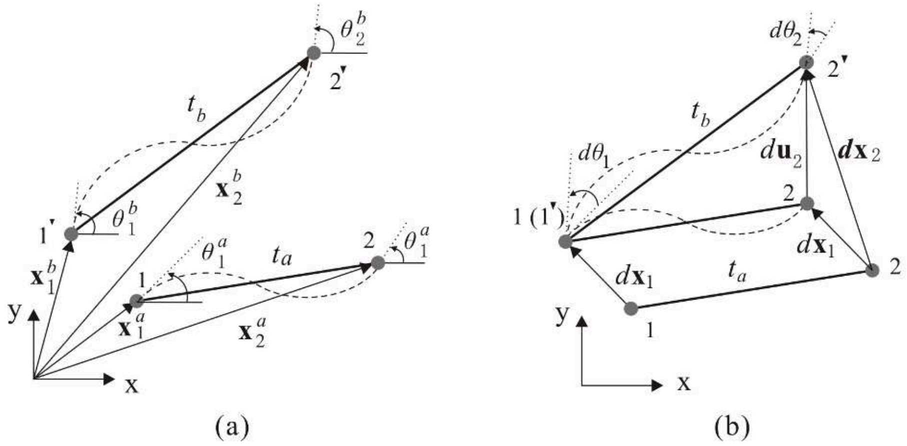

Fig. 2 Element 12 (a) elemental displacement; (b) elemental relative displacement

Let the element 1′2′ experience a fictitious translation $-\mathrm{dx}_1$ and a fictious rotation $-\Delta\theta$ to element 1″2″. Thus the rigid body motion is removed from the nodal displacement. The pure deformation of element 12 includes axial deformation Δ, two rotations θ_1 and θ_2, can be obtained at the virual configuration. According to the principle of virtual work, the incremental internal force and moment can be expressed as

$$\begin{Bmatrix} \Delta f_{2x} \\ \Delta m_{1z} \\ \Delta m_{2z} \end{Bmatrix} = \frac{E_a}{l_{1''2''}} \begin{bmatrix} A_a & 0 & 0 \\ 0 & 4I_a & 2I_a \\ 0 & 2I_a & 4I_a \end{bmatrix} \begin{Bmatrix} \Delta \\ \theta_1 \\ \theta_2 \end{Bmatrix} \tag{2}$$

where, E_a is the Young's modulus; A_a is the cross section area of element 12; I_a is the moment of inertia. The other three internal force f_{1x}, f_{1y} and f_{2y} can be obtained from the elemental balance equations. After evaluating internal forces at this configuration, the element was moved back to the original position by a forward motion. Particle internal forces can be calculated by summing the elemental internal forces connected to corresponding particles [7].

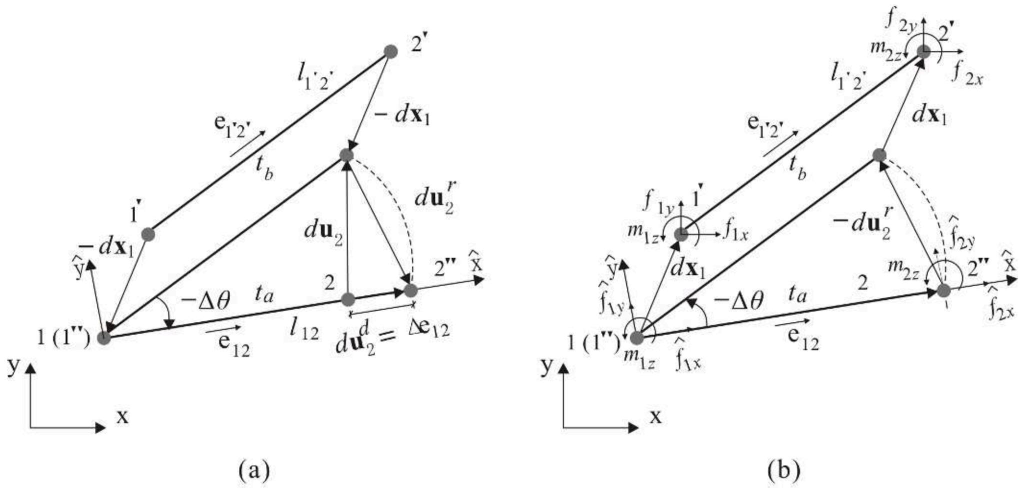

Fig.3 Fictitious motion (a) fictitious reverse motion; (b) fictitious forward motion

Semi-rigid connection calculation

Semi-rigid connection model. A zero-length spring element is used here [8]. See a semi-rigid beam-column joint C in Fig.4. It contains two particles A and B, which share the same coordinate, half of the mass and moment of inertia with joint C. The elemental mass and length between particle A and B are equal to zero. The relative rotation between A and B is restricted by the spring. The relation between the incremental force and rotation of the spring element is as follows:

$$\Delta m = k_{AB}\theta_r \qquad (3)$$

where, Δm is the restricted moment, k_{AB} is the stiffness of the semi-rigid spring, θ_r is the relative rotation between particle A and B, which equal to the difference of rotation displacements of particle A and B. The rotation of joint C is represented by particle A and B. However, the vertical and horizontal displacement of joints should be modified. Using the summation of the internal force of paticle A and B, the translation displacement of joint C is recalculated.

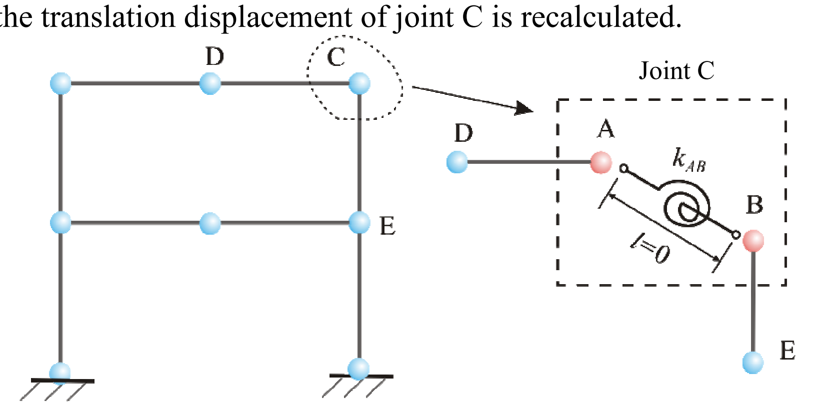

Fig.4 Zero length spring element for semi-rigid connection

Nonlinear spring model. In this paper, the Richard-Abbott four-parameter model [9] is used to evaluate the nonlinear behavior of semi-rigid connections. The independent hardening model is used to predict the cyclic behavior. The moment-rotation relationship of the connection is defined by

$$M=\frac{(R_{ki}-R_{kp})\left|\theta_r\right|}{\left\{1+\left|\frac{(R_{ki}-R_{kp})\left|\theta_r\right|}{M_0}\right|^n\right\}^{\frac{1}{n}}}+R_{kp}\left|\theta_r\right| \tag{4}$$

where M and θ_r are the moment and the rotation of the connection, n is the parameter defining the shape, R_{ki} is the initial connection stiffness, R_{kp} is the strain-hardening stiffness and M_0 is the reference moment.

Numerical examples

A single-bay two-story frame. The geometry and loading of the frame are given in Fig. 5. All the frame members are W8×48 with Young's modulus E of 205×10^6kN/m^2. An initial geometric imperfection ψ of 1/438 is considered. The vertical static loads are applied on the frame to consider the second-order effects followed by the horizontal forces applied suddenly at each floor during 0.5 s, as shown in Fig. 5. The material is assumed to be elastic throughout the analysis, and the viscous damping is ignored. The four parameters of the Richard-Abbott model are: R_{ki} = 23,000kN·m/rad, R_{kp} =70kN·m/rad, M_0=180kN·m, and n=1.6.The time-displacement responses at the second floor predicted by the proposed analysis for the rigid, linear semi-rigid, and nonlinear semi-rigid frames match well with those of Nguyen [8], as shown in Fig. 6.

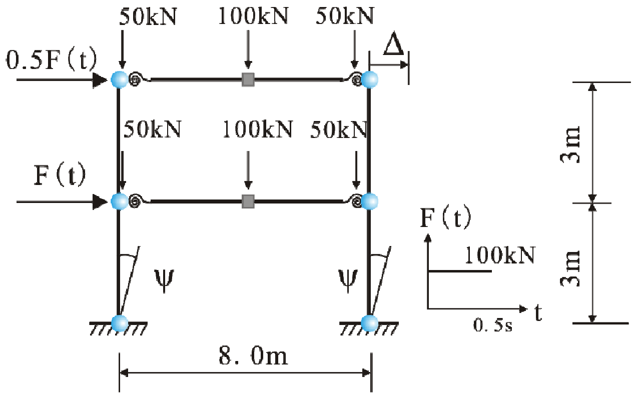

Fig.5 Geometry and load of a single-bay two-story frame

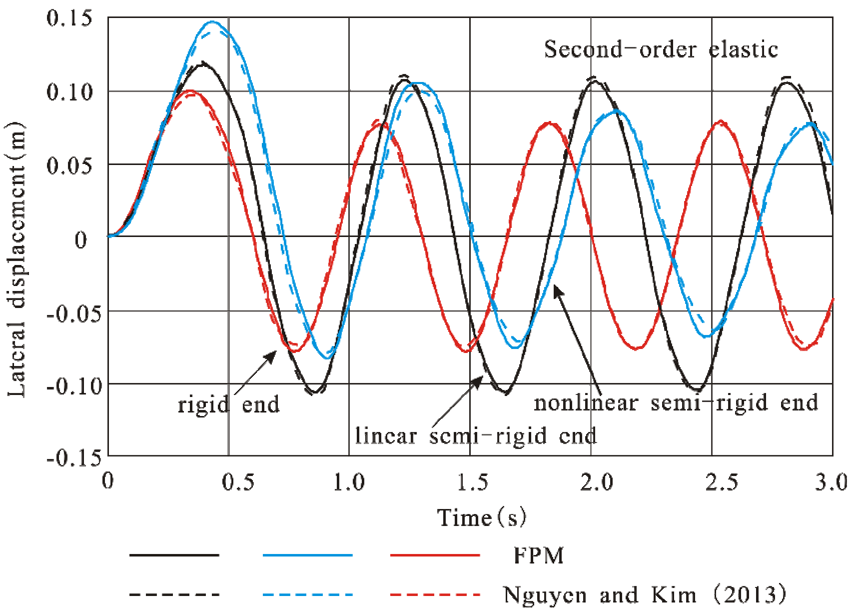

Fig.6 Time-displacement response at position Δ of a single-bay two-story frame

Vogel six-story steel frame. A Vogel six-story frame is shown in Fig.7. An initial geometric imperfection ψ of 1/450 was considered for the column members. Young's modulus was

205×10^6kN/m^2. The static loads distributed on beams of 31.7 and 49.1kN/m^2 were converted to lumped masses at the nodal points. The parameters of the Richard-Abbott model are: R_{ki} = 12,336.86kN·m/rad; R_{kp} = 112.97kN·m/rad; M_0 = 96.03kN·m; n = 1.6. The time-displacement responses at the position Δ predicted by the FPM for the rigid, linear semi-rigid and nonlinear semi-rigid frames match well with those of Nguyen [8], as shown in Fig. 8. The hysteresis loops at connection C in Fig.9 shows the energy dissipation induced by the hysteretic damping of nonlinear connections, because the envelope size of the moment-rotation curve is getting smaller.

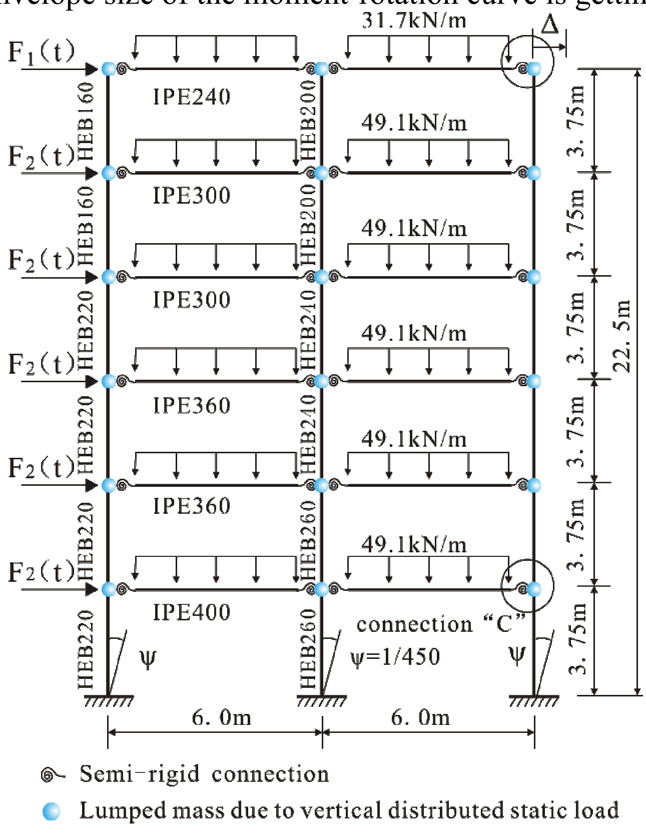

Fig.7 Geometry and load of a Vogel six-story steel frame

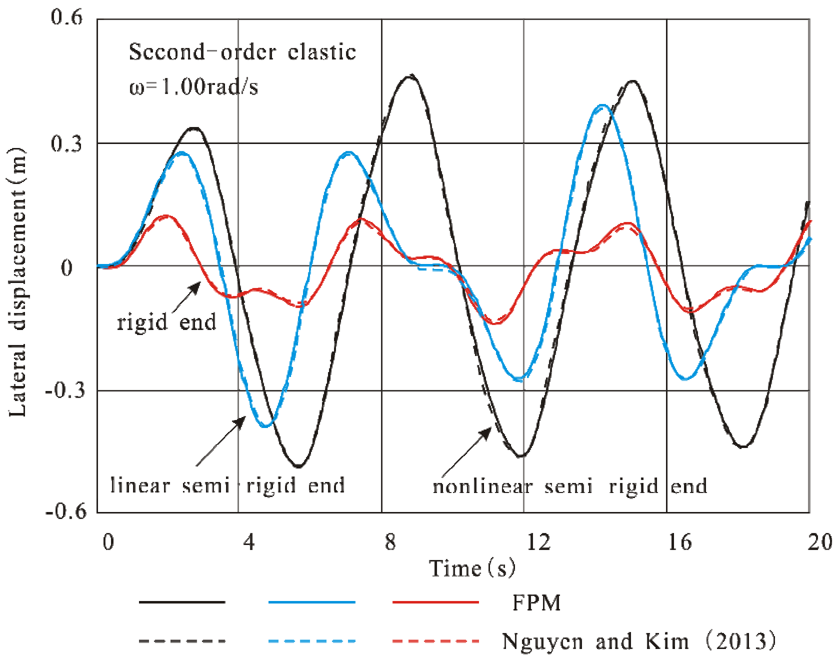

Fig.8 Time-displacement response of a Vogel six-story steel frame

Summary

This paper explores the possibility of the proposed method being applied in the dynamic nonlinear analysis of semi-rigid steel frames. Fundamentals of the FPM are presented. Using the zero-length spring model and Richard-Abbott nonlinear semi-rigid model, the rigid, linear semi-rigid and nonlinear semi-rigid frames are investigated in the present analysis. Two numerical examples are presented to demonstrate the accuracy and applicability of this method in dynamic nonlinear analysis of steel frames.

Acknowledgements

This work was financially supported by the National Natural Science Foundation of China (No.51108257), the Natural Science Foundation of Guangdong, China (2011040004173), Doctoral Program of the ministry of education China (20114402120001), Initial research founding of Shantou University (NTF10025) and Foundation for Distinguished Young Talents in Higher Education of Guangdong, China (LYM11065).

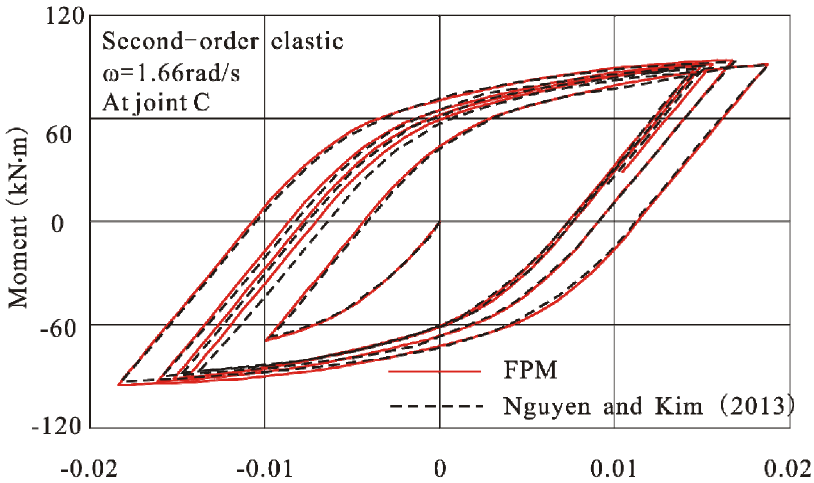

Fig.9 Hysteresis loops of the Vogel frame at connection C

References

[1] Liew JYR, Yu CH, Ng YH, Shanmugam NE. Testing of semi-rigid unbraced frames for calibration of second-order inelastic analysis. J Constr Steel Res, 1997, Vol. 41:159–95.

[2] Xu L. The buckling loads of unbraced PR frames under non-proportional loading. J Constr Steel Res, 2002, Vol. 58: 443–65.

[3] Lui EM, Chen WF. Analysis and behavior of flexibly-jointed frames. Eng Struct, 1986, Vol. 8:107–18.

[4] Ting E.C., Shih C., Wang Y.K.. Fundamentals of a vector form intrinsic finite element: Part I. Basic procedure and a plane frame element. Journal of Mechanics, 2004, Vol. 20(2): 113-122.

[5] Ying Yu, Xiaohua Zhao, Yaozhi Luo. Multi-snap-through and dynamic fracture based on Finite Particle Method. Journal of Constructional Steel Research 82 (2013) 142–152.

[6] Ying Yu, Yaozhi Luo. Motion analysis of deployable structures based on the rod hinge element by the finite particle method. Proc. IMechE Part G: J. Aerospace Engineering. 2009, 223(7): 955-964.

[7] Ying Yu, G. H. Paulino, and Y. Luo. Finite particle method for progressive failure simulation of truss structures, Journal of Structural Engineering ASCE, 2011, 137(10): 1168-1181.

[8] Phu-Cuong Nguyen, Seung-Eock Kim. Nonlinear elastic dynamic analysis of space steel frames with semi-rigid connections. Journal of Constructional Steel Research, 2013, Vol. 84:72 – 81.

[9] Richard RM, Abbott BJ. Versatile elastic-plastic stress – strain formula. J Eng Mech. Div ASCE, 1975, Vol. 101:511 – 5.

Applied Mechanics and Materials Vols. 744-746 (2015) pp 78-81

doi:10.4028/www.scientific.net/AMM.744-746.78

Effects of Silica Fume on Concrete Compressive Strength

Huaxi LI*

College of Civil and Transportation Engineering, Hohai University, Nanjing 210098, China

lhxrick@hotmail.com

Keywords: silica fume, concrete, compressive strength

Abstract. The effects of silica fume (SF) on compressive strength of concrete have been analyzed. The compressive strength results of concrete mixed over different water–binder ratios as well as different replacing percentages of SF were analyzed. The results of the experiments showed that when the polymer/binder materials ratio increases, the compressive strength of concrete decreases. A mathematical model has been proposed for evaluating the strength of concrete containing SF. The proposed model provides a probability to analyze compressive strength based on the time of curing in water (t), water to binder materials ratios and SF to binder materials ratios which are shown as (w/b) and (s). This model might serve as a useful guide for increasing concrete compressive strength.

Introduction

Many factors affect the compressive strength of concrete, such as cement composition and fineness, water-to-cement ratio, aggregate, age and temperature of curing. Abrams' water–cement ratio law in 1918 is still considered as a milestone in the history of concrete technology, it is accepted that the largest single factor that governs the strength of concrete is the water to cement ratio. Originally, concrete was made by mixing cement, aggregates and water, and use of admixtures was unknown, and the only cementation material was cement. The present-day, new-generation concretes contain mineral admixtures and latexes for a variety of reasons. These materials increase abrasion strength or durability and decrease permeability, and Abrams' formulation needs to be modified or the validity of this relationship for concrete with supplementary materials (silica fume, etc.) should be investigated. The more knowledge be available about the concrete composition versus strength relationship, the better the nature of concrete is understood and how to optimize the concrete mixture.

Silica fume reduces the workability of fresh concrete due to its very specific surface area. It improves a lot of properties of hardened concrete [1]. Some researchers have indicated that there is a great potential usage of SF in the increase in the performance of the concrete properties.

There are two different ways of adding polymers to cement composites that have been described:

(1) Keeping the water-to-cement ratio (w/c) constant to obtain a similar hydration of the cement paste.

(2) Fitting the consistency of the composite, by adjusting the w/c.

In this research, the water to binder ratio is constant and the effects of SF on fluidity and compressive strength of concrete are investigated and a relationship between compressive strength of concrete with the ratios of polymer, SF, water to binder materials and time of curing in water is proposed.

Experimental Work

2.1 Properties of Materials

The materials used in this research were: ordinary Portland cement and SF.

Coarse aggregate with a maximum particle size of 17 mm and fine aggregate with a 3.01 finesse modulus were used in the experiment. The specific gravity and water absorption of coarse aggregates and fine aggregates were 2.55 and 1.6 %, 2.25 and 2.4 %, respectively. A water reducer agent was used to adjust the workability of the concrete mixtures.

2.2 Testing Program and Procedure

In this research, $40\times40\times160$ mm^3 cubes were cast for compressive strength test. Before casting, coarse aggregate, sand and mixture of water and SF were mixed first. Then, cement and rest water together with superplasticizer were put in the mixer and completely mixed.

The mixed concrete was cast in molds to make specimens, and compacted by mechanical vibration. The specimens were demoded after 1 day. Compressive strength of specimens was measured at three mixed curing systems:

(1) 7 days immersed in 20 ± 2 °C water and then cured in air at 20 ± 2 °C with 20 ± 10% of relative humidity for 50 days.

(2) 14 days immersed in 20 ± 2 °C water and then cured in air at 20 ± 2 °C with 20 ± 10% of relative humidity for 40 days.

(3) 28 days immersed in 20 ± 2 °C water and then cured in air at 20 ± 2 °C with 20 ± 10% of relative humidity for 30 days.

Cement hydration process is retarded by the polymer and surfactants. This is visible especially in the compressive strength [2].

The cement hydration and polymer film in the modified concretes develop with prolongation cured age, which results in enhanced strength. The slope of increasing of polymer-modified concrete compressive strength declines from 28 to 90 days [3].

Also, combination of wet and dry curing is effective for the strength development of the polymer-modified concretes. A co-matrix is formed by both processes [4].

The compressive strength was determined according to BS standard 1881. The loading rate was 0.3 MPa/s.

Test Results and Discussion

3.1 Effects of SF on Fluidity of Concrete

Silica fume decreases the fluidity of concrete. This is because SF reacts with water to form hydrates, which would polymerize. The process leads to the increase of molecular volume and the increasing resistance of slurry laminar flow, resulting in an increase in viscosity of concrete.

3.2 Effects of SF on Compressive Strength

A significant improvement in compressive strength of concrete is observed because of the high pozzolanic activity and void filling ability of SF. The chemical phase consists of the pozzolanic reaction that transforms the weak calcium hydroxide crystals into the strong calcium silicate hydrate gel. The results of these actions of SF provide significant improvements in compressive strength [5]. The compressive strength of SF concrete continuously is increased with respect to reference concrete and reached a maximum value of 7.5 % replacement level.

When the ratio of polymer/binder is certain, the amount of SF affects strength of concrete. The percentage of SF that optimizes compressive strength remains 7.5 %.

In a few samples, a local decrease in compressive strength is observed in 5 % polymer. In making of these samples percentage of superplastysizer in 0 and 5% polymer were constantly considered. The cavitations of superplastysizer induce a decrease in compressive strength of these samples.

Mathematical Model

The results obtained from the experiment can be shown by a mathematical model. The primary factors that affected the compressive strength of concrete are the ratios of water, SF to binder materials and time of curing in water. In modeling, effect of superplastysizer on compressive strength is neglected.

Relationship compressive strength with main effective factors can be determined by regression. Before regression it needs to determine how each factor influence in compressive strength.

As the classical formulation of Abrams' law, there exists an inverse relationship between the compressive strength and water to cement ratio of concrete [6]. Abram's equation can be shown as:

$$f = \frac{A}{B^{(\frac{w}{c})}} \tag{1}$$

where A, B are constant coefficients and $(\frac{w}{c})$ is the ratio of water to cement.

A lot of researchers introduced relationship between compressive strength and time of curing in water with a logarithmic equation:

$$f = a \times \log(t) + b \tag{2}$$

where a, b are constant coefficients.

When the percentage of replacement of SF is less than 10, the relationship between compressive strength and SF can be considered with a parabola curve. In Fig. 1 and Fig. 2, relationship between the compressive strength with each factor is determined.

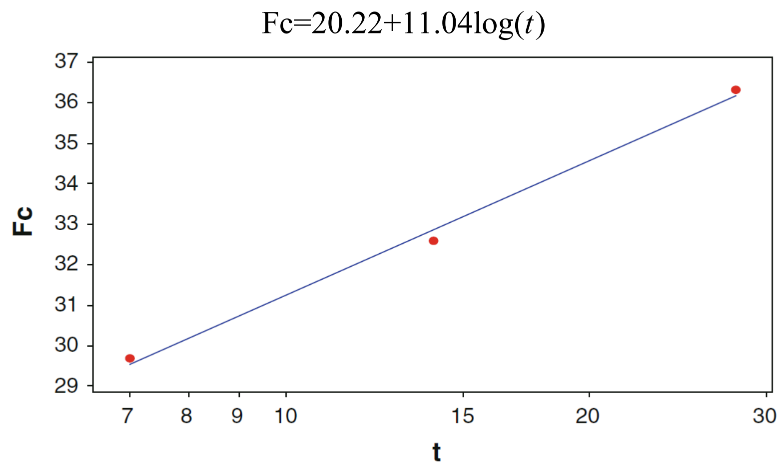

Fig. 1 Relationship between compressive strength with time of curing in water (days)

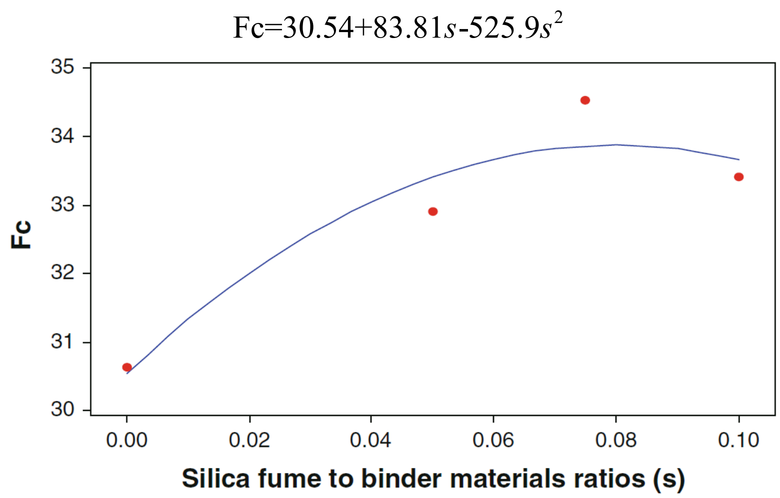

Fig. 2 Relationship between compressive strength and SF to binder materials ratios

The relationship between compressive strength with considered variables may be represented by:

$$f_c = \frac{A}{B^{(\frac{w}{b})}} \times (11.04 \times \log(t) + 20.22)^C \times (-525.9s^2 + 83.81 + 30.54)^D \tag{3}$$

where f_c is the compressive strength (MPa), $(\frac{w}{b})$ is the ratio of water to binder materials, t is time of curing in water (day), s is the ratio of SF to binder materials. A, B, C and D are constant coefficients, which can be determined with multiple linear regressions. The values of these coefficients are shown in Table 1.

Table 1 Numeric effects of diagram for compressive strength

A	*B*	*C*	*D*
2.637	0.999	0.98	0.977

With replacement of coefficients and some simplification, the following equation is obtained.

$$f_c = \frac{49.2}{10^{(\frac{w}{b})}} \times (0.546 \times \log(t) + 1) \times (-17.22 s^2 + 2.74 s + 1) \quad (4)$$

Conclusions

Results can be summarized as follows:

(1) SF decreases the fluidity of concrete.

(2) Cement replacement up to 7.5 % with SF leads to increase in compressive strength.

(3) SF optimizes the compressive strength.

(4) Abram's law with some modification is applicable to the compressive strength of concretes contain of SF. Also, according to main effects of diagram the following equation could be proposed:

$$f_c = \frac{49.2}{10^{(\frac{w}{b})}} \times (0.546 \times \log(t) + 1) \times (-17.22 s^2 + 2.74 s + 1)$$

The proposed model provides the opportunity to predict the compressive strength based on the time of curing in water (t), water and SF to binder materials ratios which are shown as ($\frac{w}{b}$) and (s) briefly.

References

[1] Bhikshma, V., Nitturkar, K., & Venkatesham, Y. (2009). Investigations on mechanical properties of high strength silica fume concrete. Asian Journal of Civil Engineering Building and Housing, 10(3), 335–346.

[2] Beeldens, A., Van Gemert, D., Schorn, H., Ohama, Y., & Czarnecki, L. (2005). From microstructure to macrostructure: An integrated model of structure formation in polymer-modified concrete. Materials and Structures, 38, 601–607.

[3] Chen, B., & Liu, J. (2007). Mechanical properties of polymermodified concretes containing expanded polystyrene beads. Construction and Building Materials, 21, 7–11.

[4] Jun, L., Chang-Wei, X., Xiao-Van, Z., & Ling, W. (2003). Modification of high performances of polymer cement concrete. Journal of Wuhan University of Technology-Mater, 18(1), 61–64.

[5] Biswal, K. C., & Sadang, S. C. (2010). Effect of superplasticizer and silica fume on properties of concrete. In Proceedings of International Conference on Advances in Civil Engineering.

[6] Popovics, S. (1998). Strength and related properties of concrete a quantitative approach. New York, NY: Wiley.

Applied Mechanics and Materials Vols. 744-746 (2015) pp 82-87

doi:10.4028/www.scientific.net/AMM.744-746.82

Evaluation on dynamic responses of transmission lines subjected to wind excitations

Pengyun Li[1,a], Bo Chen[2,b,*] Wen-ping Xie[1,c], Hao Liu[2,d]

[1]Electric Power Research Institute, Guangdong Power Grid Corporation Co. Ltd., Guangzhou, China

[2]Key Laboratory of Roadway Bridge and Structural Engineering, Wuhan University of Technology, Wuhan, China

[a]newpy@126.com,[b]cbsteven@163.com, [c]nwxiewp@163.com, [c]celiuh@163.com

Keywords: Transmission line, performance evaluation, dynamic responses, wind excitation.

Abstract: The evaluation on dynamic responses of transmission lines subjected to wind excitations is actively carried out in this study. A transmission tower-line system constructed in the southern coastal areas of China is taken as example to examine the wind induced response of the transmission lines. The structural model is established based on finite element approach by using commercial package. The displacement, velocity and acceleration responses of the transmission lines are computed to explore structural performance. The made observations indicate that the transmission lines vibrant substantially when subjected to strong winds. It is obvious that the dynamic responses of the ground wire are smaller than those of the wire and the responses in the long span are much larger than those in the short span.

Introduction

Strong wind is a typical dynamic excitation acting on the electrical infrastructures. In recent years, many damage and failure events of the transmission tower-line system have been reported and attracted more and more attention from researchers and engineers throughout the world. The transmission line is a cable structures with very small stiffness and damping, which may vibrant substantially under the wind loadings [1-3]. Actually, there exists a strong interaction between the motion of the tower and that of the transmission lines subjected to wind loading [4-6]. Therefore, the dynamic responses of the transmission lines should be investigated by considering the effects of the transmission tower [7-8].

The evaluation on dynamic responses of transmission lines subjected to wind excitations is actively carried out in this study. A transmission tower-line system constructed in the southern coastal areas of China is taken as example to examine the wind induced response of the transmission lines. The structural model is established based on finite element approach by using commercial package. The displacement, velocity and acceleration responses of the transmission lines are computed to explore structural performance.

Analytical model

The transmission tower is a typical spatial structure constructed by using steel members, which can be modelled by using beam and truss elements based on the finite element method. The element stiffness matrix $\mathbf{K}_{l,e}$ in the local coordinate system can be expressed as

$$\mathbf{K}_{l,e} = \begin{bmatrix} \mathbf{k}_c & -\mathbf{k}_c \\ -\mathbf{k}_c & \mathbf{k}_c \end{bmatrix} \tag{1}$$

In which: the submatrix $\mathbf{k}_c$ consists of the linear stiffness matrix $\mathbf{k}_l$ and the nonlinear stiffness matrix $\mathbf{k}_{nl}$

$$\mathbf{k}_c = \mathbf{k}_l + \mathbf{k}_{nl} \tag{2}$$

$$\mathbf{k}_l = \frac{EA}{L^3}\begin{bmatrix} x^2_{ji} & x_{ji}y_{ji} & x_{ji}z_{ji} \\ & y^2_{ji} & y_{ji}z_{ji} \\ & & z^2_{ji} \end{bmatrix} \tag{3}$$

$$\mathbf{k}_{nl} = \frac{N}{L}\begin{bmatrix} 1 & 0 & 0 \\ & 1 & 0 \\ & & 1 \end{bmatrix} \tag{4}$$

Where N is the tensile of the transmission line; L is the length of a cable element. The element length in the three orthogonal direction x ,y ,z are given by

$$x_{ji} = x_j - x_i \tag{5}$$

$$y_{ji} = y_j - y_i \tag{6}$$

$$z_{ji} = z_j - z_i \tag{7}$$

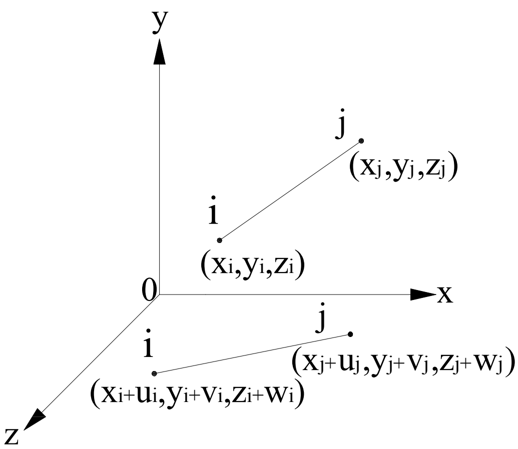

Figure 1 Model of the transmission line

The mass matrix of the transmission lines can be expressed by using the lumped mass assumption. To examine the dynamic responses of the transmission tower-line system, the finite element model of the transmission angle tower is established with the aiding of commercial package ANSYS as shown in Figure 1.

$$\mathbf{K} = \mathbf{K}_T + \sum_{i=1}^{nl} \mathbf{K}_l^i \tag{8}$$

$$\mathbf{M} = \mathbf{M}_T + \sum_{i=1}^{nl} \mathbf{M}_l^i \tag{9}$$

Where $\mathbf{K}$ and $\mathbf{M}$ are the stiffness matrix and mass matrix of the transmission tower-line system; $\mathbf{K}_T$ and $\mathbf{M}_T$ are the stiffness matrix and mass matrix of the transmission tower; $\mathbf{K}_l$ and $\mathbf{M}_l$ are the stiffness matrix and mass matrix of the transmission line in the global coordinate system.

The mass and stiffness matrices for all the lines can be constructed by summarizing the element matrices of each individual line. In addition, the mass and stiffness matrices of the transmission tower-line system can be established by combining the contribution of both towers and lines.

Structural description

Displayed in Figure 2 is the model of a transmission tower-line system constructed in the coastal areas in the southern China. This tower is a typical transmission tower with the span of the two adjacent spans being 793 m and 568m, respectively. The height of the tower is 69m. The tower is designed and constructed by using Q235 steel. To investigate the dynamic responses of the transmission tower-line system, the finite element model of the transmission tower is established with the aiding of commercial package ANSYS. There are five transmission lines for both the long span and the short span, respectively. As far as each span is concerned, there are three ground wires and two wires as shown in Figure 2. The in-plane and out-of-plane directions are denoted as X and Y directions, respectively.

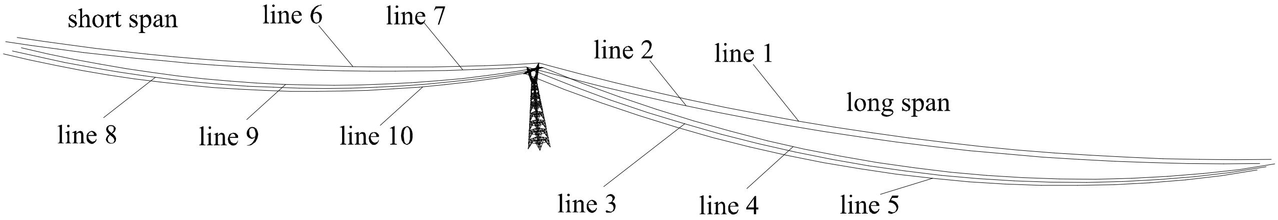

Figure 2 Model of the transmission tower-line system

Wind induced dynamic responses

The equation of motion of the example transmission tower-line system subjected to wind loading can be expressed as

$$\mathbf{M}\ddot{\mathbf{x}}(t)+\mathbf{C}\dot{\mathbf{x}}(t)+\mathbf{K}\mathbf{x}(t)=\mathbf{W}(t) \tag{10}$$

Where **M**, **C** and **K** are the mass, damping and stiffness matrices of the tower-line system, respectively; $\ddot{\mathbf{x}}(t)$, $\dot{\mathbf{x}}(t)$ and $\mathbf{x}(t)$ are the displacement, velocity and acceleration responses of the transmission tower-line system, respectively; **W**(t) is the dynamic wind loading.

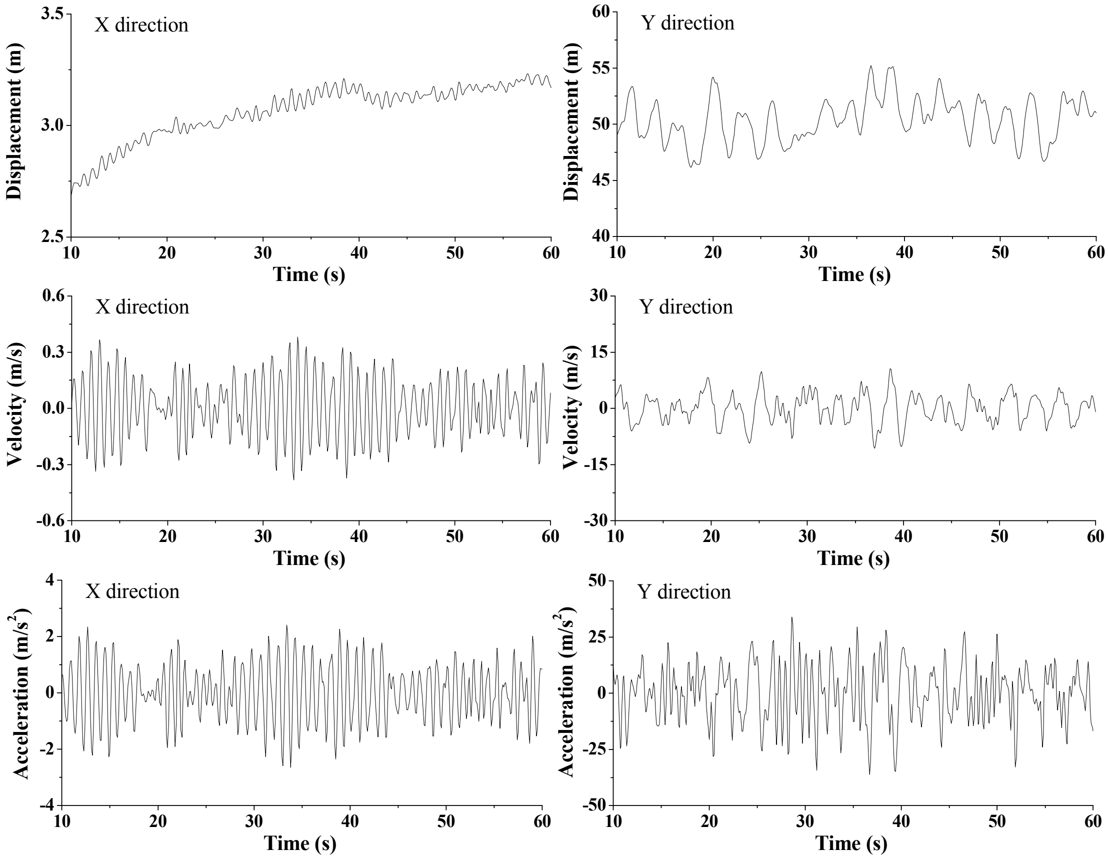

(a) X direction (b) Y direction

Figure 3 Time histories of dynamic responses of line 1 in the long span

The dynamic responses of the transmission line subjected to strong winds with a speed of 45 m/s are investigated. The dynamic responses of the wires (line No. 1) are compared to those of the ground wires (line No. 3). Figure 3 indicates the time histories of displacement, velocity and acceleration responses of the line 1, respectively. The counterparts of the ground wires are displayed in Figure 4.

It is seen from Figure 3 that the wind-induced dynamic responses for the out-of-plane vibration is much larger than those of the in-plane vibration. The maximum displacement in the x and y direction are about 3.3m and 55m, respectively. This is because the in-plane stiffness of the transmission line is larger than the out-of-plane stiffness. In addition, similar observations can be made from the velocity and acceleration responses. Figure 4 displays the time histories of dynamic responses of line 3 in the long span. The maximum displacement in the x and y direction are about 0.9m and 46m. It is obvious that the dynamic responses of the ground wire (line3) are smaller than those of the wire (line 1). The time histories of dynamic responses of line 6 in the short span are computed and displayed in Figure 5. The maximum displacement in the x and y direction are about 0.04m and 28m, respectively. To compare the dynamic responses of the transmission lines, one can found that the responses in the long span are much larger than those in the short span. It is seen that the transmission lines may vibrant substantially if they are excited by strong winds.

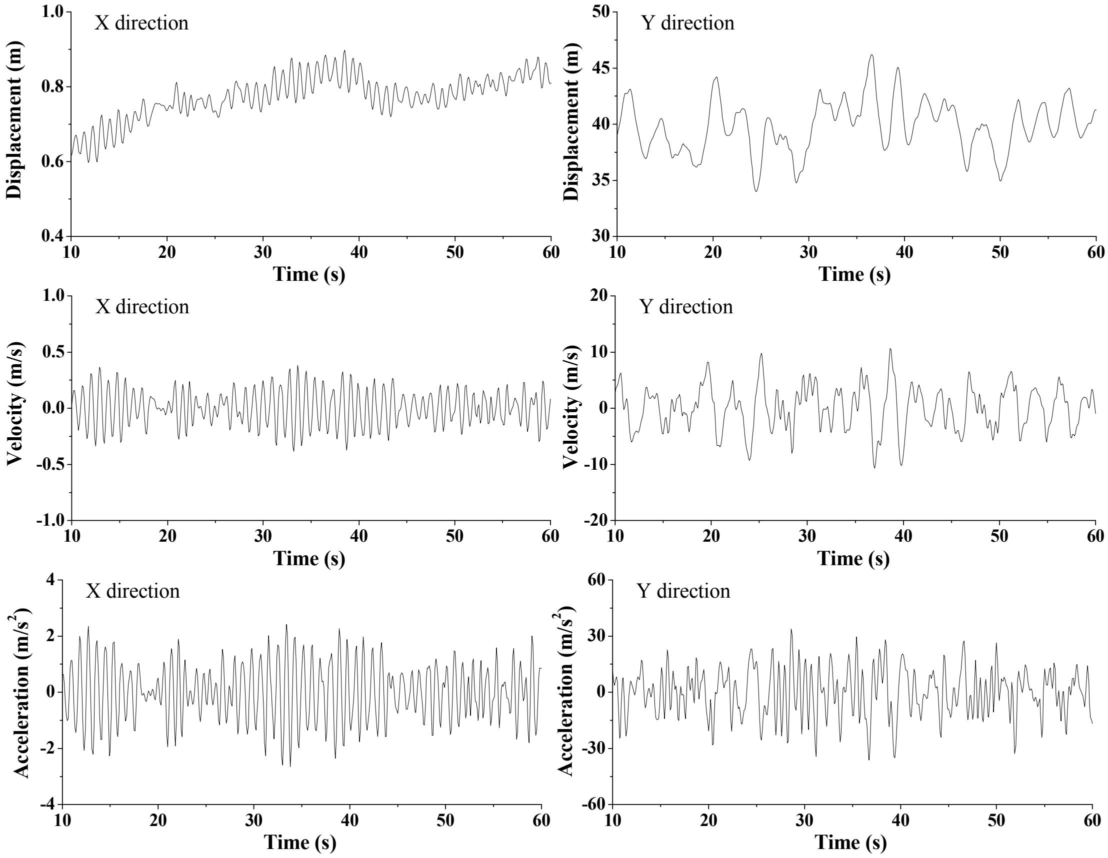

(a) X direction (b) Y direction

Figure 4 Time histories of dynamic responses of line 3 in the long span

Conclusions

The performance of a transmission tower-line system subjected to wind excitations is computed and the dynamic responses of transmission lines are actively investigated in detail in this study. The structural model is established based on finite element approach by using commercial package. The equation of motion of the transmission tower-line system under wind excitations is established. The displacement, velocity and acceleration responses of the transmission lines are computed to explore structural performance. The made observations indicate that the transmission lines vibrant substantially when subjected to strong winds. It is obvious that the dynamic responses of the ground wire (line3) are smaller than those of the wire (line 1) and the responses in the long span are much larger than those in the short span.

Acknowledgements

The writers are grateful for the financial support from the technological project of the Chinese Southern Power Grid Co. Ltd (Grant K-GD2013-0783), the Fok Ying-Tong Education Foundation (Grant 131072) and the natural science foundation of Hubei province (2014CFA026). Correspondence should be addressed to Bo Chen; cbsteven@163.com.

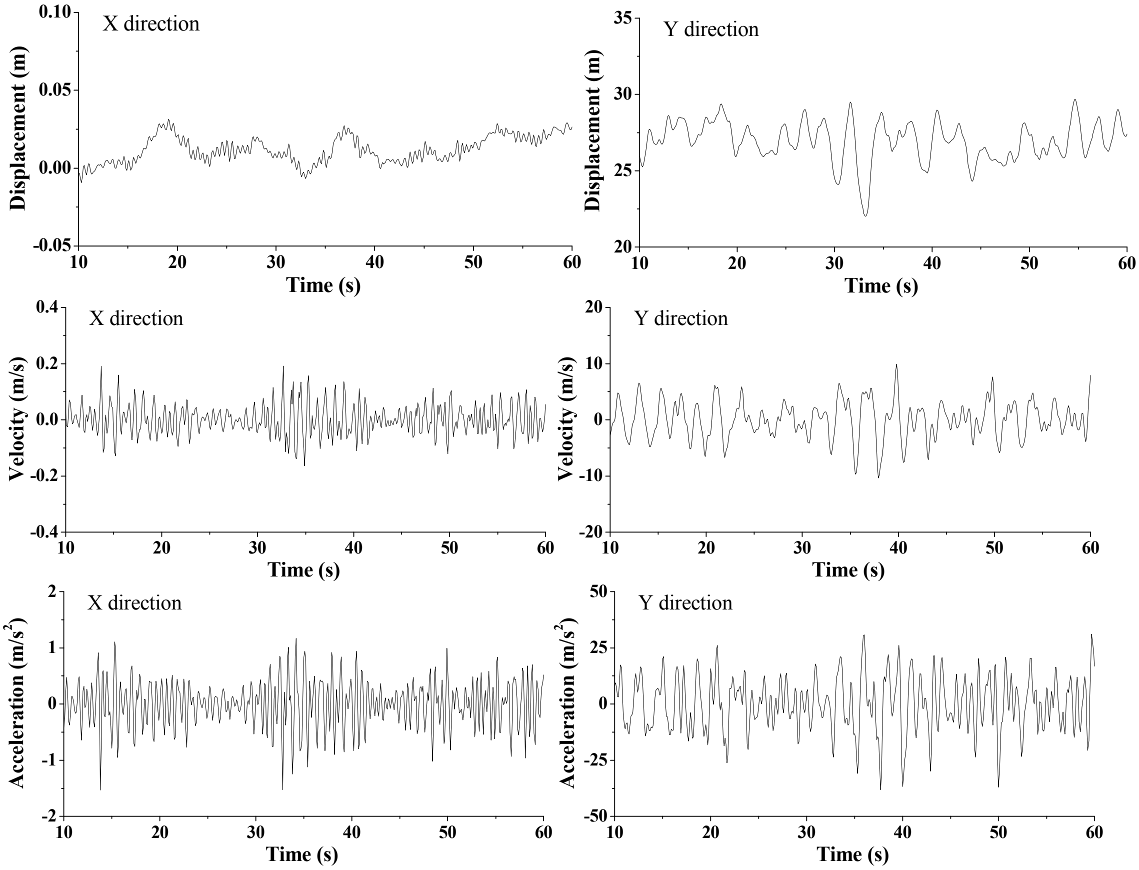

(a) X direction (b) Y direction

Figure 5 Time histories of dynamic responses of line 6 in the short span

References

[1] Chen,B., Zheng,J. Qu,W.L.(2009). Control of wind-induced response of transmission tower-line system by using magnetorheological dampers. International Journal of Structural Stability and Dynamics. 9(4):661-685.

[2] Chen, B., Guo W.H., Li P.Y., Xie W.P. (2014). Dynamic responses and vibration control of the transmission tower-line system: a state-of-the-art-review, The Scientific World Journal, Vol.2014, Article ID 538457, 1-22.

[3] Kempner, L.J., Smith, S., and Stroud, R.C. Structural dynamic characterization of an experimental 1200 kilovolt electrical transmission-line system. Shock and Vibration Bulletin, 1988, 50:3, 113-123.

[4] Chen, B, Y. L. Xu, Integrated vibration control and health monitoring of building structures using semi-active friction dampers: Part II-numerical investigation, Engineering Structures. 30(3) (2008), 573-587.

[5] Chen,B., Zheng,J. and Qu,W.L. (2007). Wind-induced vibration control of transmission tower using magnetorheological dampers, International Conference on Health Monitoring of Structure, Material and Environment, Nanjing, China, 323-327.

[6] Kempner L.J. and Smith S. Cross-rope transmission tower-line dynamic analysis, Journal of Structural Engineering ASCE. 110(6) (1984), 1321-1335.

[7] Chen, B., Sun, Y.Z., Li, Y.L., Zhao,S.L. (2014). Control of seismic response of a building frame by using hybrid system with magnetorheological dampers and isolators, Advances in Structural Engineering, 17(8): 1199-1215.

[8] Chen, B., Guo W.H., Li P.Y., Xie W.P. (2014). Dynamic responses and vibration control of the transmission tower-line system: a state-of-the-art-review, The Scientific World Journal, Vol.2014, Article ID 538457, 1-20.

Applied Mechanics and Materials Vols. 744-746 (2015) pp 88-92
© (2015) Trans Tech Publications, Switzerland
doi:10.4028/www.scientific.net/AMM.744-746.88

Experiment Research on Seismic Performance of Framework Joint Connected with Strengthening Planting Bar

Li Juan Song [1, a], Yu Guo Liang [2,b] , Li Feng Shi [3,c]

[1] Hebei Building Research Technical Co., Ltd., Shijiazhuang Hebei 050021, China

[2] Hebei Academy of building Research, Shijiazhuang Hebei 050021, China

[3] Hebei Post, Shijiazhuang Hebei 050000, China

[a]songlijuanandy@126.com, [b]liangyuguo5088@126.com, [c]691707231@qq.com

Keywords: Inorganic embedded-bar, frame joints, cyclic loading, seismic

Abstract. This issue conducted the low cyclic reversed loading test of 3 groups of framework joints formed by inorganic anchorage materials and 1 group of the one formed by integral concreting. This paper study the seismic performance, analyzed the hysteretic curve, bearing capacity, ductility and the capacity of energy dissipation of the framework joints. The conclusion can be obtained that the bearing capacity of framework joints connected with strengthening planting bar are better than the ordinary joints. The ductility and seismic performance are good.

Introduction

Anchorage is based on structural adhesive for ribbed steel bars or threaded screw anchorage to the substrate in concrete. Compared with other anchorage technique, the merits of planting bar technology are apparent. Such as it can be designed flexible, precision positioning and it is widely used. The construction is simple and could shorten the construction period. The injury of planting bar technology in the structure is little, and the capacity of the planting bar is good. The inorganic anchoring material has the advantage of good aging resistance and thermal stability[1]. So in recent years inorganic embedded-bar technique has been widely used in reinforcement and reconstruction engineering. Many add-layer projects are connected by inorganic embedded-bar, and then the new frame joints are forming. But the mechanical property and Seismic performance of the frame joints are unknown, and the related research are few. The present studies are mainly in the aspects of planting bar pullout test[2], which is different from the actual stress. So it is necessary to study the system in-depth level.

We test the frame joint formed by inorganic anchorage materials under the low cyclic reversed loading, and analyze the hysteretic curve, bearing capacity, ductility and the capacity of energy dissipation of the framework joints.

Specimen design

We design and made 3 groups of framework joints formed by planting bar with inorganic anchorage materials (named A, B and C) and 1 group of the one formed by integral concreting (named D). In each group, there are two models (No.1 and 2), and the processing methods of planted bar joints of beam column interface are different.

The specimens are all full-scale models. The section size of the column is 400mmX400mm, and the section size of the beam is 250mmX400mm. The concrete strength grade of column is C20, and the beam is C25. The longitudinal reinforcement in the column is 816, and the stirrup is 8@150. The longitudinal reinforcement in the beam is 416, and the stirrup is 8@80/200. The cross-section and reinforcement of the specimens are shown in Figure 1.

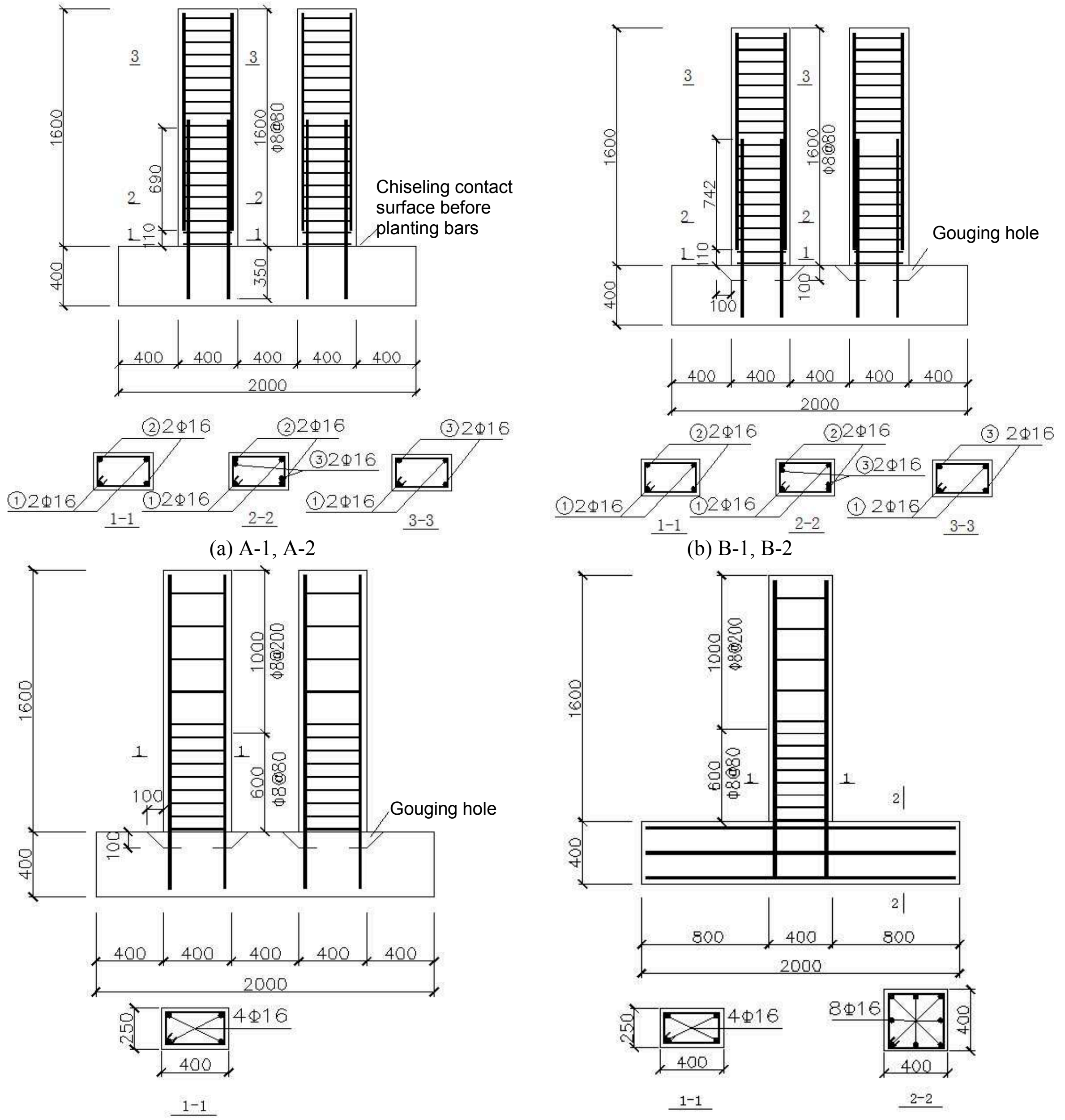

(a) A-1, A-2 (b) B-1, B-2

(c) C-1, C-2 (d) D-1, D-2

Fig. 1 Detailed design of the specimens

Loading test on specimens

The experiment is put on trial on a hydraulic servomechanism tester in the structure laboratory and hydraulic loading installation was used in the text. The low reversed cyclic loading tests are carried out on the specimens. The load and displacement method was used in this text. The load control is used in the first stage, until the load reach the theoretical calculation loading or displacement reaches values of theoretical calculation displacement. In the second stage, the displacement control is used until large strain occurs on the specimens. The loading system is shown in fig. 2. Test test equipment is shown in fig. 3.

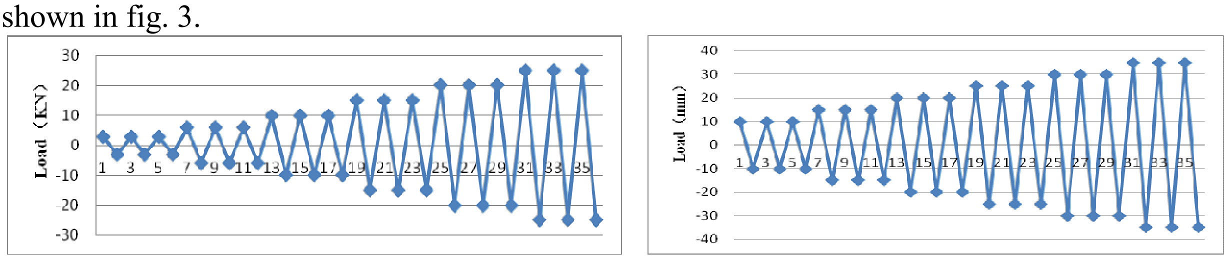

(a) The load control (b) The displacement control

Fig. 2 The loading system on the specimens

Fig. 3 Test test equipment

Analysis of test results

4.1 Analysis of hysteresic curves of the specimens

The hysteresic curves (P-△) of all the specimens are shown in fig. 4.

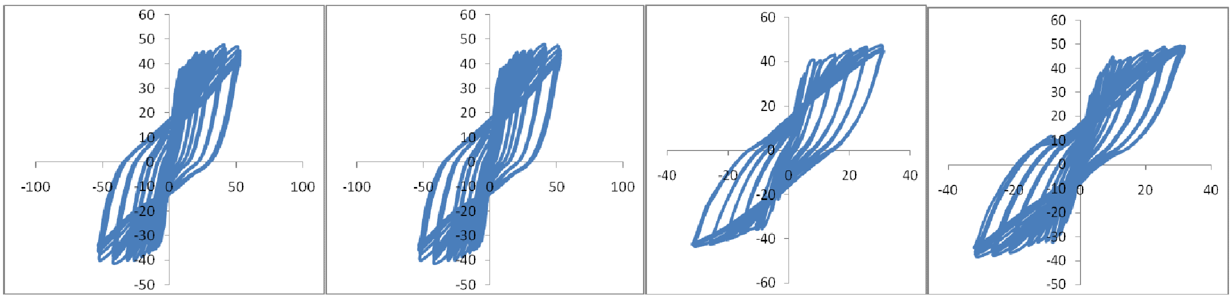

(a) A-1 (b)A-2 (c)B-1 (d)B-2

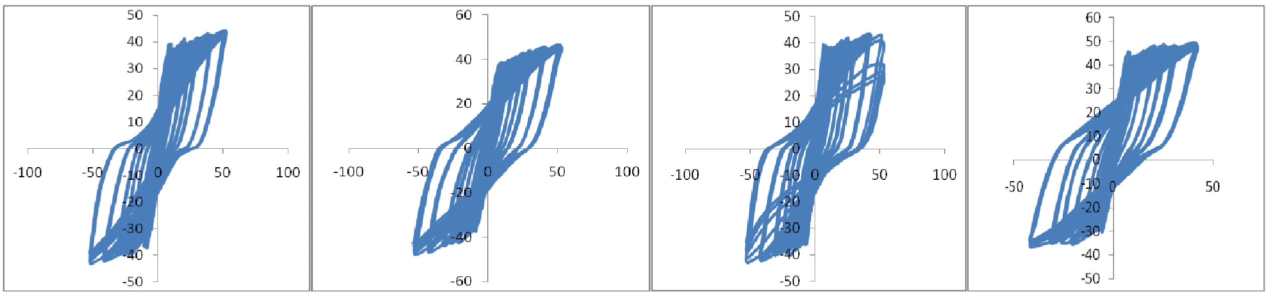

(e) C-1 (f)C-2 (g)D-1 (h)D-2

Fig. 4 The hysteresic curves (P-△) of the specimens

Comparing the hysteresic curves of the specimens, we know that the hysteresic curves of the group C are similitude to the group D's. Because there is no overlap on the steel bar embedded and with slot treatment at the junction of the beam and column, the performance of the group C is most close to the group D. The second is group B in which there are whole steel bar embedded diagonal the other steel bar lapped diagonal and the junction is same to group D. The worst is group A, which has the same steel bar with group B, but only chiseled at the junction of the beam and column. At the joint the large slip happen when the specimens failure, so the performance is slightly inferior to the other two schemes.

4.2 The bearing capacity of the specimens

The cracking load, yield load and the ultimate load of all the specimens are shown in table 1.

Table 1 The bearing capacity of the specimens

The specimen number	The cracking load P_{cr}[kN]	The yield load P_{f}[kN]	The ultimate load P_{u}[kN]
A-1	18.84	35.46	43.61
A-2	19.18	35.89	44.24
B-1	20.18	37.85	45.06
B-2	20.28	36.85	43.12
C-1	20.17	38.26	43.41
C-2	21.67	35.52	46.66
D-1	20.03	37.17	41.73
D-2	19.72	36.54	42.44

Table 1 shows that there is little difference between framework joints formed by planting bar with inorganic anchorage materials and the one formed by integral concreting in the cracking load and yield load. The ultimate load of the planting bar joints is high than the joints formed by integral concreting.

4.3 The ductility of the specimens

Ductility of the joints is an important index to measure the ability of inelastic deformation of the frame joints. It is defined as the property of deformation when the bearing capacity does not reduced significantly after structures or components access to failure stage[3]. That the bearing capacity does not reduced significantly means the whole processes since the steel yield to the bearing capacity decrease to 85% of the largest bearing capacity. If the ductility of component meets a certain requirement, the deformation of the structure will be very large when under the ultimate load or vicinity.Then the structure has a good seismic performance.

Reinforced concrete structure is not elastic structure in the strict sense, so when the earthquake reaches to a certain extent ,the structure will enter into plastic stage, and it will rely on it’s plastic deformation in absorbing and dissipating seismic energy.With better ductility comes with larger ductility factor and more seismic energy will be absorbed and dissipated.Then the damage of seismic effect will be lower. The ductility of single particle component can be measured by μ_Δ (ductility factor)which could be calculated as follows.

$$\mu_\Delta = \frac{\Delta_\mu}{\Delta_y} \qquad (1)$$

where, Δ_y is the displacement of beam end when member yields; Δ_μ is the ultimate displacement when member yields.

According to the formula ductility factors of all the members can be calculated and showed in table 2.

Table 2 The ductility factors of the specimens

The specimen number	Δ_y [mm]	Δ_μ [mm]	μ_Δ
A-1	8.239	30.410	3.691
A-2	8.209	31.234	3.804
B-1	8.630	31.123	3.606
B-2	9.330	31.179	3.342
C-1	8.335	30.812	3.697
C-2	8.301	31.711	3.820
D-1	7.437	31.200	4.195
D-2	7.273	31.065	4.271

Table 2 shows that the ductility of the frame joints formed by integral concreting is better than the framework joints formed by planting bar with inorganic anchorage materials. That is because of the specimen yield earlier. The ductility coefficient of every scheme from large to small is as follows C, A, B.

3.4 Analysis on absorbing and dissipating energy

The cracking load, yield load and the ultimate load of all the specimens are shown in table 1.

The capability to absorb energy(mainly by the deformation of structure) and dissipate energy(mainly by the structure internal friction) is a point to evaluate seismic Performances of the RC frame joint. Under low cyclic loadings,structure absorbs energy while loaded on and releases energy while unloaded on. Reinforced concrete structure is not strictly elastic structure, so the energy absorbed is not equal to the energy released.The discrepancy is called the energy dissipated in a loop. Under seismic action large deformation can be resisted if the energy absorption capability of structure is good.

This paper use indicator of function ratio to evaluate the energy absorbed[3].

$$I_w = \sum_{i=1}^{n} \frac{P_i \Delta_i}{P_y \Delta_y} \tag{2}$$

where, I_w means indicator of function ratio;n means cycle number; i means cycle order; P_i , Δ_i is respectively denote the load and displacement in the i cyclic; P_y , Δ_y is respectively denote yield load and yield displacement.

The indicators of function ratio of all components can be calculated according to the formula above. Results are shown in Table 3.

Table 3 I_w of the speciments

Displacement	A1	A2	B1	B2	C1	C2	D1	D2
$1\Delta_y$	1	1	1	1	1	1	1	1
$2\Delta_y$	2.01	1.99	1.84	1.53	1.81	2.02	1.78	1.62
$3\Delta_y$	3.56	3.66	3.34	2.75	3.188	3.63	3.13	2.84
$4\Delta_y$	4.25	4.36	4.09	3.32	3.86	4.44	3.74	3.42

Table 3 shows that the average values of I_w of all the framework joints formed by planting bar with inorganic anchorage materials are slightly higher than that of the integral casting frame node.

Conclusions

From the test results, the following conclusions can be drawn:

(1) The energy dissipation capacity of the framework joints formed by planting bar with inorganic anchorage materials is good, and could meet the seismic performance requirements.

(2) There is little difference between framework joints formed by planting bar with inorganic anchorage materials and the one formed by integral concreting in the cracking load and yield load. The ultimate load of the planting bar joints is high than the joints formed by integral concreting.

(3) The ductility of the planting-bar-joints is good.

(4) The average values of I_w of all the framework joints formed by planting bar with inorganic anchorage materials are slightly higher than that of the integral casting frame node. The dissipating energy capacity of the framework joints formed by planting bar with inorganic anchorage materials is better than that of the integral casting frame node.

References

[1] Dong Sui, Donglin Zhang, Jinyao Hua. The application of planting reinforcing bar construction technique in engineering, Zhejiang architecture, volume 24, issue 1(2007)

[2] Tianbao Gao, Wenli Shi. Experimental study on bond anchorage performance of planting steel bar concrete structure of inorganic materials, Shanxi architecture, volume 36, issue 5(2010)

[3] Jiuru Tang, Reinforced concrete frame joints aseismic, edtied by Southeast University press, (1989)

Applied Mechanics and Materials Vols. 744-746 (2015) pp 93-95

doi:10.4028/www.scientific.net/AMM.744-746.93

Experimental research on behavior of axially square CFRP steel tubular confined recycled aggregate concrete long columns

Jiong-Feng Liang [1,2,a] ,Ping-hua Yi [1,2,b], Jian-bao Wang [2,c]

[1] Guangxi Key Laboratory of Disaster Prevention and Structural Safety, Guangxi University, Nanning, Guangxi, 530004,China

[2] College of Architecture Engineering, East China Institue of Technology, Nanchang, Jiangxi, 330013,China

[a]jiongfeng108@126.com, [b]llyan790@126.com,[c]dengy888@126.com,

Keywords: behavior, recycled aggregate concrete, long columns

Abstract: Seven axially square CFRP steel tubular confined recycled aggregate concrete long columns were experimentally investigated to study their static behavior. The influence of the slenderness ratio, recycled coarse aggregate replacement ratio, layers of CFRP jackets effect on the performance of axial compression. The test results show that the higher the recycled coarse aggregate content and the slenderness ratio, the greater the specimen ultimate bearing capacity is smaller, and the more the layers of CFRP jackets, the greater the specimen ultimate bearing capacity.

Introduction

At present, it have made extensive research on the recycled coarse concrete [1]~[5]. But the recycled coarse concrete compared with ordinary concrete, its strength is slightly lower, elastic modulus is small, the deformation performance is increased. For this, applying lateral restraint to recycled concrete, can make its contraction deformation greatly decreases, and thus improve its shrinkage performance. At present, the common constraint concrete way were steel tube confined concrete and FRP confined concrete. According to the characteristics of recycled coarse concrete, the author puts forward using CFRP and steel tube together to improve the defect of recycled coarse concrete.

Experimental Program

7 specimens were fabricated, as shown in table 1. The main specimen parameters were slenderness ratio ($\lambda = \frac{2\sqrt{3}L}{B}$), recycled coarse aggregates replacement rate and the number of CFRP layers. The square steel tubes were 150mm in side length (B) and 1000mm, 1200mm, 1400mm in length ($\boldsymbol{L}$). The thicknesses (t) of steel tubes were 3mm. The design concrete strength (f_{cu}) was shown in table 1. The yield strength and tensile strength of steel were 498MPa, 609MPa, respectively. The numbers of CFRP layers confining the columns were zero, one, and two in the test. The design thickness and tensile strength of the carbon fiber sheets provided by the manufacturer were 0.17mm and 3471 MPa, respectively. Recycled coarse concrete replacement rates were considered for 0%, 50% and 100%, and use the same water cement ratio of 0.38, with strength grade C30 as the design strength. It was shown in table 2.

Table 1 All relevant parameters and measured test results of specimens

Specimen No.	B /mm	L /mm	t /mm	f_{cu} /Mpa	Slenderness ratio λ	Replacement rate/%
FS1	150	1200	3	26.6	27.7	0
FS2	150	1200	3	16.9	27.7	50
FS3	150	1200	3	12.9	27.7	100
FS4	150	1000	3	12.9	23.1	100
FS5	150	1400	3	12.9	32.3	100
FS6	150	1200	3	12.9	27.7	100
FS7	150	1200	3	12.9	27.7	100

Table 2 Proportioning of recycled aggregate concrete

Replacement rate (%)	Recycled coarse aggregate (kg/m^3)	Cement (kg/m^3)	Sand (kg/m^3)	Natural coarse aggregate (kg/m^3)	Water (kg/m^3)
0	0	500	479	1231	190
50	615.5	500	479	615.5	190
100	1231	500	479	0	190

Test Results and Discussion

Load—Deflection Relationship

According to the collected test load and deflection value, the load-deflection relationship for a typical column can be seen from the Figure .1. As can be seen from the Figure 1, at the beginning, the specimens were at the elastic stage, after at the inelastic phase. With the change of the recycled coarse aggregate content, the curve slope of the specimens' elastic stage is different. With the increasing of slenderness ratio, the bearing capacity of the specimen is decrease.

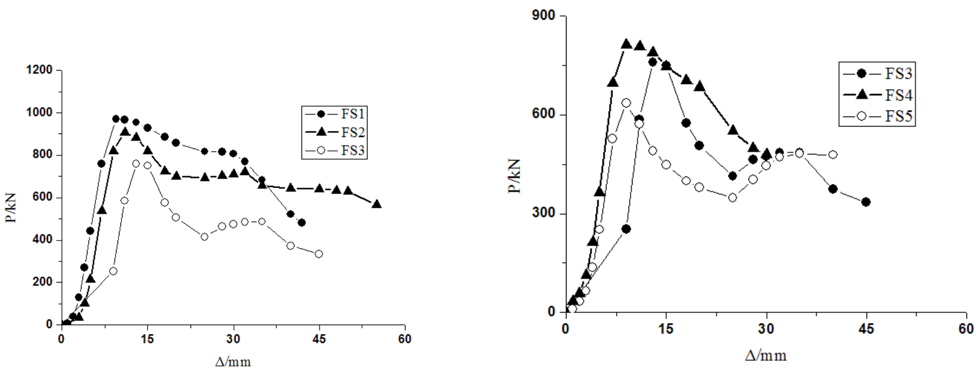

(a) (b)

Fig.1 Load-deflection relationship